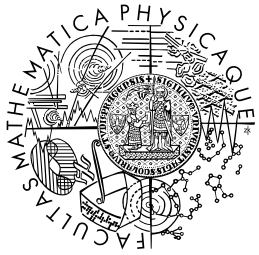

FACULTY
OF MATHEMATICS
AND PHYSICS
Charles University

MASTER THESIS

Stanislav Šašek

Microstructure and mechanical properties study of the finegrained magnesium alloys processed by severe plastic deformation

Department of Physics of Materials

Supervisor of the master thesis: RNDr. Jitka Stráská, Ph.D.

Study programme: Physics

Study branch: Physics of Condensed Matter and Materials

Prague 2021

I declare that I carried out this master thesis independently, and only with the cited sources, literature and other professional sources. It has not been used to obtain another or the same degree.

I understand that my work relates to the rights and obligations under the Act No. 121/2000 Sb., the Copyright Act, as amended, in particular the fact that the Charles University has the right to conclude a license agreement on the use of this work as a school work pursuant to Section 60 subsection 1 of the Copyright Act.

In ..... date ....

Author's signature

Acknowledgement

First of all, I would like to express my gratitude to my supervisor RNDr. Jitka Stráská, Ph.D. for patience and factual comments to this thesis. I would also like to thank PhDr. RNDr. Josef Stráský, Ph.D. for comments and advice on final editing. Thanks also belongs to RNDr. Peter Minárik, Ph.D. for instructive consultations and Mgr. Mária Zemková with Mgr. Jozef Veselý, Ph.D. for their help with secondary phases analysis. Last but not least, I would like to thank my parents for supporting me throughout my studies.

Title:

Microstructure and mechanical properties study of the finegrained magnesium alloys processed by severe plastic deformation

Author: Stanislav Šašek

Department: Department of Physics of Materials

Supervisor: RNDr. Jitka Stráská, Ph.D., Department of Physics of Materials

Abstract: Two magnesium alloys (Mg-4Y-4Gd-2Ca and Mg-2Y-2Gd-1Ca) with high ignition temperature were successfully processed by extrusion. Mg-2Y-2Gd-1Ca alloy was additionally processed by equal channel angular pressing (ECAP) to achieve ultrafine-grained microstructure. The effect of extrusion parameters on fraction of recrystallized grains, grain size, and texture was revealed by EBSD analysis. The presence of Mg_2Ca, REH_2 and Mg_5RE secondary phases was proven by SEM and TEM.

Microstructural condition including distribution and morphology of secondary phase particles directly affected the mechanical properties. Yield tensile stress exceeding 200 MPa was achieved in each condition. Large non-recrystallized grains with strong $\{10\bar{1}0\}$ texture resulted in a significant anisotropy in mechanical properties. Processing by ECAP led to a homogeneous microstructure with a mean grain size below 1 μm. ECAP condition showed superior mechanical properties with a low anisotropy.

The developed and analysed microstructural condition resulted in favourable mechanical properties. The studied alloys are therefore promising for the application in aerospace industry.

Keywords: fine-grained materials, severe plastic deformation techniques, magnesium alloys, microstructure, mechanical properties

Contents

Introduction

Magnesium, as the lightest construction material with density $\rho = 1738$ kg.m^{-3} [1], has been the subject of intensive research in recent years. Its low density and high specific strength predetermine it for application in the automotive and aerospace industries and wherever the emphasis is on weight savings. Reducing weight in cars and aircraft leads to lower fuel consumption and saving money and the environment.

The use of magnesium alloys in air transport has mainly been hampered by a ban on use because of their high flammability. In 2015, the rules prohibiting the use of magnesium alloys on passenger seat design elements were revised. Magnesium alloys may be used in aircraft seat construction if they meet the flammability performance requirements.

Ignition temperature, microstructure, and mechanical properties are influenced by alloying elements. Suitable candidates appear to be rare-earth (RE) metals. When exposed to high temperatures, they form a thermally stable oxide layer [2, 3], which has been proven to prevent the alloy from ignition. RE metals with magnesium also form intermetallic phases, which enhance mechanical properties. Secondary phases containing RE metals are thermally stable and promote particle stimulated nucleation during thermomechanical processing [4].

The processing of the material significantly affects its microstructure and thus its mechanical properties. Severe plastic deformation (SPD) methods are a group of metalworking techniques that uses very high strains to produce material with high dislocation density and small grain size. One of these methods is equal channel angular pressing (ECAP), which has proven itself in the production of ultrafine-grained (UFG) materials with a grain size below one micrometer. These materials are usually characterized by superior mechanical properties.

This thesis aims to analyse the microstructure and mechanical properties of two magnesium alloys designed with an emphasis on high ignition temperature while maintaining solid mechanical properties.

1. Aims of the thesis

The aim of the thesis is to prepare fine grained conditions of non-flammable Mg-4Y-4Gd-2Ca and Mg-2Y-2Gd-1Ca alloys, characterize their microstructure, and evaluate their mechanical properties.
Following partial aims will be achieved:

- To process two quaternary magnesium alloys by extrusion
- To process Mg-2Y-2Gd-1Ca alloy by ECAP
- To characterize the microstructure and to describe secondary phases using SEM and TEM
- To characterize mechanical properties using tensile/compression tests and microhardness measurement
- To discuss the influence of processing parameters on microstructure including texture
- To discuss the influence of microstructure on the achieved mechanical properties.

2. Theoretical background

2.1 Magnesium and its alloys

Magnesium (symbol Mg) is a chemical element with an atomic number 12. It belongs to the group of alkaline earth metals. Magnesium is the sixth most abundant element in the earth's crust and the third in seawater. Due to its great chemical affinity, magnesium is not found in its elementary form. The most common compounds are magnesite ($MgCO_3$), dolomite ($MgCO_3 \cdot CaCO_3$), and carnallite ($KCl \cdot MgCl_2 \cdot 6H_2O$) [1, 5, 6].
Magnesium is the lightest structural metal with density $\rho \doteq 1740$ kg.m^{-3} and melting point $T_m = (650 \pm 1)$ °C. It crystallizes in hexagonal close packed (HCP) structure with parameters $a = 320$ nm and $c = 520$ nm (see Fig. 2.1). The ratio $c/a = 1.624$ is very close to the ideal of HCP structure ($c/a = \sqrt{8/3} \approx 1.633$) [1,7]. There are three stable isotopes of magnesium: ^{24}Mg, ^{25}Mg, and ^{26}Mg [8].

The advantages of magnesium and its alloys are:

- Low density and high specific strength
- Good castability
- Low price and easy availability
- Good weldability under controlled atmosphere
- Recyclability.

On the other hand, there are also some disadvantages of magnesium and its alloys:

- Low elastic modulus
- Limited cold workability and toughness
- High chemical reactivity
- Low corrosion resistance
- Limited strength and creep resistance at elevated temperatures [9].

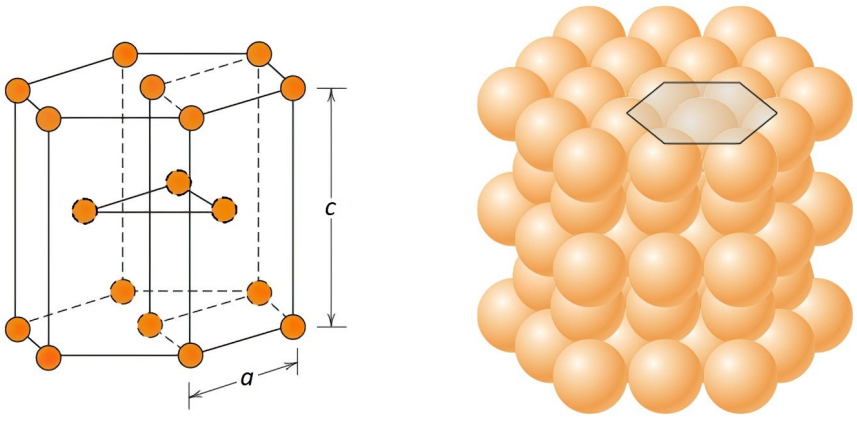

Figure 2.1: Hexagonal close-packed crystal structure [10].

2.2 Deformation mechanisms of magnesium alloys

Slip and twinning are two basic mechanisms of plastic deformation in metals.

2.2.1 Slip

Slip is the movement of one part of a crystal over the other part. On an atomic scale, it involves sliding of one plane of atoms over another. The plane on which it occurs is called the slip plane, and the direction in which they move is called the slip direction. A slip plane and a slip direction form a slip system (Fig. 2.2) [11].

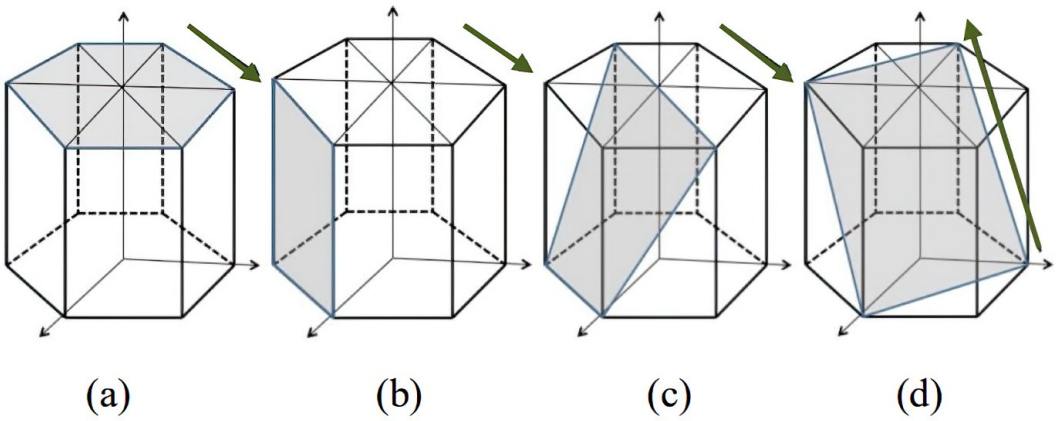

Figure 2.2: Slip systems in hexagonal structure: (a) basal, (b) prismatic, (c) pyramidal I, (d) pyramidal II. The arrow indicates the direction of the slip [12].

Slip occurs when the shear stress applied on the slip plane in the slip direction reaches a critical value called critical resolved shear stress (CRSS). Slip systems with the lowest CRSS are those with close-packed planes (with most atoms per area) and close-packed directions (most atoms per length). That is the reason why these slip systems are usually activated first. The areal density of atoms in a hexagonal lattice is related to the c/a ratio, and therefore, the preferred planes for dislocation movement differ for different HCP metals. If the c/a ratio is higher than for the ideal HCP structure, basal slip usually occurs. On the other hand, if the c/a ratio is lower, prismatic or pyramidal is more common. As noted in the previous section, magnesium has c/a close to the ideal value. Hence the basal slip can be partially substituted by prismatic or pyramidal slip systems [7].
The microscopic mechanism responsible for macroscopic plastic deformation is a mass movement of dislocations [11, 13].

2.2.2 Twinning

Magnesium, as a hexagonal metal, has only several independent slip systems (Tab. 2.1) with different CRSS. CRSS of the basal slip system is more than an order of magnitude smaller than for other slip systems. Hence, they usually require elevated temperature or higher applied stress to be activated [14]. According to the von Mises criterion, five independent slip systems are necessary

for homogenous plastic deformation of polycrystalline material [15]. For that reason deformation mechanism called mechanical twinning may take place at RT [11, 14, 16].

Direction	Plane	Notation	Number of independent modes
$\langle a \rangle$	Basal	$\{0002\}\ \langle 11\bar{2}0 \rangle$	2
$\langle a \rangle$	Prismatic	$\{1\bar{1}00\}\ \langle 11\bar{2}0 \rangle$	2
$\langle a \rangle$	Pyramidal	$\{1\bar{1}00\}\ \langle 1120 \rangle$	4
$\langle c+a \rangle$	Pyramidal	$\{10\bar{1}1\}\ \langle 11\bar{2}\bar{3} \rangle$	4
$\langle c+a \rangle$	Pyramidal	$\{2\bar{1}\bar{1}1\}\ \langle 11\bar{2}\bar{3} \rangle$	4
$\langle c+a \rangle$	Pyramidal	$\{11\bar{2}2\}\ \langle 11\bar{2}\bar{3} \rangle$	4

Table 2.1: Independent slip systems in hexagonal metals [11].

Mechanical twinning, similarly to slip, occurs by shear. A twin is a symmetrical mirror part of a crystal compared to the original undeformed crystal. The mirror plane is called the twinning plane (Fig. 2.3). Unlike slip, during twinning, a shift by non-integer multiples of the interatomic distance and an abrupt reorientation of the crystal lattice occur. Twinning shear is always directional because shear in one direction is not equivalent to shear in the opposite direction [17].

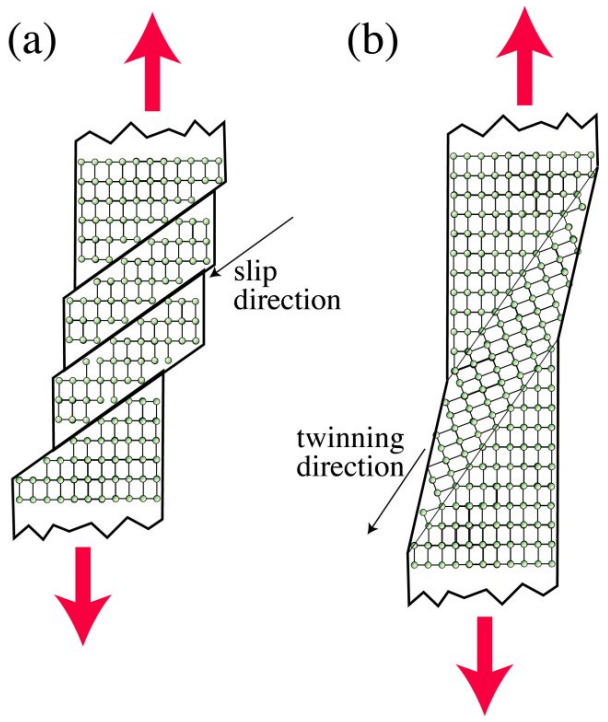

Figure 2.3: Schematic comparision of (a) slip and (b) deformation twinning [18].

The most common twinning system in HCP metals is $\{10\bar{1}2\}\ \langle 10\bar{1}1 \rangle$. This twinning system provides elongation in the c-axis, which plays an essential role in the ductile behaviour of magnesium alloys. The direction of shear associated with this twinning system depends on the c/a ratio. Magnesium and most of other

HCP metals have $c/a < \sqrt{3}$. For these metals, twins are formed when the applied tensile stress is parallel to the c-axis or for compression stress applied perpendicular to the c-axis, (Fig. 2.4). The reorientation of grain-twin is approximately 86.3° [11, 17, 19].

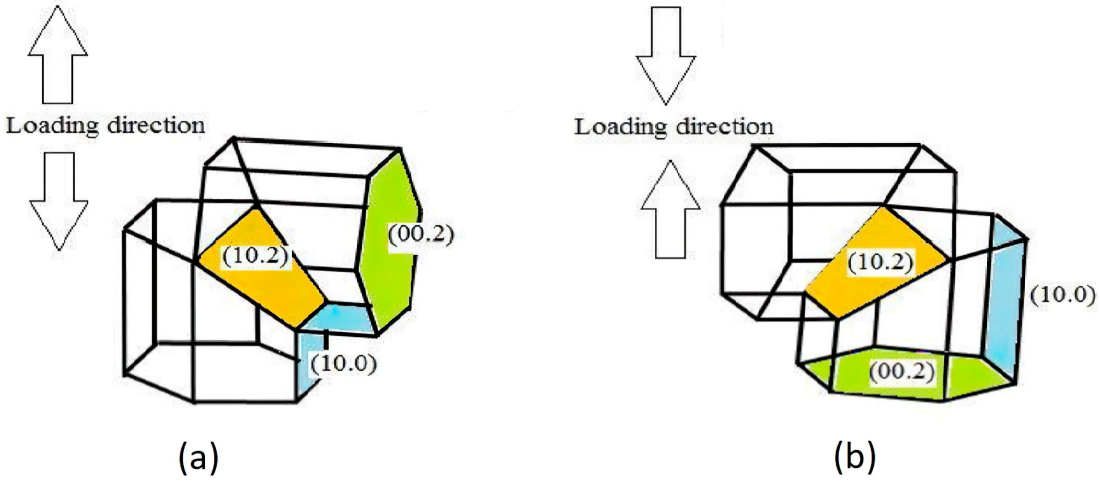

Figure 2.4: Mechanisms of twinning in magnesium alloys depending on the direction of the external stress (a) in tension (b) in compression [19].

2.3 Strengthening mechanisms in alloys

The strength of polycrystalline materials depends on the mobility of dislocations and twin boundaries. The mobility of dislocations is affected by so-called pinning points - obstacles avoiding dislocation motion. These obstacles can be other dislocations, grain boundaries, solute atoms of different elements, and precipitates. Strengthening mechanisms describe how and how much these obstacles hinder dislocation movement and affect mechanical properties.

2.3.1 Work hardening

Work hardening is caused by the interaction of mobile dislocations with dislocation structure. Dislocations create a stress field that hinders dislocation motion and strengthens the material. In addition, interactions can create entanglement and jogs, which severely influence the movement of dislocations [20]. Contribution of work hardening σ_D is given by Eq. 2.1 [21]:

$$\sigma_D = \alpha G b \rho^{-\frac{1}{2}}, \tag{2.1}$$

where α is a proportionality constant, G is the shear modulus, b is the Burgers vector, and $\rho = \frac{l}{V}$ is the dislocation density defined as dislocation lines length l per unit volume V.

2.3.2 Grain boundary strengthening

Grain boundary strengthening is a mechanism that plays a crucial role in polycrystalline materials, especially in UFG alloys. In the case of dislocation move-

ment, the Burgers vector must be a translation vector of the crystal, which usually does not hold for neighbouring grains due to their different orientations. Hence, dislocations pile up on grain boundaries generating stress that acts against subsequent dislocations. Dependence of strength on grain size is given by the Hall-Petch equation (Eq. 2.2) [22, 23].

$$\sigma_y = \sigma_0 + k_y d^{-\frac{1}{2}}, \tag{2.2}$$

where σ_y represents the yield stress, σ_0 is the resistance of the lattice to dislocation motion, k_y is the material constant, and d is the average grain diameter. Defining the diameter d is unclear in the case of bimodal grain size distribution or the case of non-equiaxed grains.
Although there exist some models explaining Eq. 2.2 described in [24–26], the complete principle is still not understood. The validity of Eq. 2.2 was experimentally verified in a wide range of grain sizes. It fails in the case of submicrometer grains, where the strength decreases with decreasing grain size. This is caused by the activation of another deformation mechanism - grain boundary sliding, see Fig. 2.5. This phenomenon is called the inverse Hall-Petch relation.

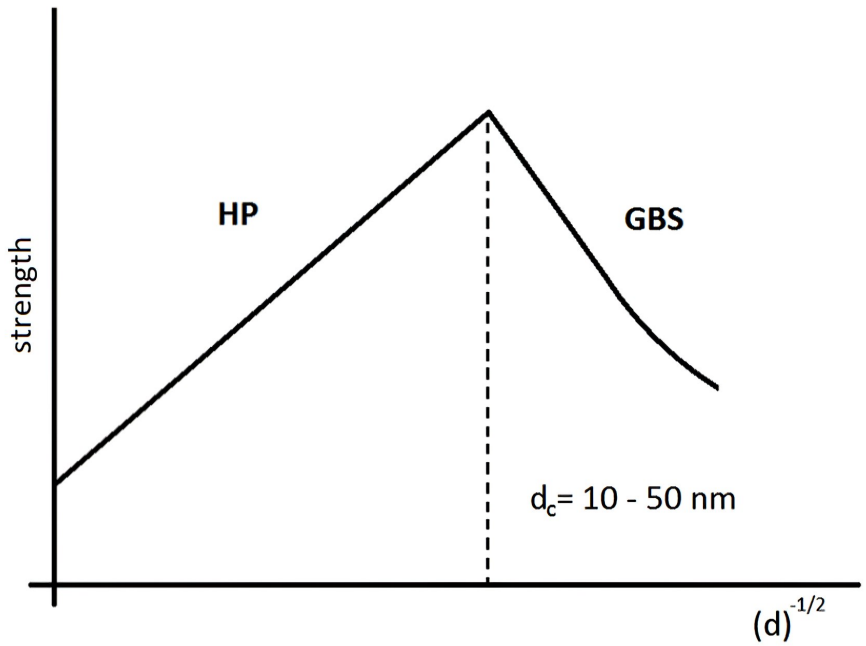

Figure 2.5: Strength of polycrystalline material depending on $d^{-\frac{1}{2}}$ - inverse Hall-Petch [27].

2.3.3 Solid solution strengthening

Atoms of other elements may occupy a substitutional or interstitial position in the matrix and form so-called solid solution, see Fig. 2.6. Solid solution forms, if Hume-Rothery rules are met, described in detail in [28]. If the rules are not met, solute atoms tend to form secondary phases. Typical interstitials are small atoms (H, C, N, O). Substitutional atoms are usually similarly large as matrix atoms.

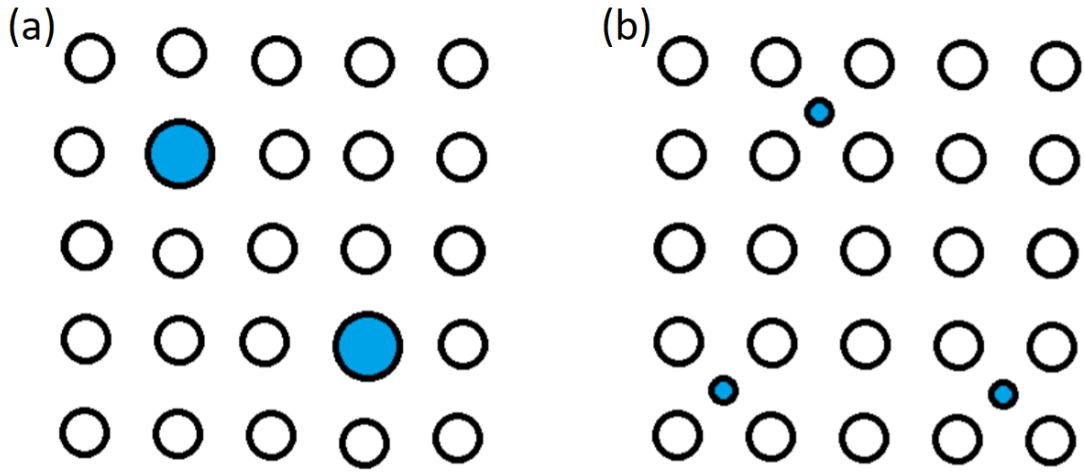

Figure 2.6: Solid solution (a) substitutional, (b) interstitial [27].

Dissolved atoms cause lattice distortion and the formation of stress field around the atoms, which acts against dislocation movement. There are a number of models describing the influence of concentration of dissolved atoms c on contribution to material strength σ_S. For example Fleischer: $\sigma_S \sim c^{\frac{1}{2}}$ [29], or Labusch $\sigma_S \sim c^{\frac{2}{3}}$ [30].

2.3.4 Precipitation hardening

Particles of secondary phases are other obstacle for dislocation motion. There are two types of precipitates - coherent and incoherent. Coherent precipitate and matrix lattice are continuous. Therefore, they must have the same type of crystalline structure. If the lattice parameters of coherent precipitate and matrix are different, a stress field is created around the precipitate. The stress increases with the increasing precipitate size until the continuity of lattice planes breaks. This is the reason why coherent precipitates are usually much smaller. There is no continuity between crystallographic planes of precipitate and matrix in the case of incoherent precipitate, see Fig. 2.7.

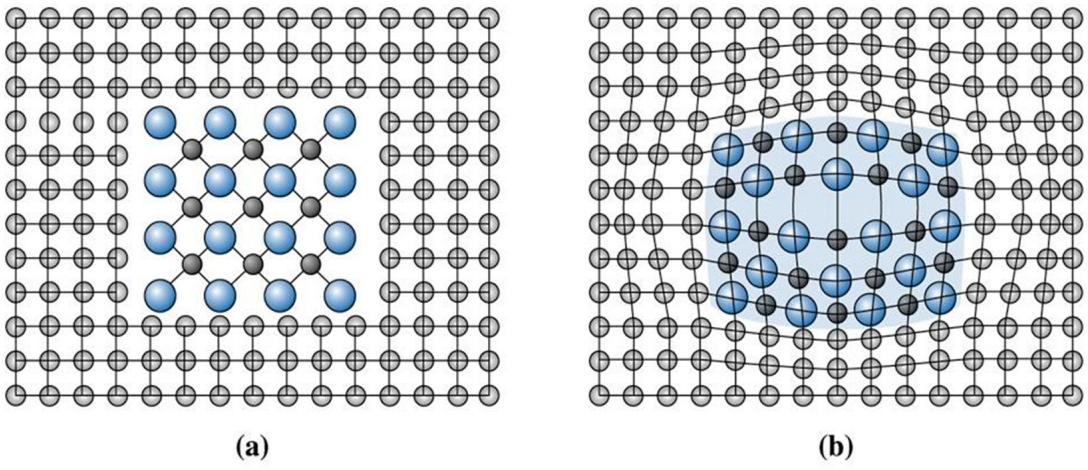

Figure 2.7: Illustration of (a) incoherent and (b) coherent precipitates [31].

Dislocations use different mechanisms to overcome coherent and incoherent precipitate. In the case of coherent precipitate, dislocation can pass through the precipitate by slip because of the crystallographic planes continuity. After passing through, an antiphase boundary can be formed and the surface energy of the precipitate increases, see Fig. 2.8. The increase in the energy of the precipitate must be associated with the work done and thus with the extra force necessary to overcome the precipitate.

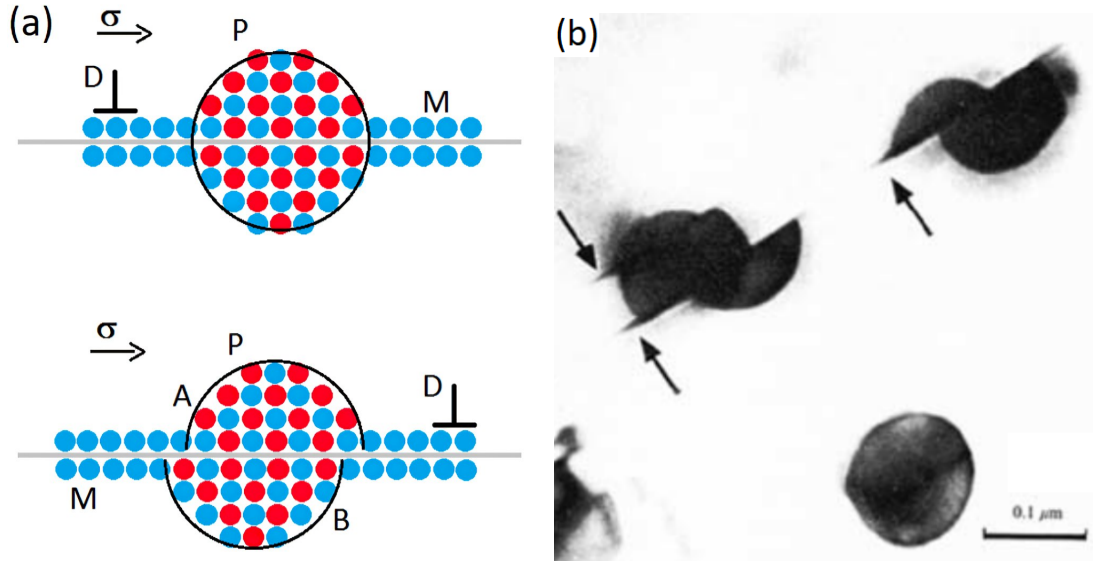

Figure 2.8: Dislocation pass through the coherent precipitate (a) schematic illustration [27], (b) Ni_3Al particles in a Ni-base alloy [32]

.

Incoherent precipitates can be overcome by dislocation by two mechanisms - Orowan looping and Hirsch looping. In the case of Orowan looping, the dislocation bends around the precipitate. If the applied stress is sufficiently high, bent sections with the opposite sign of the Burgers vector get close enough to annihilate. The dislocation splits into two parts - the dislocation loop around the precipitate and the dislocation line. The dislocation remains in one slip plane throughout the process. Multiple dislocation pass causes the formation of several concentric loops around the precipitate. That leads to what is known as Orowan strain hardening [33, 34].
An alternative mechanism involving a cross-slip, in which two dislocation loops are formed, is known as the Hirsch looping. Both mechanisms are schematically illustrated in Fig. 2.9 [34, 35].

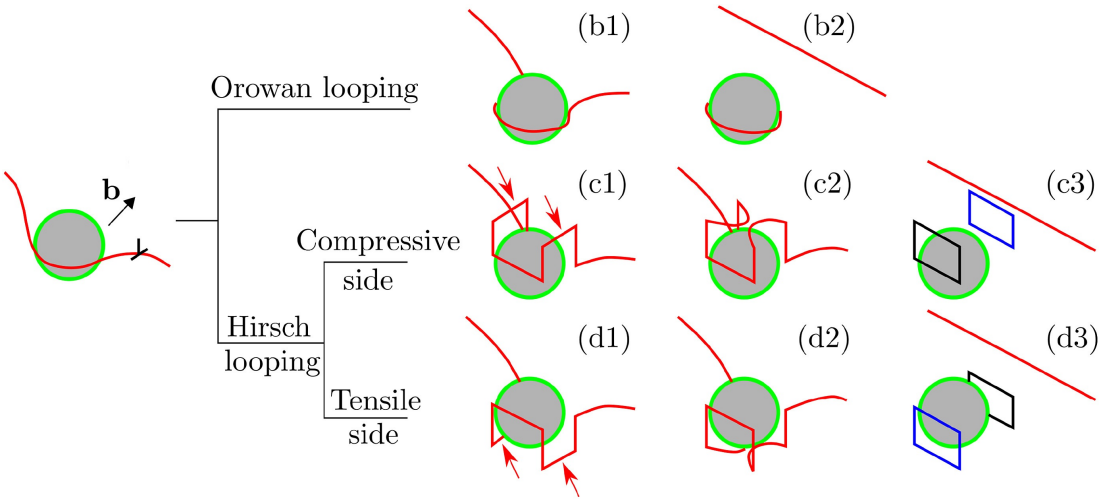

Figure 2.9: Orowan and Hirsch looping [34].

2.4 Texture and its effect on mechanical properties

Preferred orientation of crystallites (texture) is a characteristic property of polycrystalline materials. Like single crystals, polycrystals with non-random texture exhibit anisotropy of physical properties such as strength, electrical conductivity, piezoelectricity, magnetic susceptibility, light refraction, and wave propagation [36].

Two coordinate systems are necessary to quantify the texture - first related to the orientation of crystallite and the second related to sample orientation. This requires three variables, usually Euler angles, that relate these two coordinate systems. In the case of a polycrystal, it is possible to construct an orientation probability distribution of the three angles, and it is described by an orientation distribution function (ODF). ODF gives complete information about the texture [36, 37].

ODF gives the distribution of grain orientation in the material and thus the distribution of suitable volumes (grains) for activation of a particular slip or twinning system. If most of the grains are oriented so that the Schmid factor of a certain slip system is close to zero (slip plane parallel or perpendicular to tensile axis), relatively higher stress is necessary to activate this system, or activation of another system must occur. Texture is typically formed when alloys are mechanically processed, for example by rolling, extrusion or ECAP [38].

The texture can be quantitatively represented by pole figure and inverse pole figure. Pole figure is a two-dimensional projection of ODF. It shows the probability of finding a pole to a particular lattice plane in a specific sample direction. Inverse pole figure is also a two-dimensional projection of ODF, but in this case, the probability of finding a sample direction relative to crystal directions is plotted [36]. An example of pole figure and inverse pole figure is shown in Fig. 2.10.

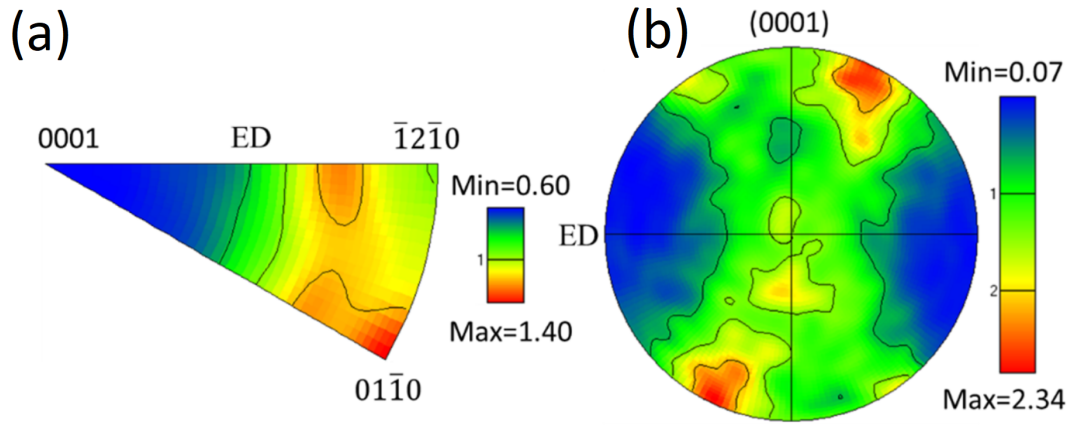

Figure 2.10: Inverse pole figure (a) and pole figure (b) of extruded WE43 alloy measured by EBSD [39].

2.5 Extrusion

Extrusion is a thermomechanical process, in which a stem presses a billet at high pressure through a tool of desired shape. The process is commonly used for the production of bars, wires, tubes, and other products with fixed cross-section. During extrusion, extruded material is under high compressive stress, and therefore also brittle materials can be extruded. Direct and indirect are the two most important types of extrusion. In the direct extrusion, a stem pushes the billet through a tool of a desired shape. In contrast, in the indirect extrusion, the die is pushed inside a hollow stew against the billet [40]. Schematic illustration of a direct extrusion facility is shown in Fig. 2.11.

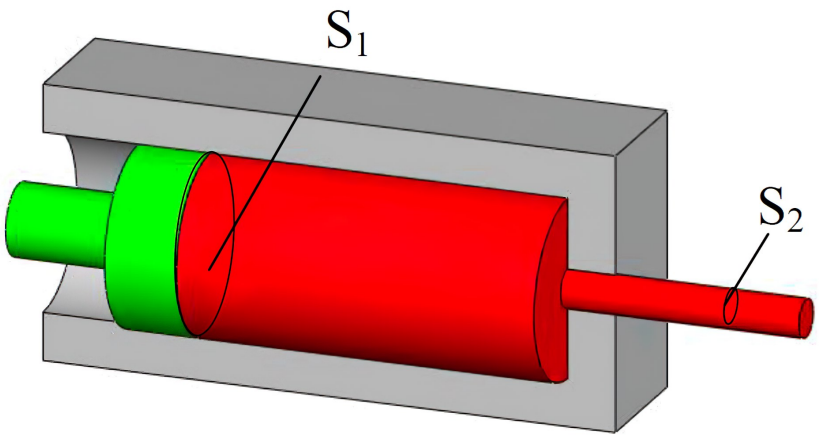

Figure 2.11: Schematic illustration of typical direct extrusion facility [38].

Three main parameters characterize the extrusion process: temperature, extrusion rate, and extrusion ratio.
The temperature plays an essential role in the extrusion process. Some materials can be extruded at room temperature (RT). However, magnesium and its alloys are usually extruded between 300 °C and 450 °C due to their low ductility at RT [38]. The process of extrusion can raise a local temperature sufficiently to

activate dynamic recrystallization. The grain size of the recrystallized grains strongly depends on the processing temperature. Lower temperature results in finer microstructure [41, 42].
The extrusion rate and extrusion temperature need to be optimized for each alloy separately. With increasing temperature, the extrusion rate can also be increased [38]. In the case of high ram speed, the temperature may increase significantly, and the dynamic recrystallization may be affected. This can result in a coarser microstructure [43].
The extrusion ratio ER is defined in Eq. (2.3):

$$\mathrm{ER} = \frac{S_1}{S_2}, \tag{2.3}$$

where S_1 is the initial cross-section and S_2 is the final cross-section of the extruded billet. The extrusion ratio has a great influence on the die exit temperature and, thereby, the grain size. A higher degree of deformation caused by a higher extrusion ratio gives rise to a higher degree of post-extrusion secondary recrystallization, and consequently, a relatively weaker texture is observed [41]. In magnesium alloys, grain size after extrusion can be in the order of micrometres, but they are usually elongated in the extrusion direction. The basal planes of non-recrystallized grains are typically orientated parallel to the extrusion axis [38].

2.6 Equal channel angular pressing

As mentioned in section 2.3, the mechanical properties of polycrystalline material are significantly affected by microstructure. Fine-grained microstructure with high dislocation density can be produced by severe plastic deformation (SPD) methods. One of these methods is Equal channel angular pressing (ECAP).
ECAP was developed by Segal and his co-workers in the 1970s and 1980s in former Soviet Union [44]. There are many various types of ECAP. Schematic illustration of a common type is shown in Fig. 2.12 [45]. The ECAP facility is relatively simple. It consists of a die with a bent channel with constant diameter and ram that pushes a billet through. A suitable lubricant such as MoS_2 is usually used to minimalize frictional effects.
The strain after N passes of ECAP with inner angle ϕ and an additional angle ψ is given by Eq. 2.4. The deformation is simple shear as it is schematically shown in Fig. 2.13 [45].

$$\varepsilon_N = \frac{N}{\sqrt{3}}\left[2\cot\left(\frac{\Phi}{2}+\frac{\Psi}{2}\right)+\Psi\csc\left(\frac{\Phi}{2}+\frac{\Psi}{2}\right)\right] \tag{2.4}$$

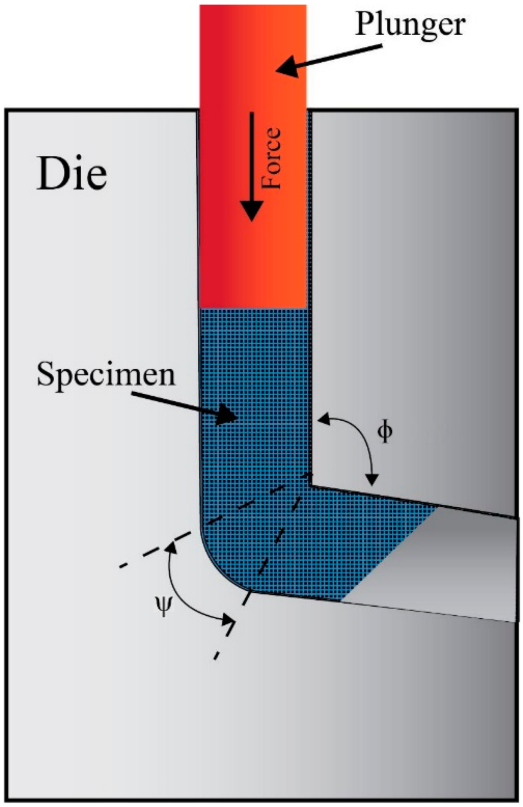

Figure 2.12: Schematic illustration of typical ECAP facility [46].

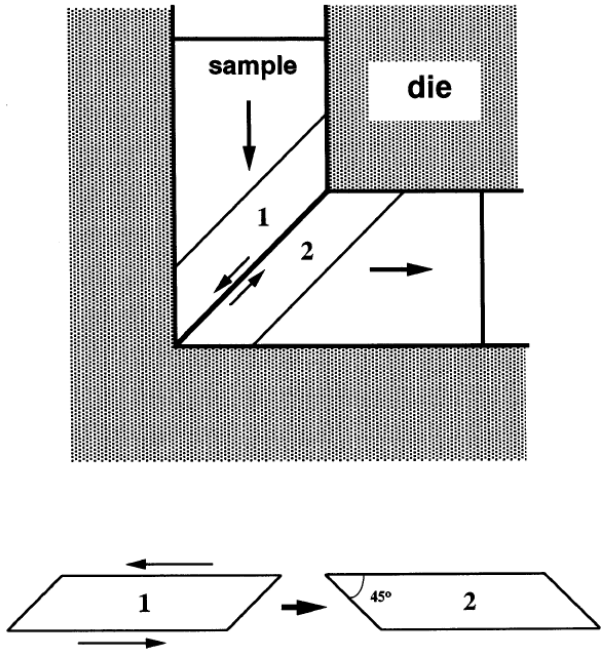

Figure 2.13: The principle of ECAP showing the shearing plane within the die [45].

The cross-section of the billet does not change, so it can be processed repetitively to attain high strains. The repetitive pressing can be used to activate different

slip systems during each pass just by rotating the billet between various passes. In practice, ECAP with square cross-section is commonly used. It allows rotating the billet by 90° or 180° after every pass. There are four fundamental processing sequences called routes. If **route A** is used, the billet is not rotated between passes. The billet is rotated by 90°, whereby the direction of rotation changes after each pass in **route $\mathbf{B_A}$**. The **route $\mathbf{B_C}$** is the same as the **route $\mathbf{B_A}$**, but the direction of rotation does not change. If the billet is rotated by 180°, it is **route C**. The same routes are easily applied in the case of the circular cross-sectional channel. Various combinations of these routes are also possible [45].
As already mentioned, using different routes leads to activation of different slip systems. That results in significant differences in the microstructure [47, 48]. On the other hand, too many passes can lead to the formation of cracks, especially if the temperature or pressing speed is not optimal.
The pressing temperature is a crucial parameter because of its great influence on grain size. It can be controlled and measured relatively easily, and a lot of studies have been done in recent years. Although pressing at higher temperatures is experimentally easier, pressing at lower temperatures results in finer microstructure with higher fraction of high-angle boundaries [49–51]. On the other hand, the temperature must be high enough to avoid cracking of the billets.

2.7 Alloys selection

Magnesium is a chemically active metal and easily reacts with other metal elements creating intermetallic phases. These secondary phases significantly affect microstructure and mechanical properties. The most widely used alloying element in magnesium alloy is aluminium. Addition of aluminium results in enhanced mechanical properties. It also improves castability [1].
The addition of calcium can assist in grain refinement and creep resistance. It also improves corrosion resistance and thermal and mechanical properties [1]. Calcium is known to increase the ignition temperature of magnesium alloys especially in synergy with yttrium [52]. The disadvantage of magnesium alloys containing Ca is their limited ductility due to high concentration of Ca-rich intermetallic phases, forming at the grain boundaries and causing intergranular cracking.
Rare earth metals are added to improve mechanical properties at elevated temperatures. It also increases creep resistance and corrosion resistance. When exposed to high temperatures, a rare earth's oxide layer forms on the surface, protecting from the ignition.
The increase of ignition temperature was confirmed in alloys containing Y and Gd, when an oxide layer composed of Gd_2O_3 and Y_2O_3 was formed on the surface [2, 3, 53, 54]. Because of their high price, they are primarily used in high-tech alloys [1, 55].
In the present work, two magnesium alloys containing Y, Gd, and Ca featuring the combination of high ignition temperature, high strength, and satisfactory elongation were prepared. Alloying elements were selected preferentially according to their positive effects on the ignition temperature. Newly designed alloy Mg-4Y-4Gd-2Ca was inspired by WE43 (Mg-4Y-3RE) alloy, which has successfully passed the specifically designed flammability test [56, 57]. Due to the excessive cost of Y and Gd we have also designed Mg-2Y-2Gd-1Ca alloy.

3. Experimental methods and samples preparation

3.1 Scanning electron microscopy

Scanning electron microscope (SEM) uses interactions of accelerated electrons with a sample. An image is created by rastering an electron beam over the sample surface, and certain types of electrons are emitted and collected by the appropriate detectors. There are several signals that carry information from different sample depths, see Fig. 3.1. As the depth of signal origin increases, the resolution deteriorates.

One of the signals is Auger electrons coming from a minimal depth (1nm). In most cases, scanning electron microscopes are not equipped with a detector using this type of signal.

Secondary electrons (SE) are emitted from inelastic collisions of primary electrons with electrons of the specimen's atoms. They have low energy (<50 eV). Low energy limits their mean free path in the sample, so only SE emitted very close to the surface are able to leave the sample and be detected. Consequently, they are very useful for an inspection of the topography of the sample's surface.

Backscattered electrons (BSE) are elastically reflected primary electrons. BSE have more energy than SE, and therefore they emerge from deeper locations within the specimen, and, consequently, the resolution of BSE images is less than SE images. The amount of BSE depends on the atomic number of atoms Z. The higher Z, the higher the electron density around the atom. This results in a higher reflectivity and a lighter contrast compared to atoms with a lower atomic number. The so-called Z-contrast is created. BSE are sensitive to chemical composition, and they are suitable for observing different phases.

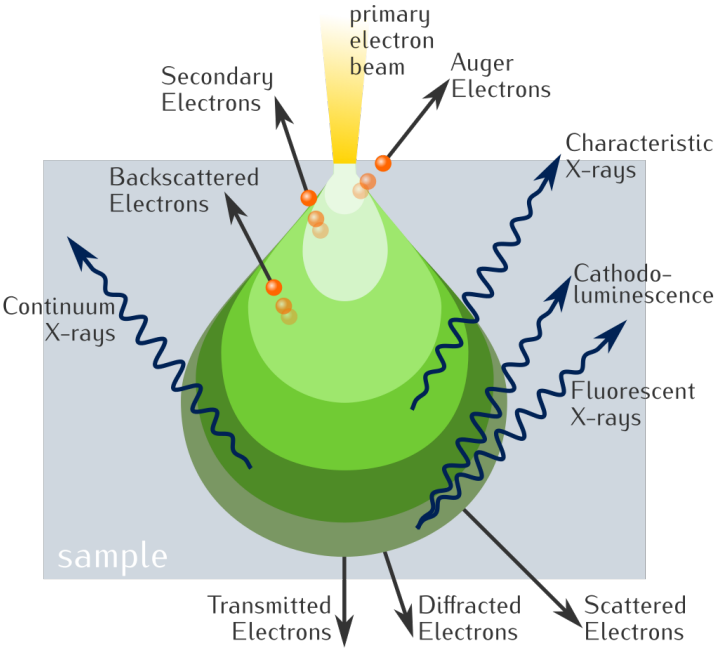

Figure 3.1: Schema of electron-solid interaction volumes [58].

When primary electrons interact with matter, X-rays are also produced. One of the types of X-rays is the so-called characteristic X-rays, which arise during the deexcitation of an atom. Since the energy levels in the atom are quantized and different for each element, the chemical composition of the sample can be determined by measuring the X-ray spectrum. Based on the intensity of different wavelengths, concentration of individual elements can be estimated. The method using this physical principle is called Energy-dispersive X-ray spectroscopy (EDS).
The microstructure was studied with SEM FEI Quanta 200F. The accelerating voltage was 5 keV.

3.2 Electron backscatter diffraction

Electron backscatter diffraction (EBSD) is a scanning electron microscope–based experimental technique using diffraction of backscattered electrons to determine crystallographic orientation at measured points.
Inelastically scattered BSE are scattered in all directions. The intensity of the scattered beam is greatest in its original direction and decreases with increasing angle. BSE may subsequently diffract on crystallographic planes if they satisfy Bragg's equation (Eq. 3.1):

$$2d_{hkl} \sin \theta = \lambda, \tag{3.1}$$

where d_{hkl} represents interplanar distance, θ Bragg's angle, and λ is de Broglie wavelength of the electron.
Electrons of the same wavelength diffract in two directions, 1 and 2. Part of the electrons from direction 1 diffracts into direction 2 and vice versa. The intensity of the diffracted beam is proportional to the intensity of the electrons in the individual directions. Thus, in direction 1, the intensity decreases because more electrons diffract in direction 2 than in direction 1. In direction 2 the intensity will be higher. In 3D space, the diffracted electrons form pair of so-called Kossel cones. On the screen of the EBSD detector are sections through these cones - two hyperbolas (dark and bright). Due to their great curvature, they can be considered as lines and they are called the Kikuchi lines.
Suppose the direction of the incident beam is almost parallel to the crystallographic planes. The intensity of the diffracted beam is almost the same in both directions and no pair of Kikuchi lines is formed. Instead, the strong dynamical diffraction effect creates a band of increased intensity between directions 1 and 2. This band is called the Kikuchi band. The formation of Kikuchi lines and Kikuchi bands is schematically shown in Fig 3.2.

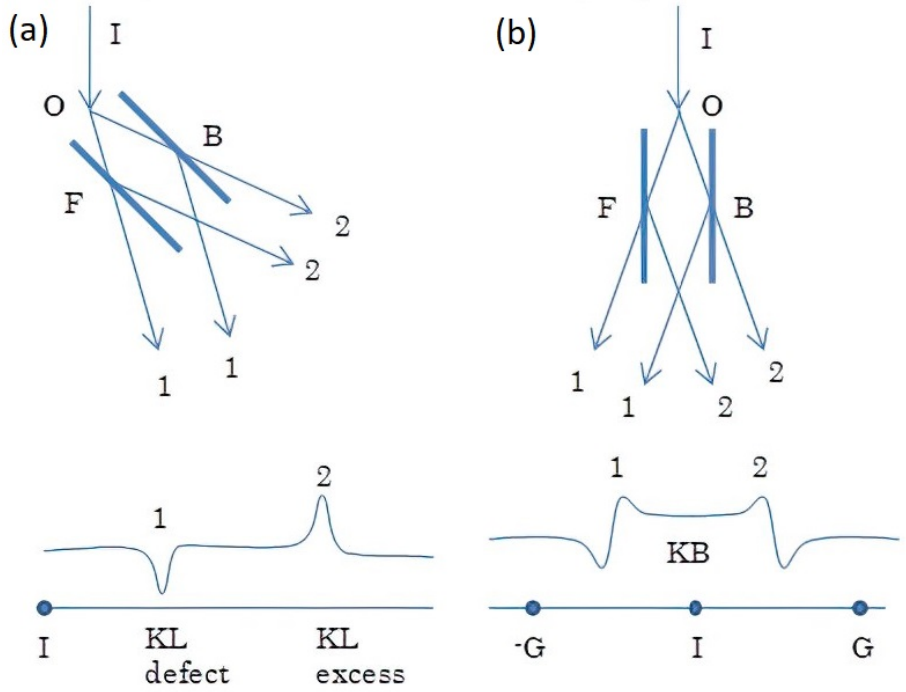

Figure 3.2: Schema of (a) Kikuchi lines and (b) Kikuchi bands formation [59].

In practice, diffraction occurs not only on one system of planes but on several systems. This gives an image of several Kikuchi lines/bands, the so-called Kikuchi pattern, see Fig. 3.3. The Hough transform is used for easier Kikuchi pattern analysis in determining the orientation of the investigated point. It assigns two characteristic values (angle and distance) to each line/band.
EBSD method is mainly used for the characterization of polycrystalline materials. Texture, grain size distribution, grains misorientation, and other material features can be obtained by this powerful method.
Scanning electron microscope FEI Quanta 200F equipped with an EBSD camera by EDAX was used for EBSD measurement. The accelerating voltage was 10 kV, and the step size 200 nm (100 nm for ECAP condition).

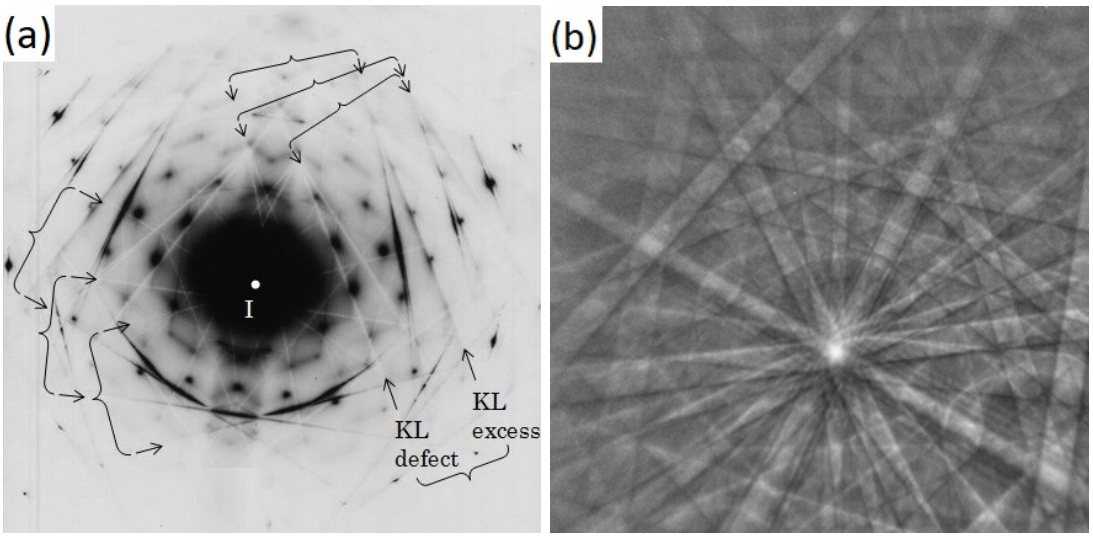

Figure 3.3: An example of (a) Kikuchi lines [59] and (b) Kikuchi bands [60].

3.3 Transmission electron microscopy

Transmission electron microscopy (TEM) uses beam of high energetic electrons. Unlike SEM, the electron beam passes through a very thin sample (less than 100 nm). There are many techniques and types of contrasts in modern transmission electron microscopes. For the purpose of this work, it will be sufficient to explain the principle of the scattering contrast and diffraction pattern.
Scattering contrast is created by the partial elimination of elastically scattered electrons by an objective aperture. Inelastically scattered electrons usually pass through this aperture and contribute to the image background. During elastic scattering, electrons interact with the electrostatic potential of atoms and are deflected from the original trajectory. Parts of the sample with a higher average atomic number Z, such as precipitates, scatter more and appear darker on the screen. Similarly, thicker areas of the sample scatter more electrons than thin ones and also appear darker.
The advantage of electron diffraction over X-ray diffraction is the ability to focus the electron beam on a very small area. In addition, a picture can be taken, or chemical analysis (EDS) can be measured at the same sample location. Crystalline materials have a periodic structure of atoms that appear as a diffraction grating. Because electrons also have a wave character, diffraction occurs on the crystal lattice, and a diffraction pattern is formed in the back focal plane of the microscope. The diffraction pattern is a Fourier transform of the electrostatic potential of all atoms. Based on it, we can determine the type of crystal lattice, including lattice parameters, and subsequently identify the phase.
An example of a precipitate and a diffraction pattern is shown in Fig. 3.4.

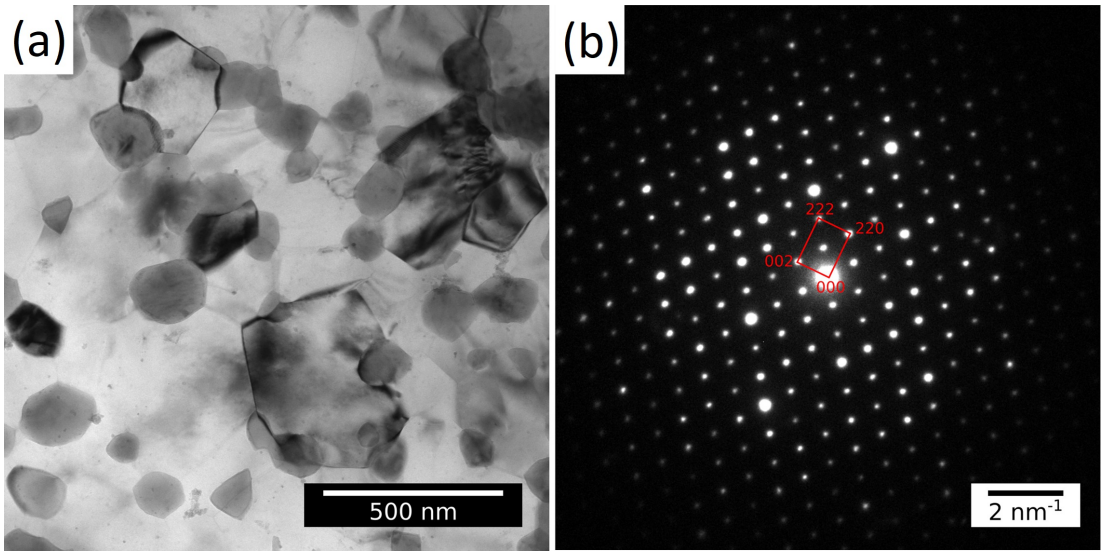

Figure 3.4: Mg_5RE precipitates in magnesium alloy (a) scattering contrast and (b) diffraction pattern [61].

Detailed microstructure analysis was performed using transmission electron microscopes Jeol 2200FS (Mg-4Y-4Gd-2Ca, ECAP condition) and JEOL 2000 FX (extruded Mg-2Y-2Gd-1Ca).

3.4 Deformation tests

Tensile/compression tests are a basic type of experiment characterizing the behaviour of material under applied stress. In the deformation test, the dependence of the applied load on the elongation of the sample is measured. Using the measured data and known sample dimensions, a stress-strain curve is constructed, from which the characteristic values of the investigated material are determined. A typical example of a stress-strain curve is shown in Fig. 3.5. The linear part of the deformation curve belongs to the elastic deformation. When deviating from the linear part, plastic deformation occurs. The parameter characterizing the minimum stress in which plastic deformation occurs is called yield stress. It is defined as the stress at 0.2 % of plastic strain. UTS (ultimate tensile strength) is the maximum on the engineering tensile stress-strain curve. UCS (ultimate compressive strength) is defined analogously.

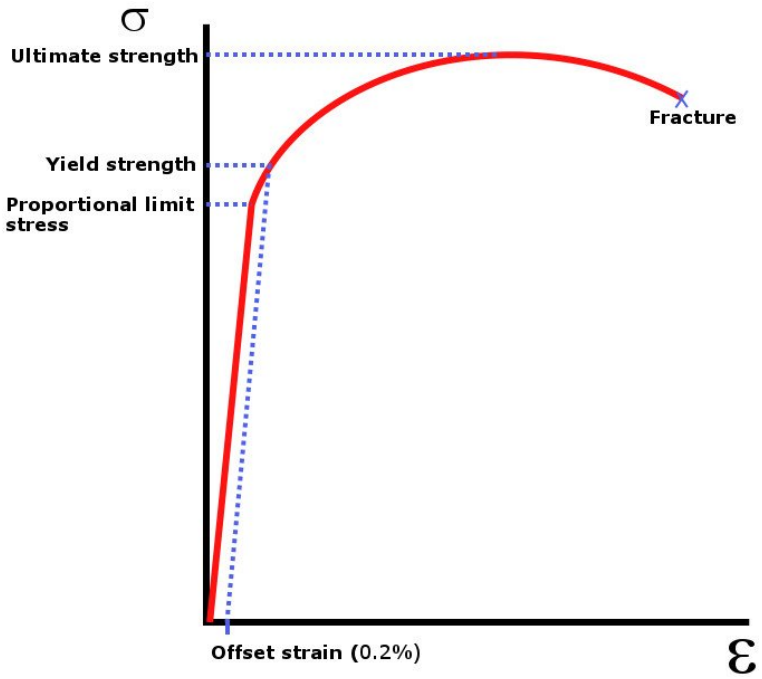

Figure 3.5: Stress-strain curve [62].

Tensile and compressive tests were measured on Instron 5882 equipped with an extensometer. Compressive tests were measured on at least three samples, tensile tests on two. In the case of tensile tests (except ECAP condition), an extensometer was used. The measurement was performed at room temperature with a strain rate 10^{-3} s^{-1}.

3.5 Microhardness measurement

Microhardness measurement is one of the experimental methods characterizing mechanical properties. Microhardness testing consists of making an indentation on the sample by a diamond indenter. The sample's surface should be thoroughly polished, strain-free, and perpendicular to the indentation axis.

There are several types of indenters of different shapes. One of the most common is the pyramidal Vickers-type with interfacial angle 136°, see Fig. 3.6. A calibrated optical microscope is used to determine the size of the resultant indentation d [63].

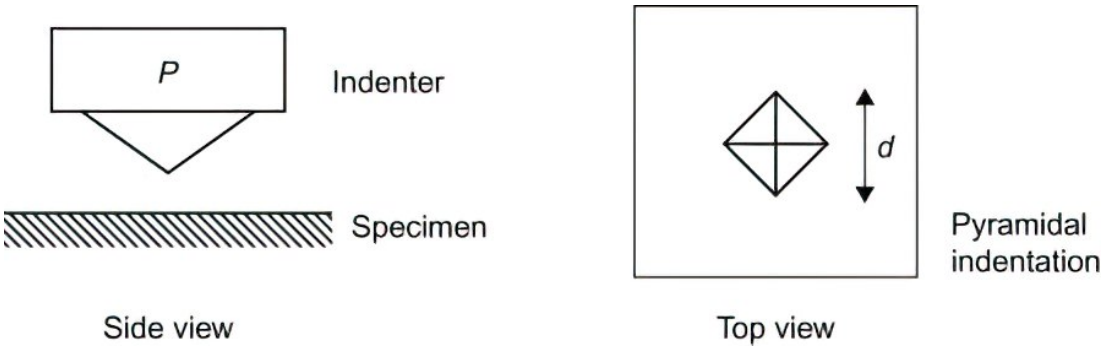

Figure 3.6: Scheme of indentation [63].

The Vickers microhardness HV is given by Eq. (3.2):

$$HV = 1.854.4\frac{P}{d^2}[\text{kgf.mm}^{-2}], \tag{3.2}$$

where P represents the load expressed in units of gram force and d is the arithmetic mean of the lengths of the indentation diagonals in micrometres.
Usually, several tens of measurements are performed to obtain a sufficient statistical set or to characterize the microhardness at multiple locations in the sample. Vickers microhardness was measured by Qness Q10 with a load of 10 N for 10 seconds in the transverse section. At least 100 (ER25), 230 (ER11) or 430 (ECAP) indentations were evaluated for each condition.

3.6 Differential scanning calorimetry

Differential scanning calorimetry (DSC) is an experimental method by which heat capacity, heat of transition, purity, and glass transition can be determined. DSC curves also serve to identify substances, set up phase diagrams and determine degrees of crystallinity. DSC is based on measuring the change of the difference in the heat flow rate to the sample and a reference sample while they are subjected to a controlled temperature program. A material whose heat capacity is known and does not undergo any phase transformation in the measured temperature range is used as a reference [64].
There are several types of DSC. One of the most used is the heat flux DSC, see Fig. 3.7. The measuring cell consists of two pans connected by a thermal bridge (for the sample and the reference) and sensors measuring the temperature difference and the absolute temperature. The cell is usually filled with inert gas. The primary measurement signal is a temperature difference that determines the intensity of the exchange, and the resulting heat flow rate is proportional to it [64]. During measurement, if no thermal processes occur in the material, the DSC signal is proportional to the sample's heat capacity. The first-order phase transition is associated with heat absorption/emission. This displays a peak in the DSC

curve. The area under the peak is proportional to the heat absorbed/emitted during the phase transition. Second-order phase transition associated with abrupt change in heat capacity is detected as a step change in the DSC curve [65].

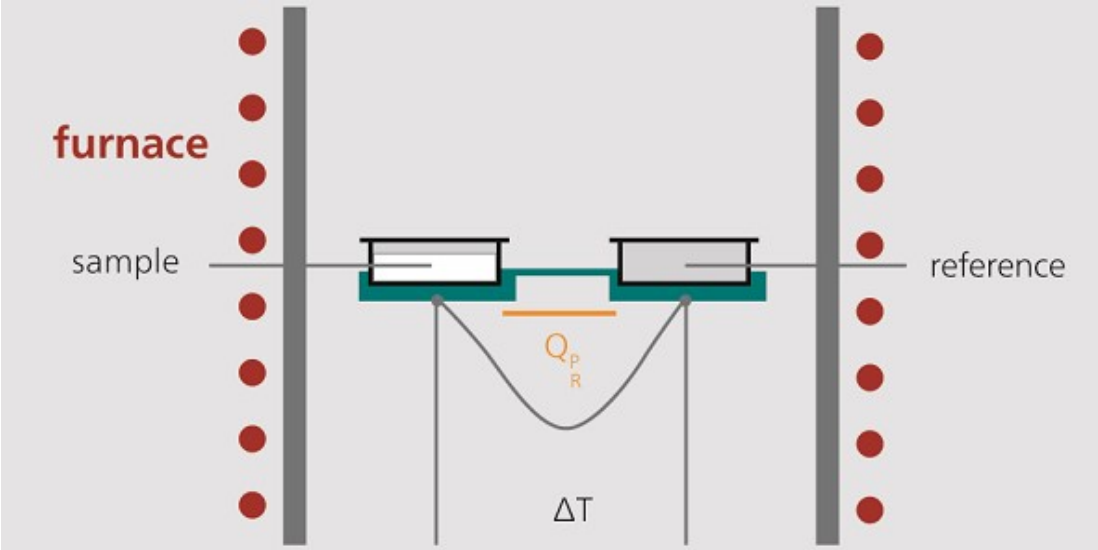

Figure 3.7: Scheme of heat flux DSC [66]

Heat flux Netzsch DSC 404 C Pegasus was used for DSC measurement. The temperature profile was 100 °C → 550 °C → 100 °C, 5 °C/min, measured in inert Ar atmosphere.

3.7 Samples preparation

Samples for SEM and EBSD measurement were cut by ATM Brillant 220 saw into three millimetres thick slices and ground using SiC abrasive papers (P4000). Then they were polished using diamond paste with particles of about 0.25 μm. In the end, EtosilE containing particles of about 0.06 μm was used. For EBSD observation, samples were additionally ion polished by Leica EM RES102. Samples prepared for SEM observation were also used for microhardness measurement.
Samples for TEM observation were first cut to one millimetre thick slices and ground by SiC paper (P1200) on both sides to 150 μm thickness. Then disks three millimetres in diameter were cut. Subsequently, approximately 100 μm deep hollow was ground into them. In the end, the centre of the disks was ion polished until a small hole was made. The scheme of sample preparation is shown in Fig. 3.8.

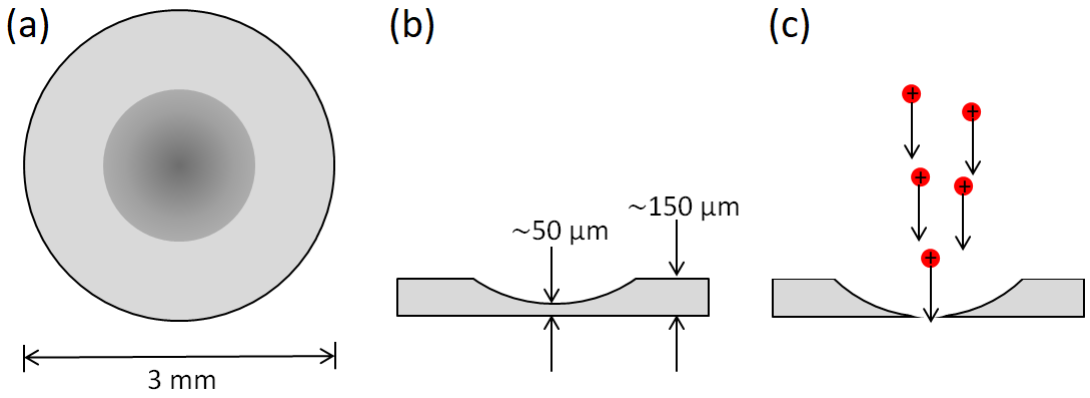

Figure 3.8: TEM sample preparation: (a) a sample with a ground hollow (top view), (b) sample with ground hollow (side view), (c) final form sample (side view).

Samples for deformation tests were machined by a lathe due to their circular cross-section. ECAP condition tensile samples were cut using ATM saw and processed by CNC machine due to limited amount of material. Both samples for compression and tensile tests, were machined with the longest side parallel to the extrusion (ECAP) direction. The scheme of samples, including dimensions, is shown in Fig. 3.9.

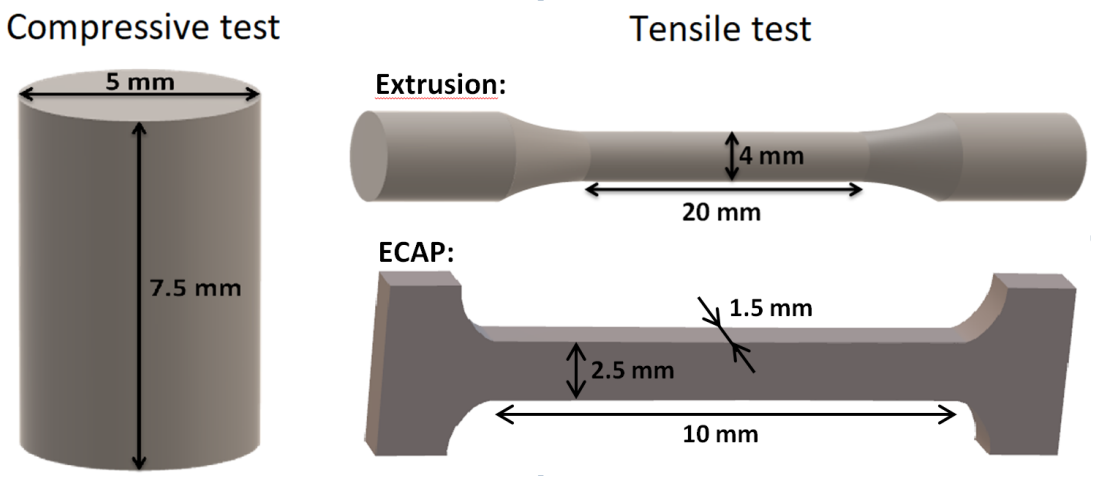

Figure 3.9: Deformation tests samples.

4. Experimental material and aims of the thesis

4.1 Experimental material

Two quaternary magnesium alloys further referred to as Mg-4Y-4Gd-2Ca and Mg-2Y-2Gd-1Ca have been used in this thesis.

4.1.1 Mg-4Y-4Gd-2Ca processed by extrusion

The exact composition of the alloy (4.5 % Gd, 3.4 % Y, and 2.6 % Ca, in wt. %) was determined by EDS. All elements were melted at 750 °C under a protective Ar atmosphere and homogenized for 10 minutes. Then they were cast into a cylindrical brass mould with a 50 mm diameter. After casting, solution annealing was performed at 480 °C for 16 hours and subsequently quenched in water.
The alloy thus prepared was extruded at two different temperatures (350 °C and 400 °C) with two extrusion ratios (11 and 25). The extrusion rate was 0.02 $m.s^{-1}$. Labels of extruded conditions and parameters of processing are summarized in Tab. 4.1.

Label	Heat-treatment	Extrusion ratio	Extrusion temperature
Ex350-ER11	480 °C for 16 h	11	350 °C
Ex350-ER25	480 °C for 16 h	25	350 °C
Ex400-ER11	480 °C for 16 h	11	400 °C
Ex400-ER25	480 °C for 16 h	25	400 °C

Table 4.1: Labels and processing parameters of extruded conditions of Mg-4Y-4Gd-2Ca.

4.1.2 Mg-2Y-2Gd-1Ca processed by extrusion

The exact composition of the alloy (2.0 % Y, 1.9 % Gd, and 1.1 % Ca, in wt. %) was determined by EDS. The alloy Mg-2Y-2Gd-1Ca was cast and heat-treated under the same conditions as Mg-4Y-4Gd-2Ca. Then it was extruded at two different temperatures (300 °C and 350 °C). The extrusion ratio (11 and 25) and the extrusion rate (0.02 $m.s^{-1}$) were like in the case of Mg-4Y-4Gd-2Ca. Labels of extruded conditions and parameters of processing are shown in Tab. 4.2.

Label	Heat-treatment	Extrusion ratio	Extrusion temperature
Ex300-ER11	480 °C for 16 h	11	300 °C
Ex300-ER25	480 °C for 16 h	25	300 °C
Ex350-ER11	480 °C for 16 h	11	350 °C
Ex350-ER25	480 °C for 16 h	25	350 °C

Table 4.2: Labels and processing parameters of extruded conditions of Mg-2Y-2Gd-1Ca.

4.1.3 Mg-2Y-2Gd-1Ca processed by ECAP

Only Mg-2Y-2Gd-1Ca alloy was processed by ECAP. Mg-2Y-2Gd-1Ca is more promising due to the lower price caused by the lower concentration of RE-metals. Within this project, the emphasis was mainly on high ignition temperature and, despite the twice lower concentration of alloying elements, it reaches only 150 °C lower ignition temperature than Mg-4Y-4Gd-2Ca.
Because the extruded conditions showed signs of insufficient solution annealing temperature (large Mg_2Ca precipitates), DSC curves were measured on both alloys to determine (Mg)+Mg_2Ca $\leftrightarrows$ (Mg) phase transition temperature, see Fig. 4.1. Based on the measurement, the alloy was annealed at 525 °C for 16 hours in order to homogenize the chemical composition to assure successful ECAP processing.

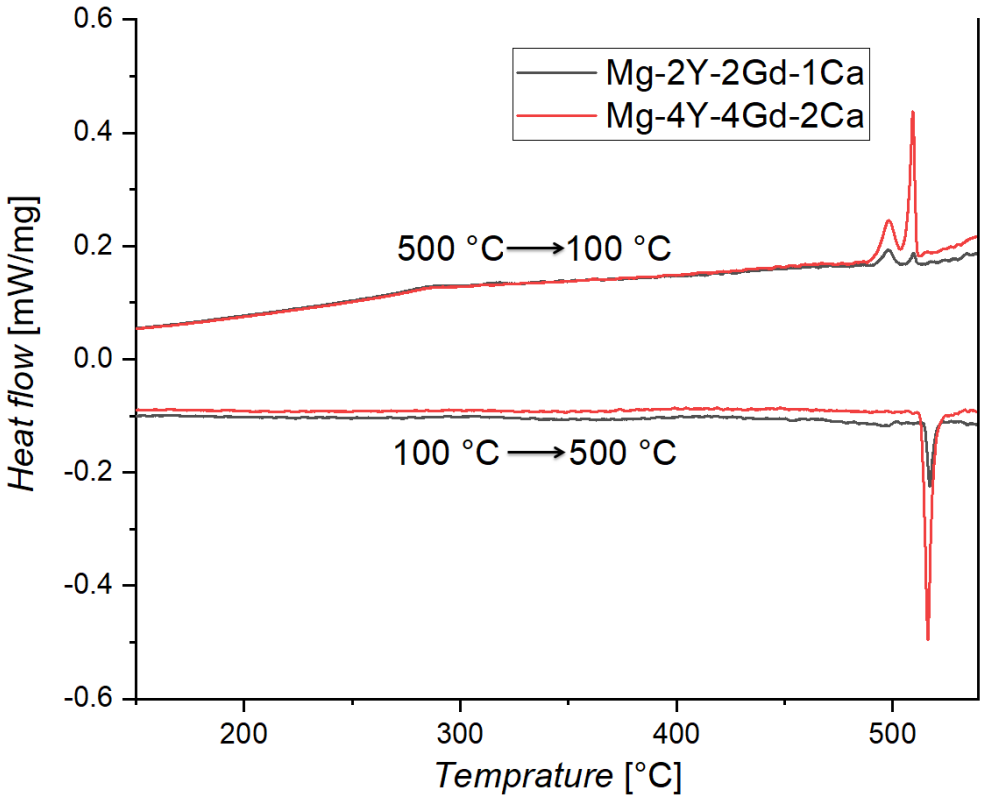

Figure 4.1: DSC curves of investigated alloys.

Billets with square cross-section and length of 10 cm were processed by ECAP, following route B_C. Die had the inner angle $\phi = 90°$ and the angle of curvature $\phi = 0°$. Eight passes of ECAP were performed, after which saturation of the microstructure was observed in similar alloys [61,67]. Processing temperature and pressing speed were chosen based on experience with Mg-4Y alloy, see Tab. 4.3.

ECAP pass number	1	2	3	4	5	6	7	8
Processing temperature [°C]	340	325	315	305	300	295	290	290
Pressing speed [mm/min]	2	3	5	7	7	7	7	7

Table 4.3: ECAP procedure parameters.

The condition processed by ECAP will be further referred to as ECAP condition.

5. Results

5.1 Mg-4Y-4Gd-2Ca after extrusion

5.1.1 Secondary phase particles

The microstructure was studied by SEM (BSE, EDS) and TEM. No differences in the number, composition, or distribution of the precipitates were observed for different conditions. Fig. 5.1 and 5.2 show micrographs of Ex350-ER25. Secondary phases were determined on the basis of local chemical analysis using EDS and electron diffraction.

Mg_2Ca precipitates

The Mg_2Ca particles are aligned in the direction of extrusion, see Fig. 5.1 (a). Large particles (∼4 µm) of Mg_2Ca phase were observed, see Fig. 5.1 (a-b) and Fig. 5.2 (b). Small precipitates were also present and they are highlighted in a circle in Fig 5.1 (b). Tiny particles of the same phase at grain boundaries and in the form of coherent precipitates within the grains were observed by TEM, see Fig. 5.2 (a-b). This phase usually forms due to the limited solubility of Ca in the Mg matrix [68, 69]. It occurs when large intermetallic particles formed after casting are fragmented and stretched during the extrusion process.

REH_2 and Mg_5RE precipitates

Particles rich in RE-metals were also observed. Specifically, REH_2 with different content of Y and Gd in individual particles (Fig. 5.1 (b) and Fig. 5.2 (c)). Mg_5RE are also present in the form of particles growing from the surface of Mg_2Ca or REH_2 precipitates, see Fig 5.2 (c). Despite the high concentration of yttrium and gadolinium, particles rich in these elements are relatively few. Based on this, it can be concluded that most of the Gd and Y atoms are dissolved in the magnesium matrix and only a small amount of MgRE intermetallic particles formed during the extrusion process and subsequent cooling.

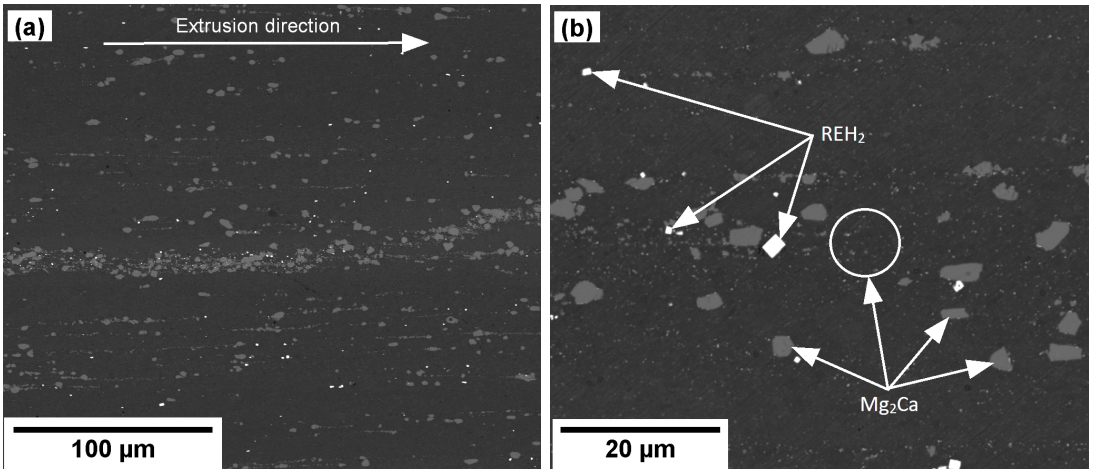

Figure 5.1: SEM micrographs of extruded Mg-4Y-4Gd-2Ca.

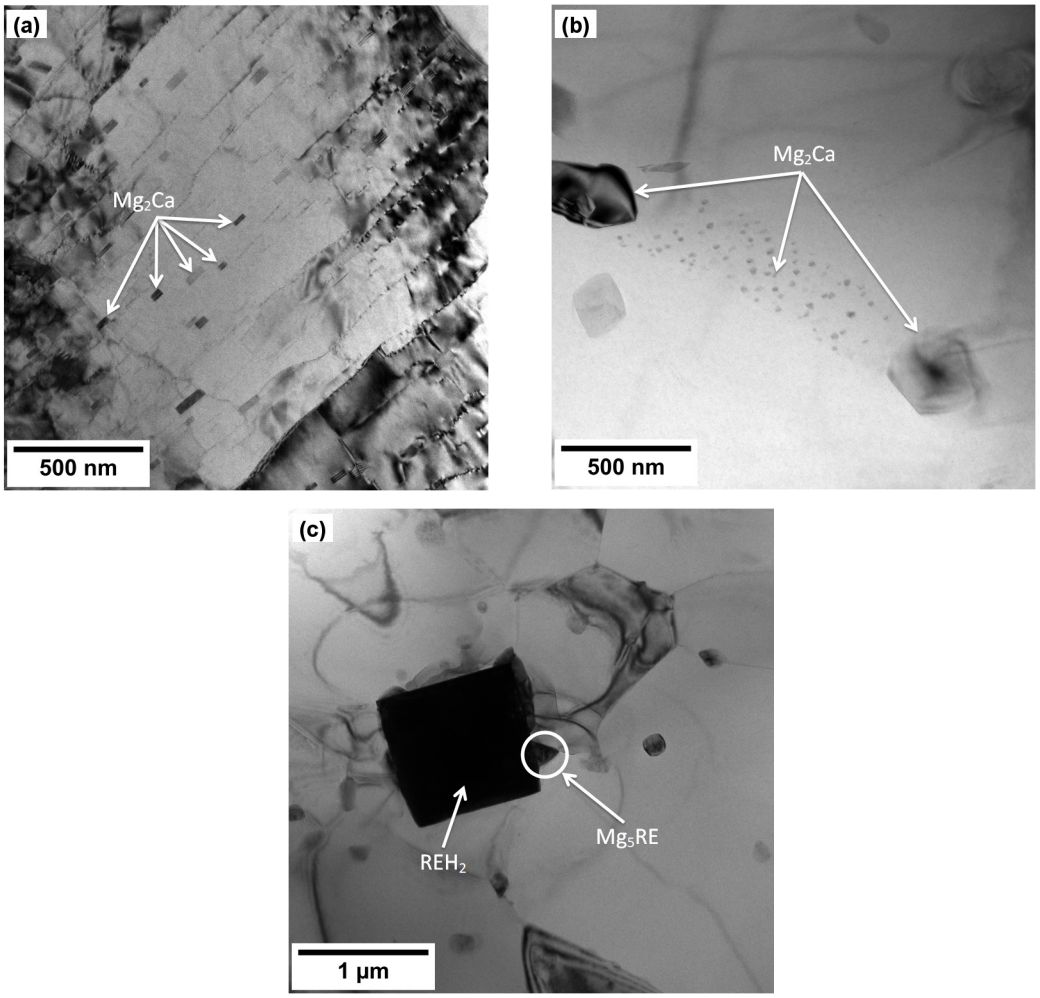

Figure 5.2: TEM micrographs of extruded Mg-4Y-4Gd-2Ca showing (a) tiny Mg_2Ca coherent precipitates (b) Mg_2Ca incoherent precipitates, and (c) large REH_2 particle with small Mg_5RE growing on its surface.

5.1.2 Grain microstructure

EBSD was measured for each extruded condition in three different sections of the extruded bar. Two measurements were performed in section perpendicular to the extrusion direction - in the middle and on the edge, referred to as TS (transverse middle section) and ES (transverse edge section). The third measurement was performed on a section parallel to the extrusion direction in the middle of the extruded rod, referred to as LS (longitudinal section). The scheme of sections TS, ES, and LS is shown in Fig. 5.3.

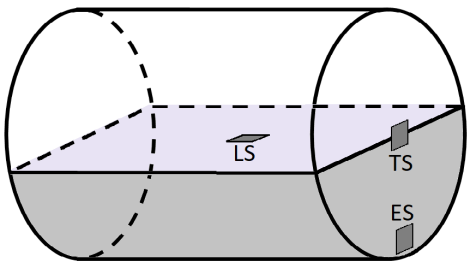

Figure 5.3: Three different sections of the EBSD measurement.

Fig. 5.4 shows IPF maps of all four extruded conditions measured in TS. In the case of extrusion temperature of 350 °C (Ex350), the resulting microstructure was significantly affected by the extrusion ratio. The microstructure of Ex350-ER11 is bimodal with a high fraction of non-recrystallized grains. The grain size of the recrystallized grains is 2.5 µm in diameter. Ex350-ER25 led to fine-grained, almost fully recrystallized microstructure with small recrystallized grains - 2.3 µm. Extrusion at higher temperature (400 °C) led to almost completely recrystallized (Ex400-ER11) and wholly recrystallized (Ex400-ER25) microstructure with an average grain size of 5.6 µm for both conditions.

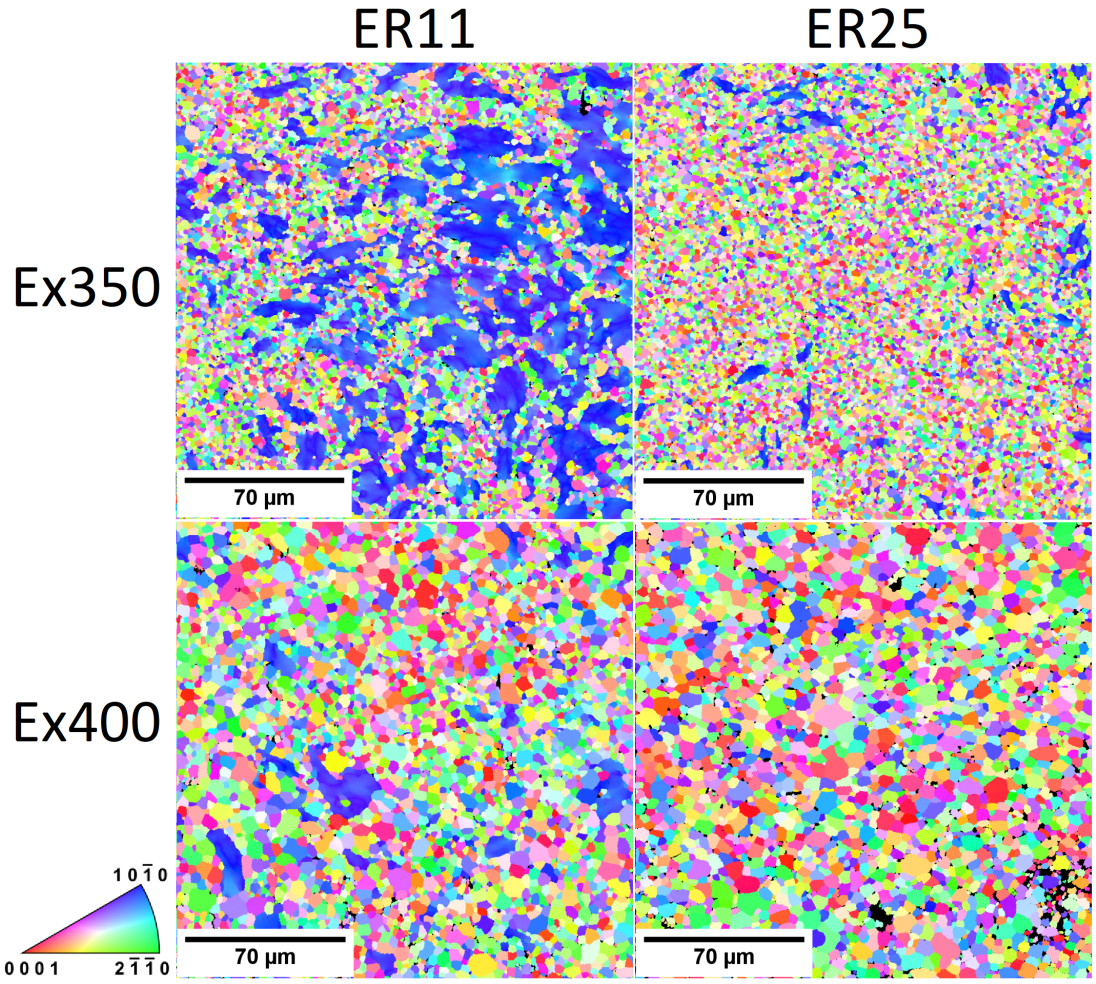

Figure 5.4: IPF orientation maps of extruded Mg-4Y-4Gd-2Ca measured in TS.

IPF maps measured in LS are shown in Fig. 5.5. Non-recrystallized grains are observed in all conditions except Ex400-ER25, which is consistent with the TS observations. These large grains are significantly elongated in the extrusion direction.

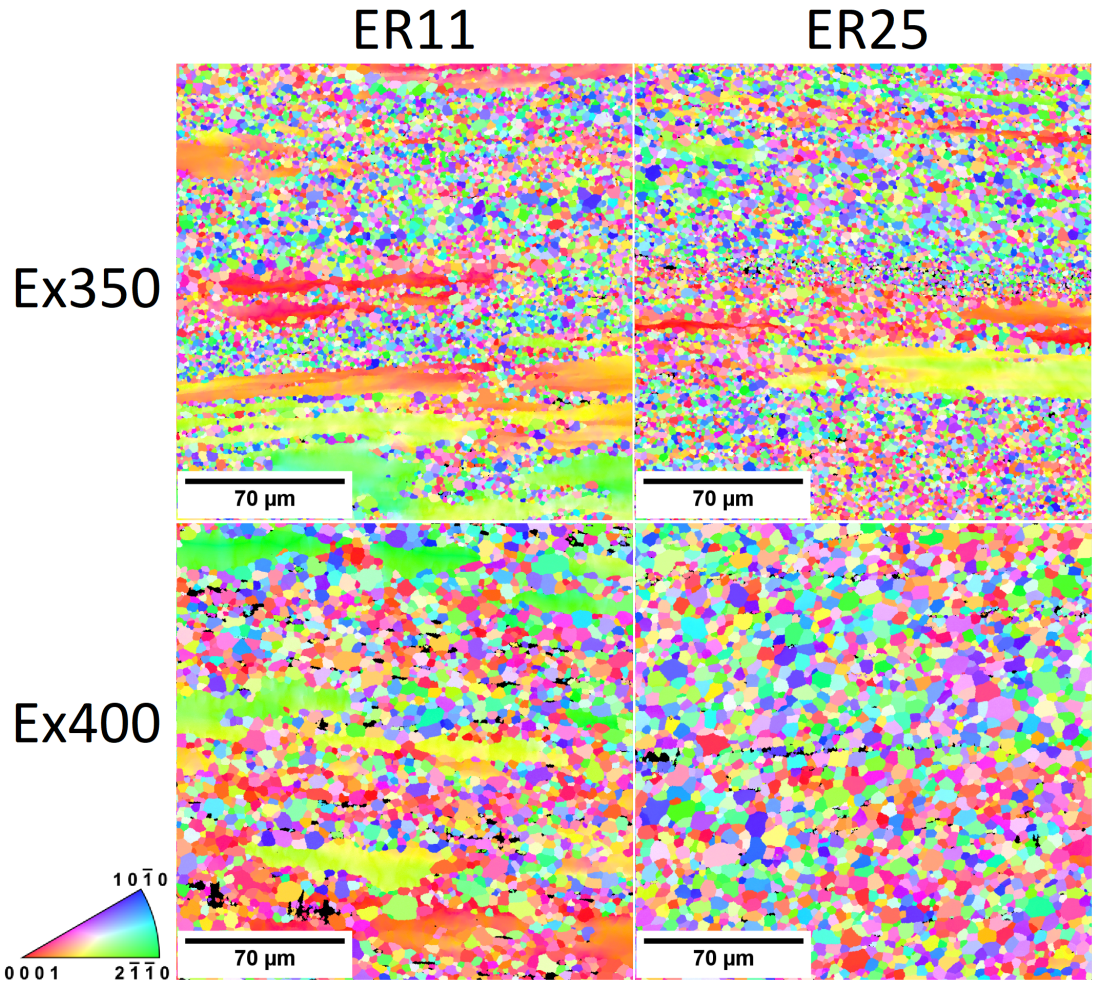

Figure 5.5: IPF orientation maps of extruded Mg-4Y-4Gd-2Ca measured in LS.

EBSD was also measured in ES, see Fig. 5.6. The finer microstructure and the higher degree of recrystallization near the edge are probably caused by frictional effect and higher strain near the contact of the extruded material and the die. Unlike the microstructure measured in TS of the Ex350 conditions, grains are completely recrystallized, but the average grain size of recrystallized grains remained almost the same - 2.5 μm (Ex350-ER11) and 2.2 μm (Ex350-ER25). In the Ex400-ER11 condition, there are no non-recrystallized grains. The microstructure of the Ex400-ER25 condition is fully recrystallized both near the edge (Fig. 5.6) and in the center (Fig. 5.5). It can be concluded that the microstructure of Ex400-ER25 condition is homogeneous. The mean grain size of Ex400 conditions measured in ES is 4.8 μm (Ex400-ER11) and 5.6 μm (Ex400-ER25).

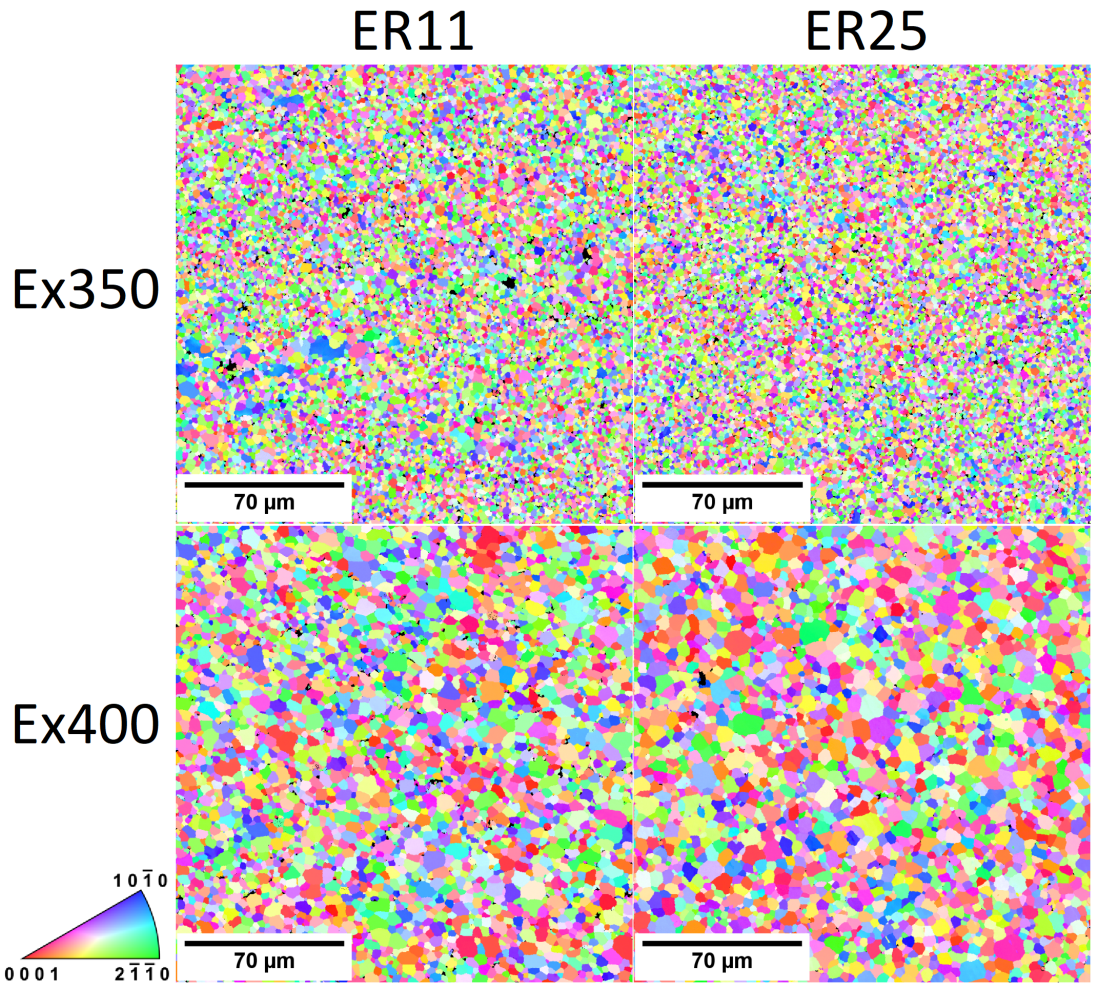

Figure 5.6: IPF orientation maps of extruded Mg-4Y-4Gd-2Ca measured in ES.

5.1.3 Texture

Recrystallized grains

Fig. 5.7 shows pole figures of recrystallized grains measured on TS. Recrystallized grains were selected based on grain size (<5 μm). The textural component typical for RE-alloyed magnesium alloys having a c-axis rotated by ∼45° from the extrusion direction is observed in all conditions. Also, weak texture overall is typical for magnesium alloys containing rare earth elements [70–72]. There is a clear connection between the texture of the non-recrystallized grains and the recrystallized grains of Ex350-ER11. The RE texture appears to form gradually during recrystallization. Almost fully recrystallized condition Ex350-ER25 shows a complete RE texture, while in semi-recrystallized Ex350-ER11 condition, this texture component is not fully developed. A weak unusual {0001} texture component is present in all conditions except Ex350-ER11.

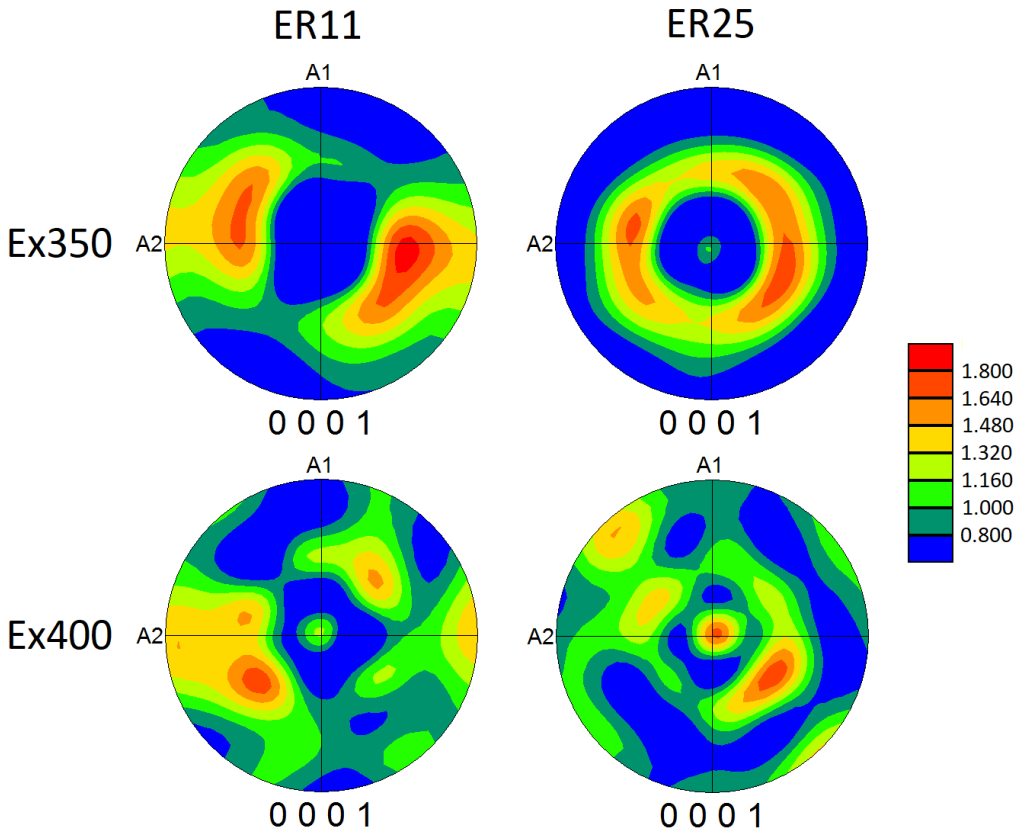

Figure 5.7: Pole figures of recrystallized grains calculated from the EBSD data measured in TS of extruded Mg-4Y-4Gd-2Ca.

Non-recrystallized grains

From Fig. 5.4, it is clear that the non-recrystallized grains have a strong $\{10\bar{1}0\}$ texture, thus with the decreasing proportion of non-recrystallized grains decreases the overall intensity of $\{10\bar{1}0\}$ texture component. Pole figures of Ex350-ER11 are shown in Fig. 5.8. The symmetrical textural component (see $\{10\bar{1}0\}$ pole figure in Fig. 5.8) is related to other prismatic planes being tilted by 30°. Strong $\{10\bar{1}0\}$ texture is typical for non-recrystallized grains of extruded magnesium alloys [73, 74].

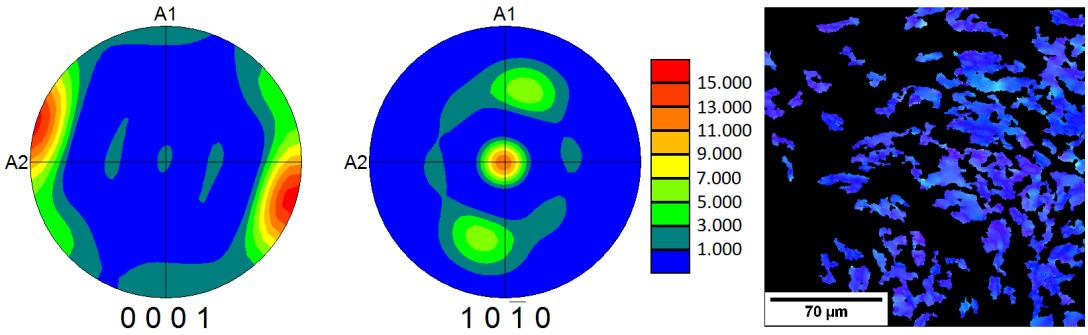

Figure 5.8: Pole figures and IPF map of non-recrystallized grains of Ex350-ER11 calculated from the EBSD data measured in TS.

5.1.4 Mechanical properties

Tensile and compressive tests

Representative stress-strain curves of compressive tests are shown in Fig. 5.9. There is no significant difference between conditions extruded at the same temperature. YCS and UCS are higher for Ex350 conditions. It is probably related to the grain boundary strengthening (Hall-Petch relation) and higher content of the deformed non-recrystallized grains with potentially high dislocation density. Compressive stress-strain curve of Ex350-ER11 shows slightly sigmoidal character (convex between $\varepsilon = 0.06$ and $\varepsilon = 0.10$). Such flow curve shape is related to twinning. Microstructure of Ex350-ER11 contains large non-recrystallized grains. These grains with a significant $\{10\bar{1}0\}$ texture component have a low Schmid factor for a basal slip but with the c-axis perpendicular to applied stress are ideally oriented for $\{10\bar{1}2\}$ twinning in compression [75, 76].

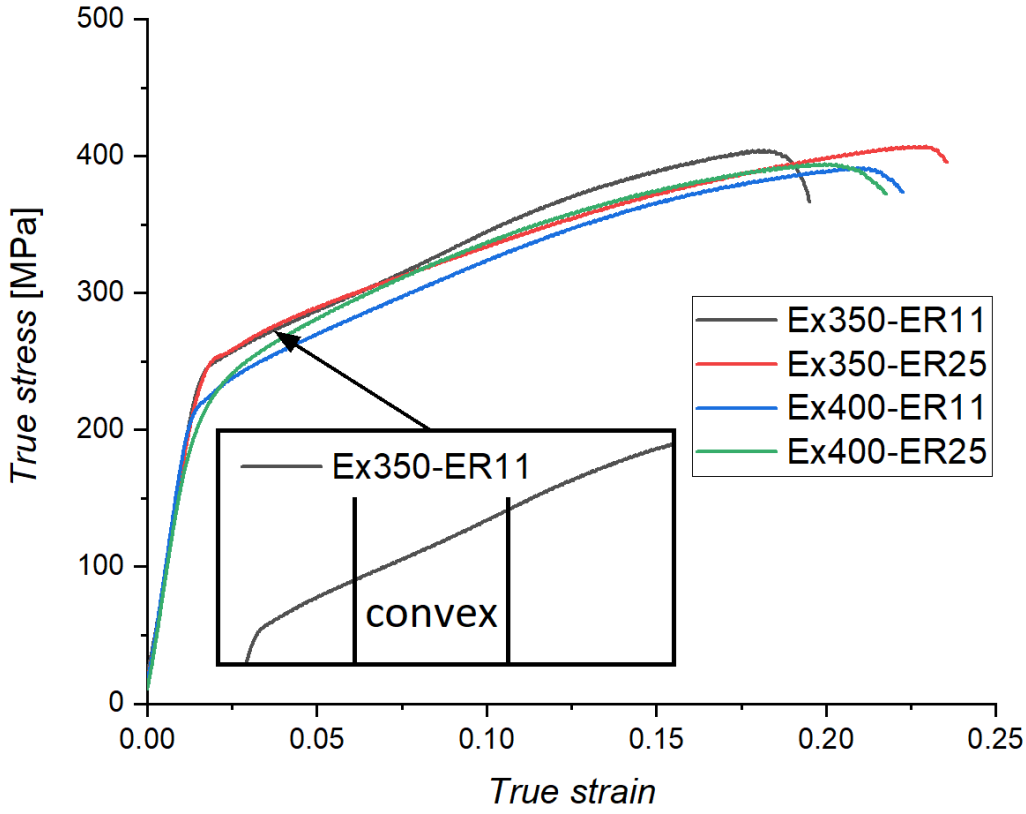

Figure 5.9: Compressive stress-strain diagrams of extruded Mg-4Y-4Gd-2Ca.

Tensile stress-strain curves are shown in Fig. 5.10. As in the case of compressive tests, Ex350 conditions exhibit higher YTS and UTS. YTS matches within the error YCS except Ex350-ER11 condition, which is slightly higher. It is caused by a higher fraction of grains orientated with c-axis perpendicular to the applied load and thus not preferred for basal slip or twinning in tension. Tensile stress-strain curves show sigmoidal character (except Ex400-ER11), with Ex400-ER25 being the most distinct. This is consistent with the texture analysis, see Fig. 5.7, where the {0001} texture component suitable for tensile twinning is present in both Ex400 conditions, while it is strongest in the condition Ex400-ER25. The values of YTS (YCS) and UTS (UCS) are shown in Tab. 5.1.

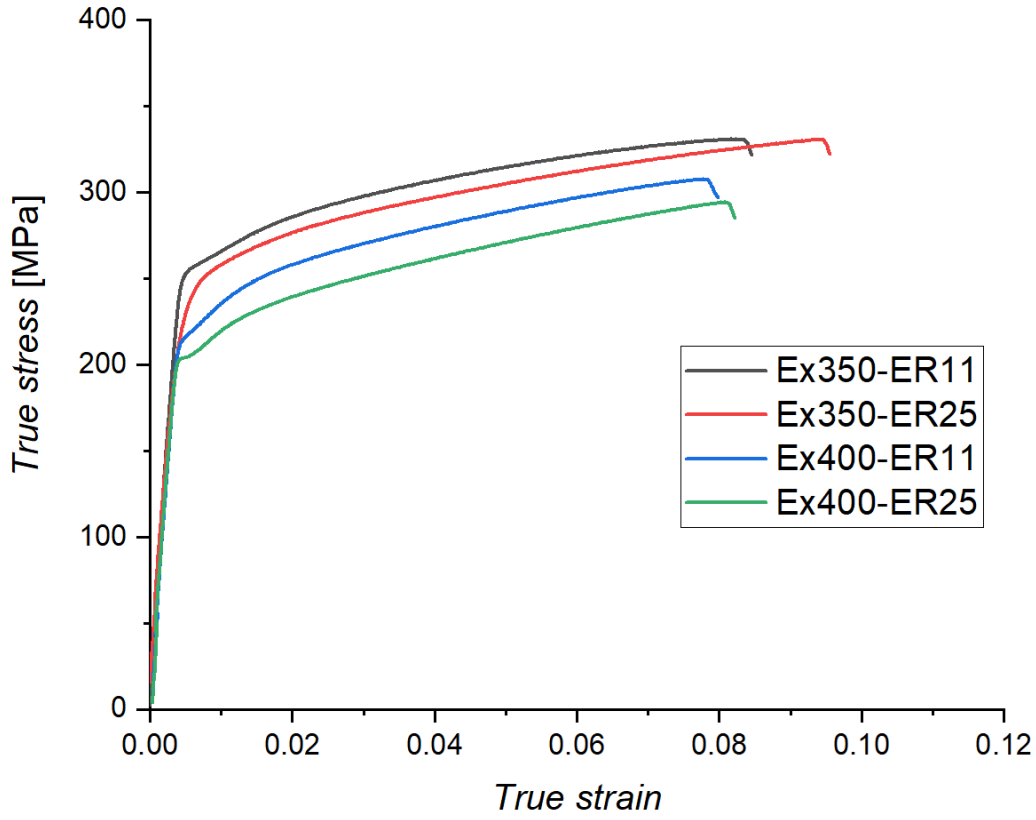

Figure 5.10: Tensile stress-strain diagrams of extruded Mg-4Y-4Gd-2Ca.

Microhardness measurements

It is clear from the microhardness maps shown in Fig. 5.11 that the microhardness is not homogeneous over the whole cross-section. For each condition, microhardness values are lower in the center of samples even in the completely recrystallized Ex400-ER25. It has been proven that during extrusion, the material flow velocity is not the same for all locations in cross-section. At the interface extruded material-die, the flow rate is lower due to friction effects [77]. This results in strain accumulation, which leads to an increase in dislocation density which promotes recrystallization. This eventually leads to a smaller grain size [78]. The average values of microhardness are stated in Tab. 5.1.

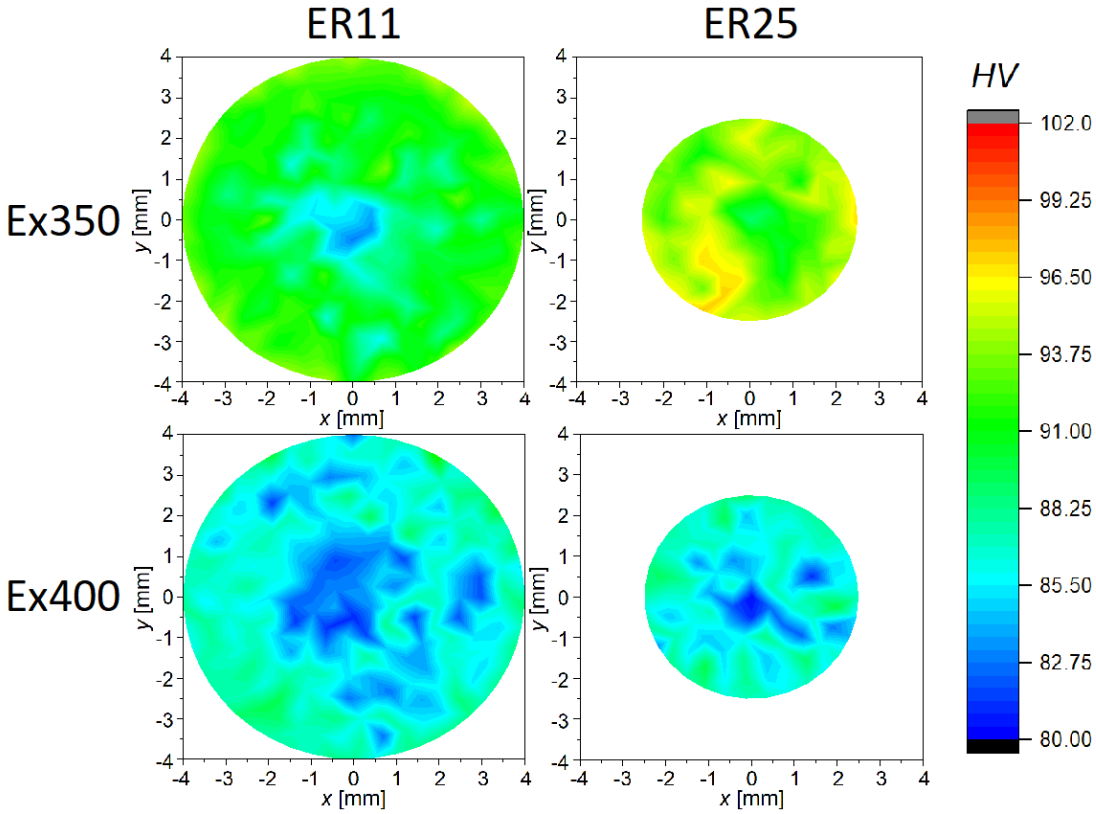

Figure 5.11: Microhardness maps of extruded Mg-4Y-4Gd-2Ca.

Material	*YCS* [MPa]	*UCS* [MPa]	*YTS* [MPa]	*UTS* [MPa]	*HV*
Ex350-ER11	244 ± 6	490 ± 11	257 ± 6	306 ± 7	91 ± 2
Ex350-ER25	246 ± 7	512 ± 13	242 ± 8	301 ± 9	94 ± 2
Ex400-ER11	220 ± 7	464 ± 14	220 ± 5	282 ± 8	86 ± 2
Ex400-ER25	207 ± 8	466 ± 15	205 ± 5	273 ± 7	86 ± 2

Table 5.1: Evaluated mechanical properties of Mg-4Y-4Gd-2Ca.

5.2 Mg-2Y-2Gd-1Ca after extrusion

5.2.1 Secondary phase particles

Mg-2Y-2Gd-1Ca alloy was processed by extrusion at two different temperatures - Ex300 and Ex350 using two different extrusion ratios ER11 and ER25. No differences in the precipitation microstructure were observed for individual conditions. Therefore only SEM micrographs of Ex300-ER11 (Fig. 5.12) and TEM micrographs of Ex350-ER11 (Fig. 5.13) are shown. Secondary phases were determined based on local chemical analysis using EDS and electron diffraction.

Mg_2Ca precipitates

The Mg_2Ca particles are aligned in the direction of extrusion, see Fig. 5.12 (a) as already observed in other alloys processed by extrusion [79, 80] and in Mg-4Y-4Gd-2Ca (Fig. 5.1 (a)). Large particles (∼3 μm) of Mg_2Ca phase were observed, see Fig. 5.12 (b), Fig. 5.13 (b). Smaller incoherent Mg_2Ca particles were observed by TEM (Fig. 5.13 (b)) as well as coherent ones within the grains, see Fig 5.13 (a). Although Mg-2Y-2Gd-1Ca alloy contains lower concentration of Ca, a large number of precipitates forms due to the limited solubility of Ca in the Mg matrix [68, 69].

REH_2 precipitates

A small amount of particles rich in RE-metals were observed (Fig. 5.12 (b), Fig. 5.13 (b)). Specifically, REH_2 with different content of Y and Gd in individual particles. No other particles containing RE metals were observed, although the presence of small amounts (e.g., Mg_5RE) cannot be excluded. Similarly to the Mg-4Y-4Gd-2Ca alloy, most Y and Gd atoms are dissolved in the Mg matrix. Due to the half concentration of these elements, a smaller amount of particles containing these atoms precipitated during the extrusion process and subsequent cooling.

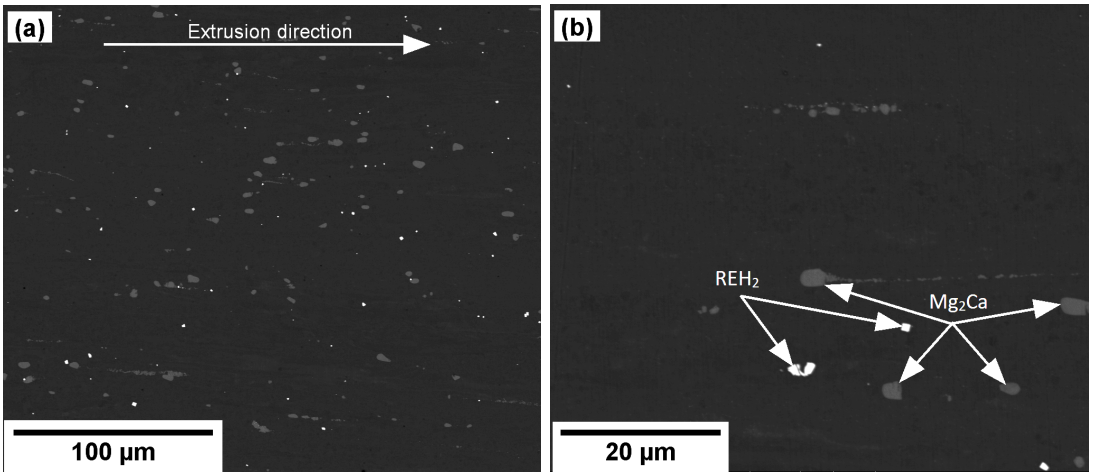

Figure 5.12: SEM micrographs of extruded Mg-2Y-2Gd-1Ca.

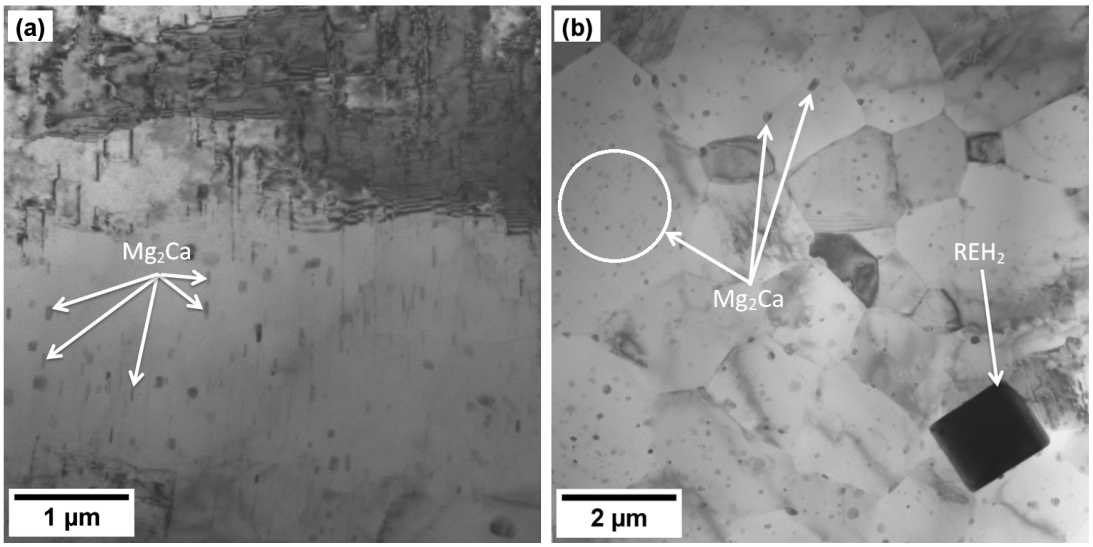

Figure 5.13: TEM micrographs of extruded Mg-2Y-2Gd-1Ca showing (a) tiny Mg_2Ca coherent precipitates (b) Mg_2Ca incoherent precipitates, and REH_2 particle.

5.2.2 Grain microstructure

IPF maps measured in TS are shown in Fig. 5.14. Microstructure of ER11 conditions is bimodal with a high fraction of non-recrystallized large grains surrounded by small recrystallized ones. These recrystallized grains are smaller for Ex300-ER11 (1.7 μm) than for Ex350-ER11 (2.2 μm). The microstructure of both ER25 conditions is bimodal. Despite the lower temperature of extrusion, the portion of recrystallized grains is higher in Ex300-ER25 than Ex350-ER25. Similarly to the ER11 conditions, the recrystallized grain size increases with increasing temperature (2.0 μm and 2.8 μm).

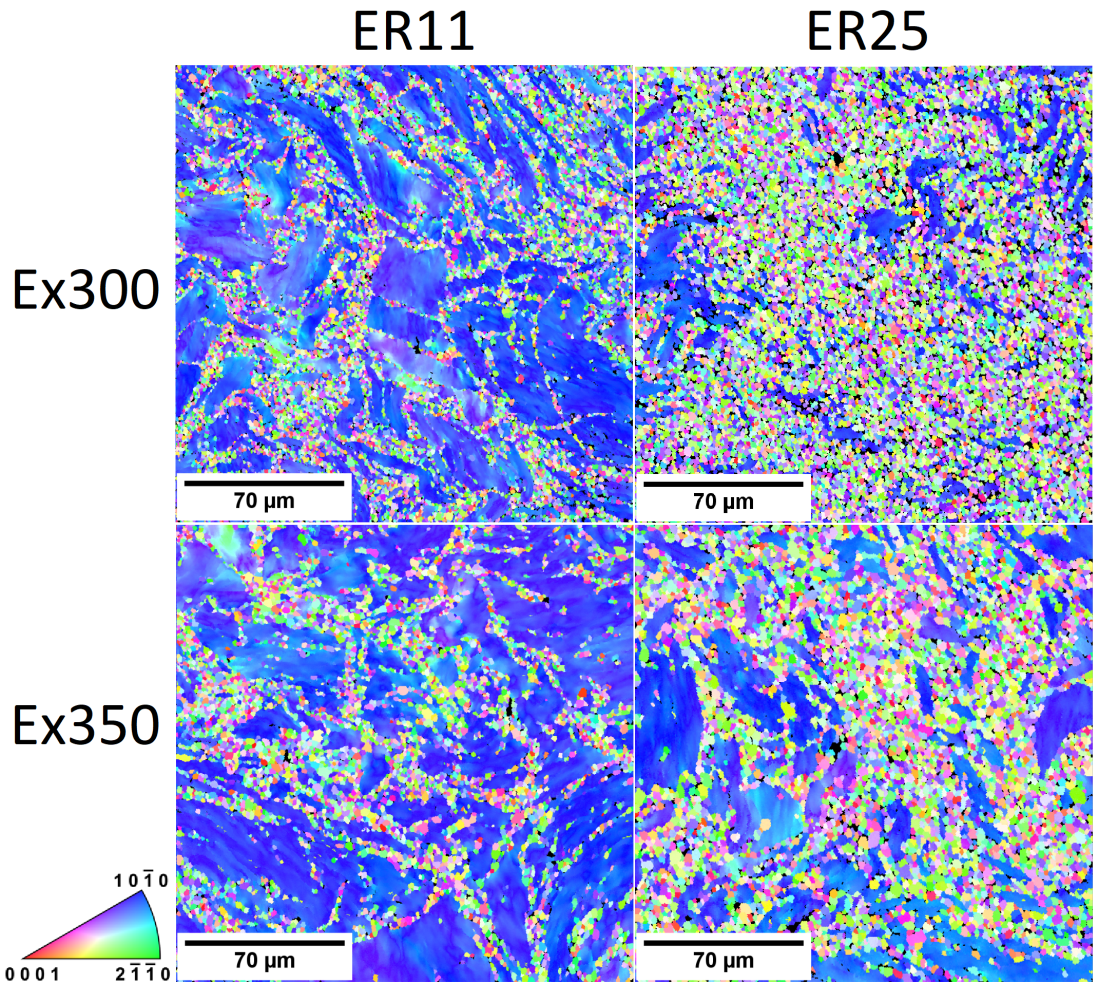

Figure 5.14: IPF orientation maps of extruded Mg-2Y-2Gd-1Ca measured in TS.

EBSD maps measured in LS are shown in Fig. 5.15. Non-recrystallized grains significantly elongated in the extrusion direction were observed in each condition. The largest fraction of elongated non-recrystallized grains is in the ER11 conditions, which corresponds to the measurement in TS. Although non-recrystallized grains were present in a small amount in Ex300-ER25 TS, their fraction is higher in the IPF map measured in LS. These grains may seem small in cross-section, but they may be hundreds of micrometers long in the direction parallel to the extrusion direction.

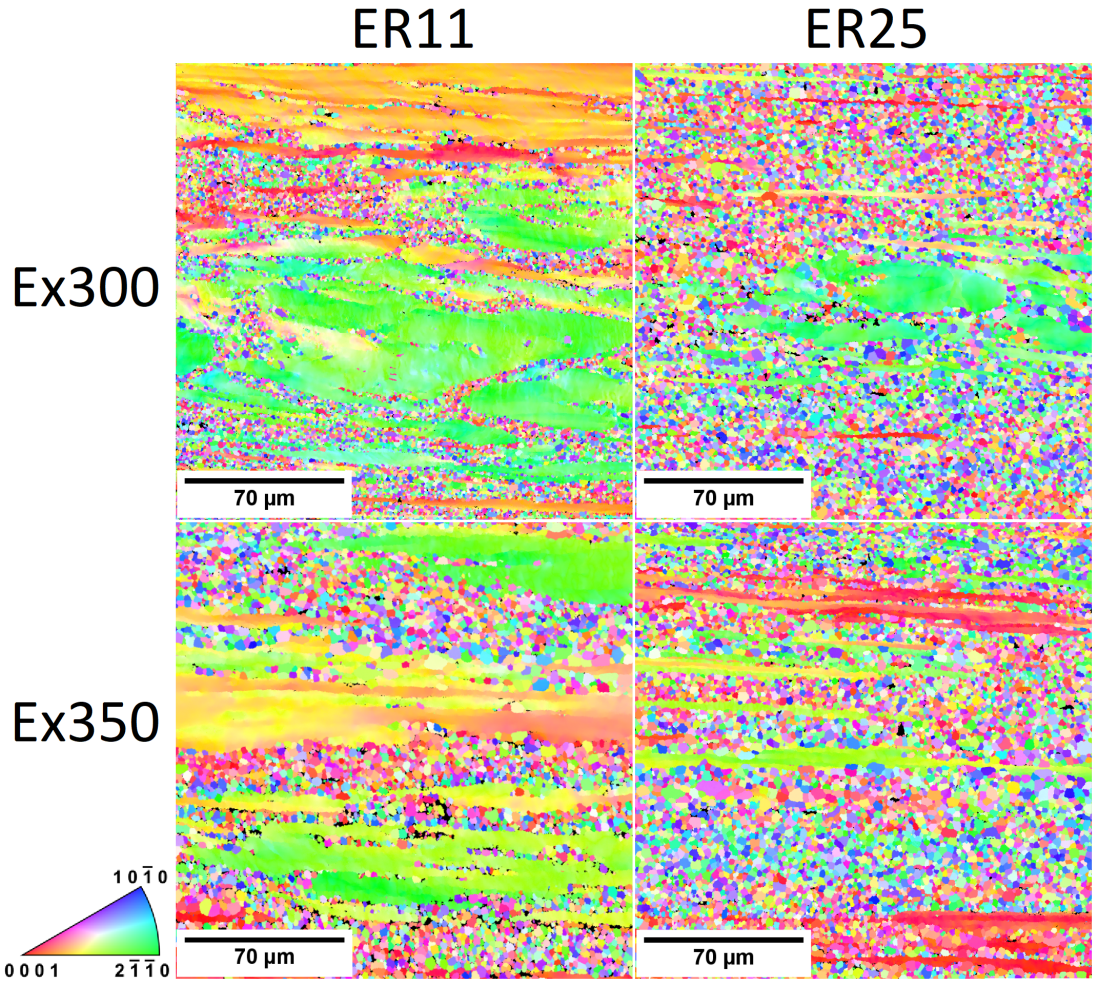

Figure 5.15: IPF orientation maps of extruded Mg-2Y-2Gd-1Ca measured in LS.

EBSD was also measured in ES, see Fig. 5.16. The microstructure of ER11 conditions is bimodal with a much higher fraction of recrystallized grains compared to microstructure measured in TS. The size of the recrystallized grains is slightly smaller in ES than in TS.

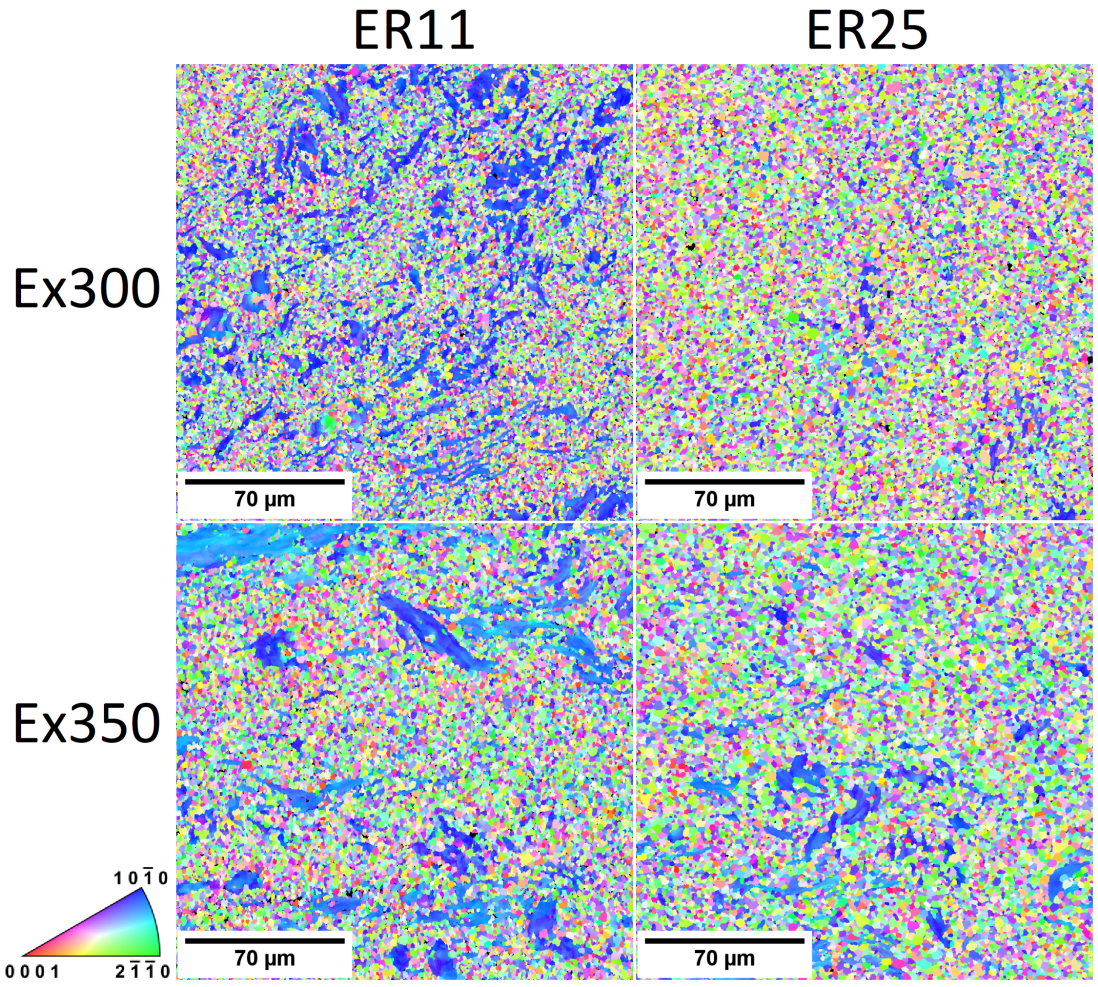

Figure 5.16: IPF orientation maps of extruded Mg-2Y-2Gd-1Ca measured in ES.

5.2.3 Texture

Recrystallized grains

Fig. 5.17 shows pole figures of recrystallized grains measured in TS. Recrystallized grains were selected based on grain size. The RE textural component was observed in all conditions. In the Ex300-ER11 condition, the $\{10\bar{1}0\}$ textural component passes continuously into the RE textural component. This phenomenon can also be observed in other conditions. With the increasing fraction of recrystallized grains decreases the intensity of the $\{10\bar{1}0\}$ and increases the intensity of the RE textural component.

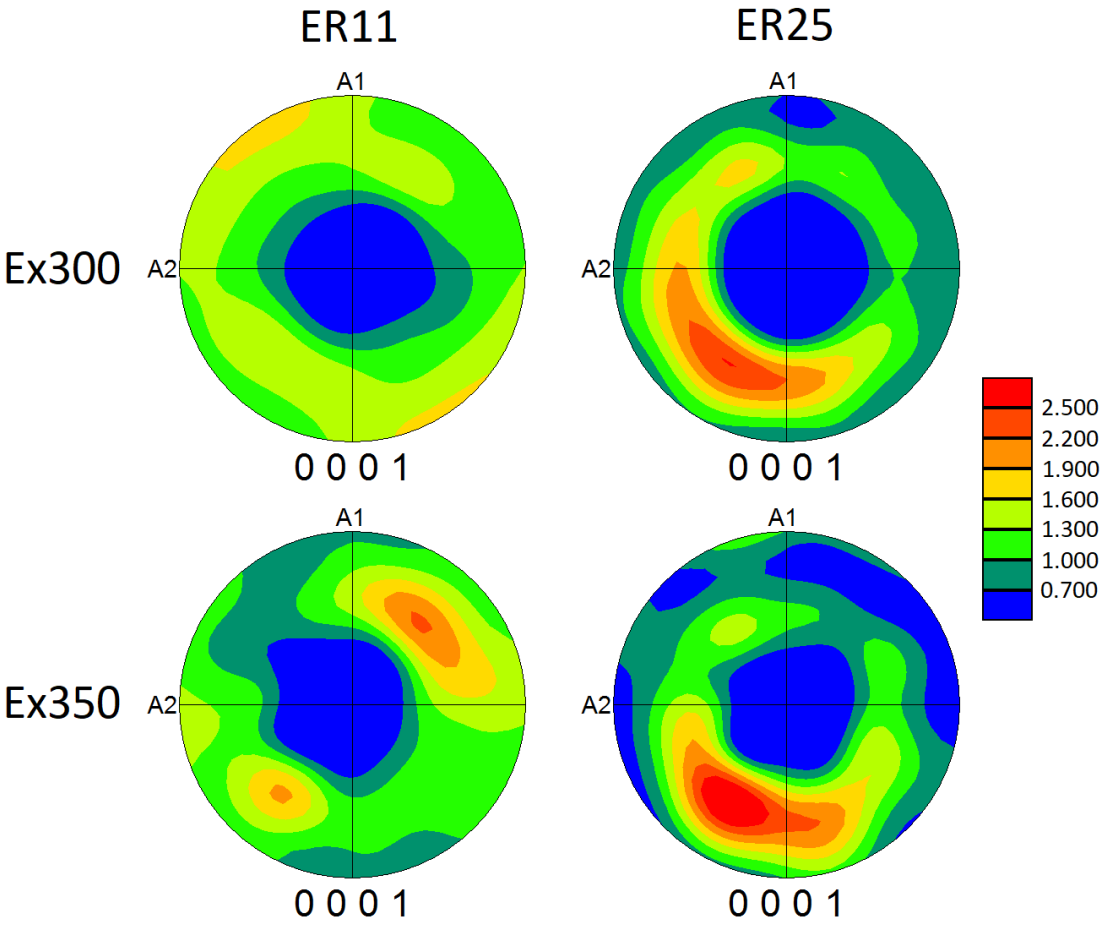

Figure 5.17: Pole figures of recrystallized grains calculated from the EBSD data measured in TS of extruded Mg-2Y-2Gd-1Ca.

Non-recrystallized grains

The $\{10\bar{1}0\}$ textural component typical for non-recrystallized grains of extruded magnesium alloys is dominant for all conditions, see Fig. 5.18. For the Ex300-ER25 condition, the pole figure is not shown due to the limited number of non-recrystallized grains.

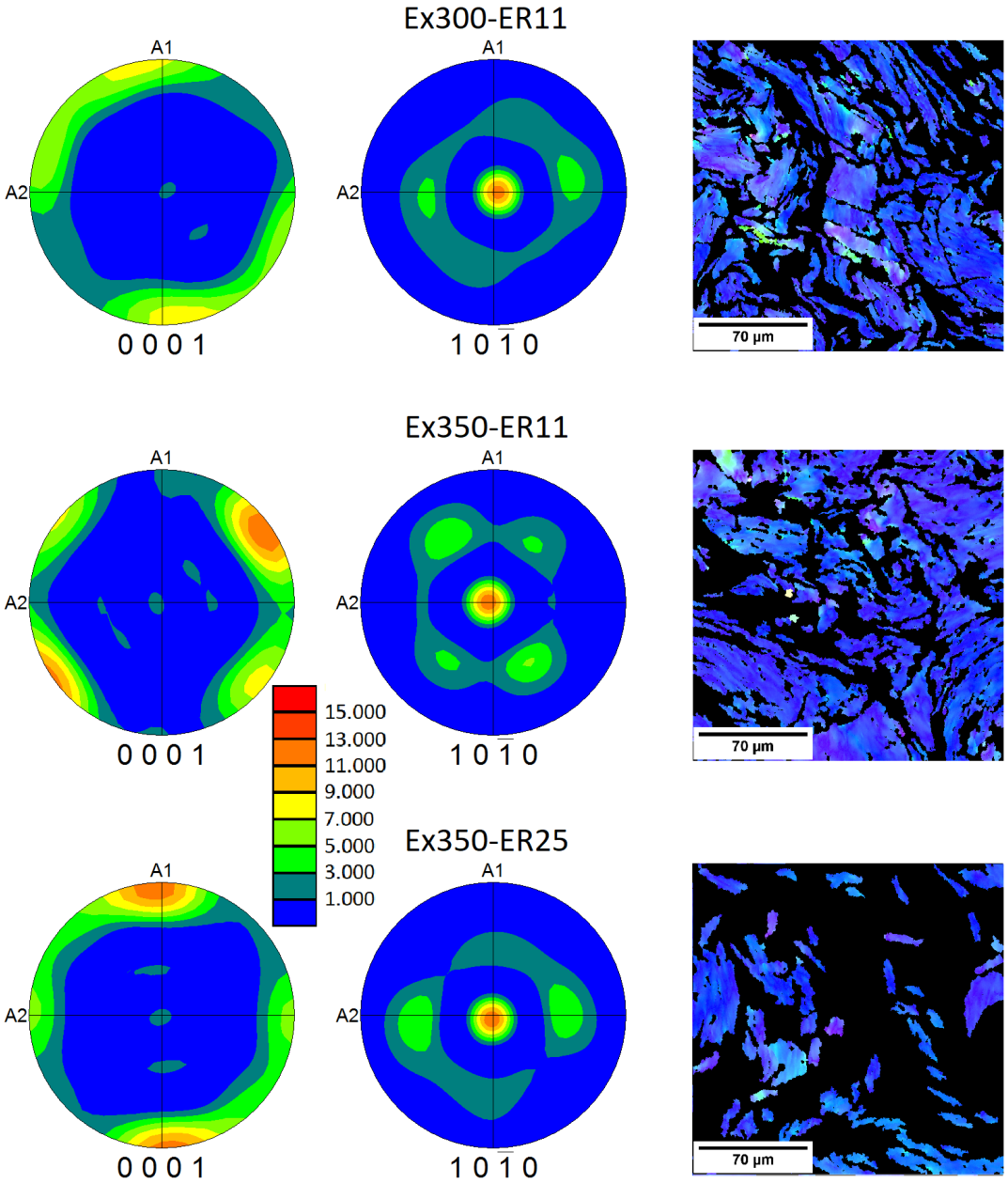

Figure 5.18: Pole figures and IPF maps of non-recrystallized grains calculated from the EBSD data measured in TS of extruded Mg-2Y-2Gd-1Ca.

5.2.4 Mechanical properties

Tensile and compressive tests

Compression stress-strain curves are shown in Fig. 5.19. Conditions extruded at lower temperatures (Ex300) have higher YCS. The highest value of YCS is achieved in the almost completely recrystallized Ex300-ER25 condition moreover, a sharp yield point can be observed. This is probably due to twinning, since a sharp yield point is not observed in the tensile test. In conditions with a strong $\{10\bar{1}0\}$ textural component (ER11 conditions), significant work hardening occurred. Non-recrystallized grains are favourably oriented for $\{10\bar{1}2\}$ twinning. Twinning with low CRSS is activated first, resulting in a decrease in YCS. When a large fraction of the grain volume is twinned, material significantly strengthens because neither twins are favourably orientated for basal slip, reoriented approximately about 86.3 ° relatively to their parent grains. As a result, Schmid factor is very low for basal slip.

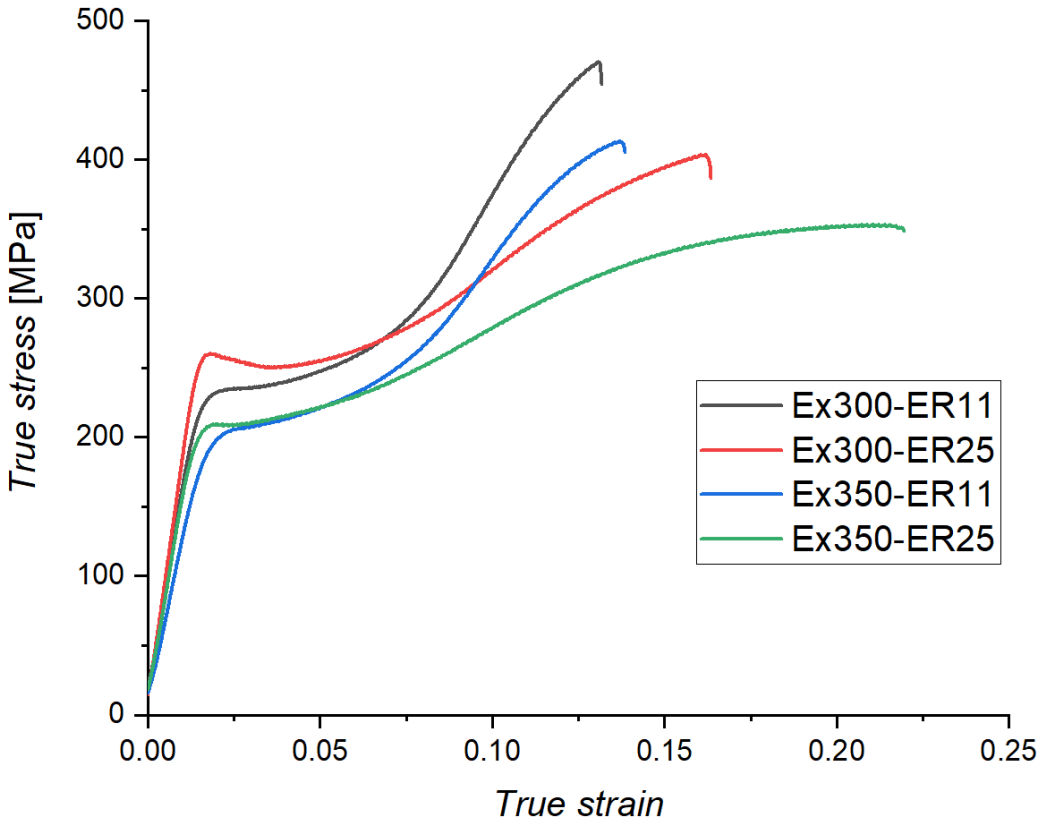

Figure 5.19: Compressive stress-strain diagrams of extruded Mg-2Y-2Gd-1Ca.

Tensile stress-strain curves are shown in Fig. 5.20. There is a significant difference between the studied conditions. Especially YTS of Ex300-ER25 is much higher than that of other conditions. Contrary to compression tests, $\{10\bar{1}0\}$ oriented grains neither take part in twinning, nor are suitably oriented for basal slip. Higher stress is required to activate other slip systems, resulting in higher YTS. Grain boundary strengthening can play an important role. The values of YTS (YCS) and UTS (UCS) are shown in Tab. 5.2.

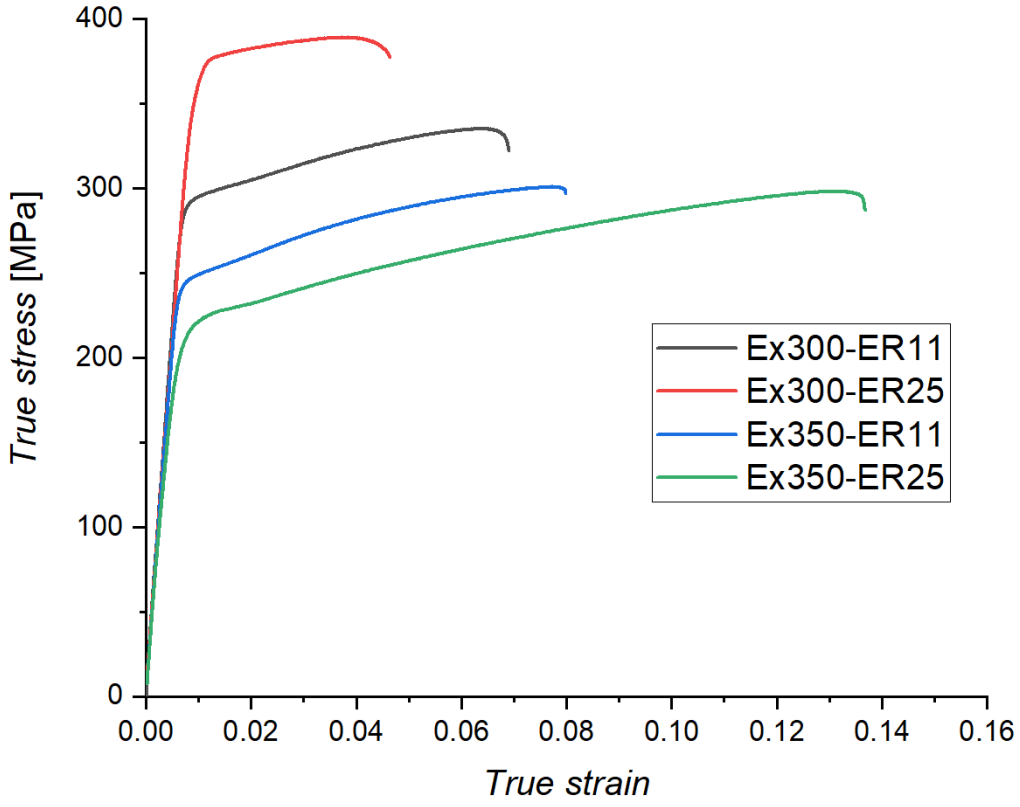

Figure 5.20: Tensile stress-strain diagrams of extruded Mg-2Y-2Gd-1Ca.

Microhardness measurements

The microhardness maps are shown in Fig. 5.21. In ER11 conditions, the microhardness on the edge is higher than in the middle of the sample. This corresponds to differences in microstructure at different locations in the sample. In the case of Ex300-ER25, the microhardness is almost homogeneous despite the different microstructure. Higher microhardness is not observed on the edge of the sample of the Ex350-ER25 condition. Mean microhardness values are stated in Tab. 5.2.

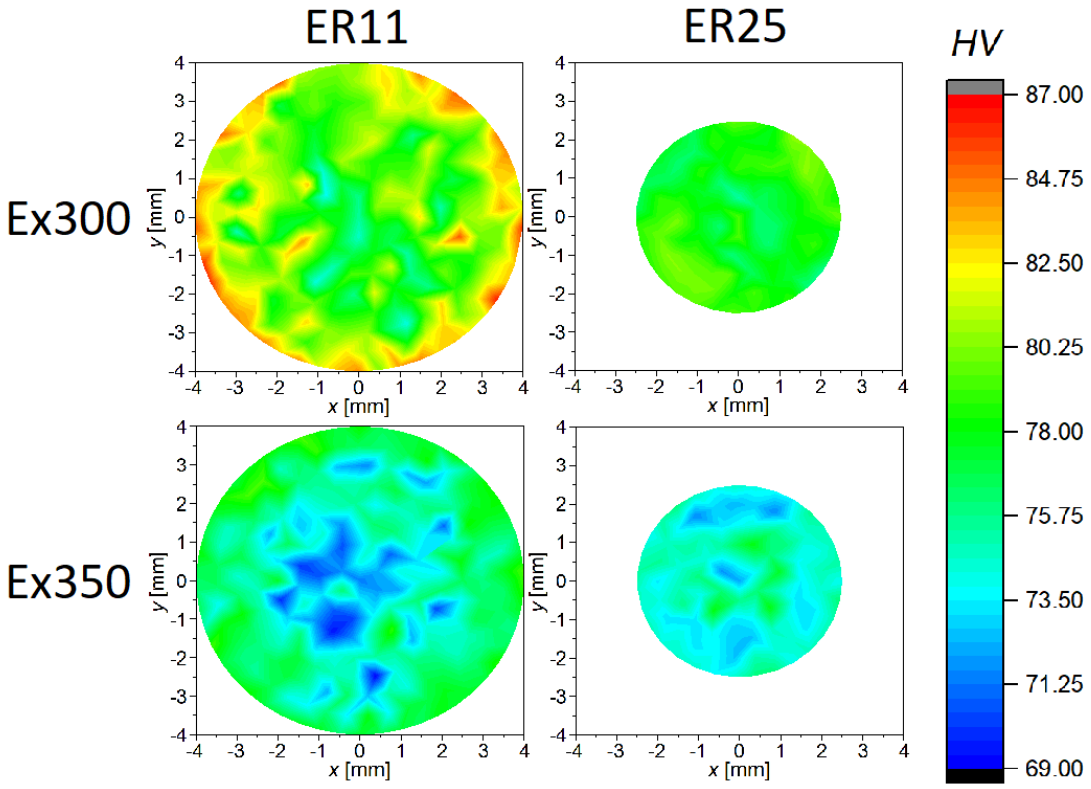

Figure 5.21: Microhardness maps of extruded Mg-2Y-2Gd-1Ca.

Material	*YCS* [MPa]	*UCS* [MPa]	*YTS* [MPa]	*UTS* [MPa]	*HV*
Ex300-ER11	231 ± 6	530 ± 12	292 ± 7	324 ± 8	80 ± 3
Ex300-ER25	259 ± 6	469 ± 11	362 ± 9	376 ± 10	79 ± 2
Ex350-ER11	199 ± 8	479 ± 11	248 ± 6	279 ± 7	75 ± 2
Ex350-ER25	207 ± 7	436 ± 9	219 ± 6	261 ± 6	75 ± 2
ECAP	315 ± 8	425 ± 12	303 ± 10	308 ± 10	92 ± 2

Table 5.2: Evaluated mechanical properties of Mg-2Y-2Gd-1Ca.

5.3 Mg-2Y-2Gd-1Ca after ECAP

5.3.1 Secondary phase particles

Processing by ECAP led to presence of tiny precipitates with homogenous distribution, see Fig. 5.22. REH_2 particles were observed by SEM (Fig. 5.22 (a)) but they are less abundant than tiny Mg_5RE and Mg_2Ca.
Fig. 5.23 shows TEM micrograph and EDS maps measured at the same area. Based on electron diffraction patterns, calcium-rich particles were identified as Mg_2Ca, RE-rich particles as Mg_5RE. They are only a few hundred nanometres in diameter, and Mg_2Ca are slightly larger than Mg_5RE. A higher concentration of RE elements in Mg_2Ca particles and Ca in Mg_5RE particles is evident from EDS maps.
Unlike the extruded conditions, no coherent precipitates and no small precipitates at the grain boundaries were observed. The lower temperature of the ECAP process (during sixth to eighth pass) compared to the extrusion process and especially the longer processing time led to the precipitation of Mg_5RE particles. Note that no Mg_5RE particles were observed in the extruded Mg-2Y-2Gd-1Ca alloy. Formation of the high density of Mg_5RE precipitates was already observed in WE43 alloy processed by ECAP [61].

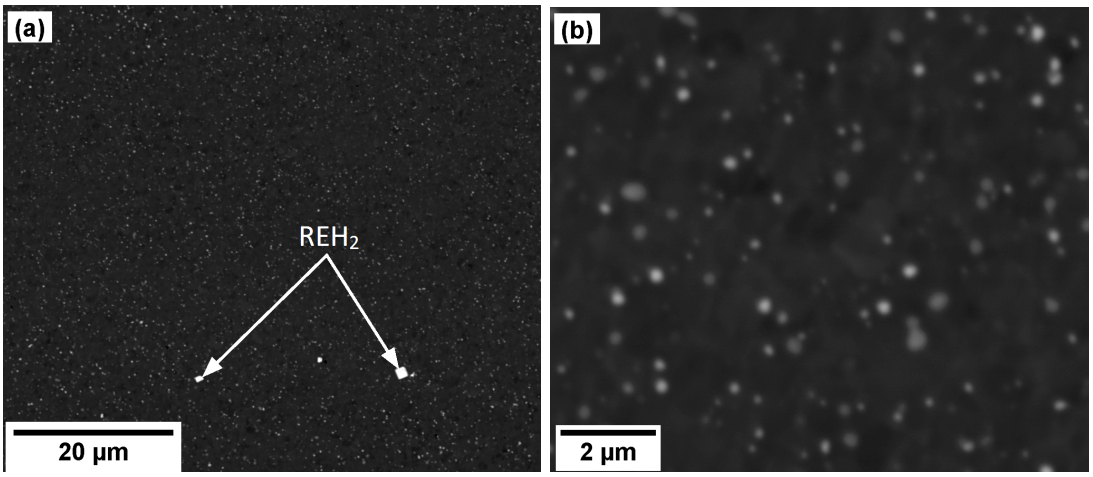

Figure 5.22: SEM micrographs of ECAP condition.

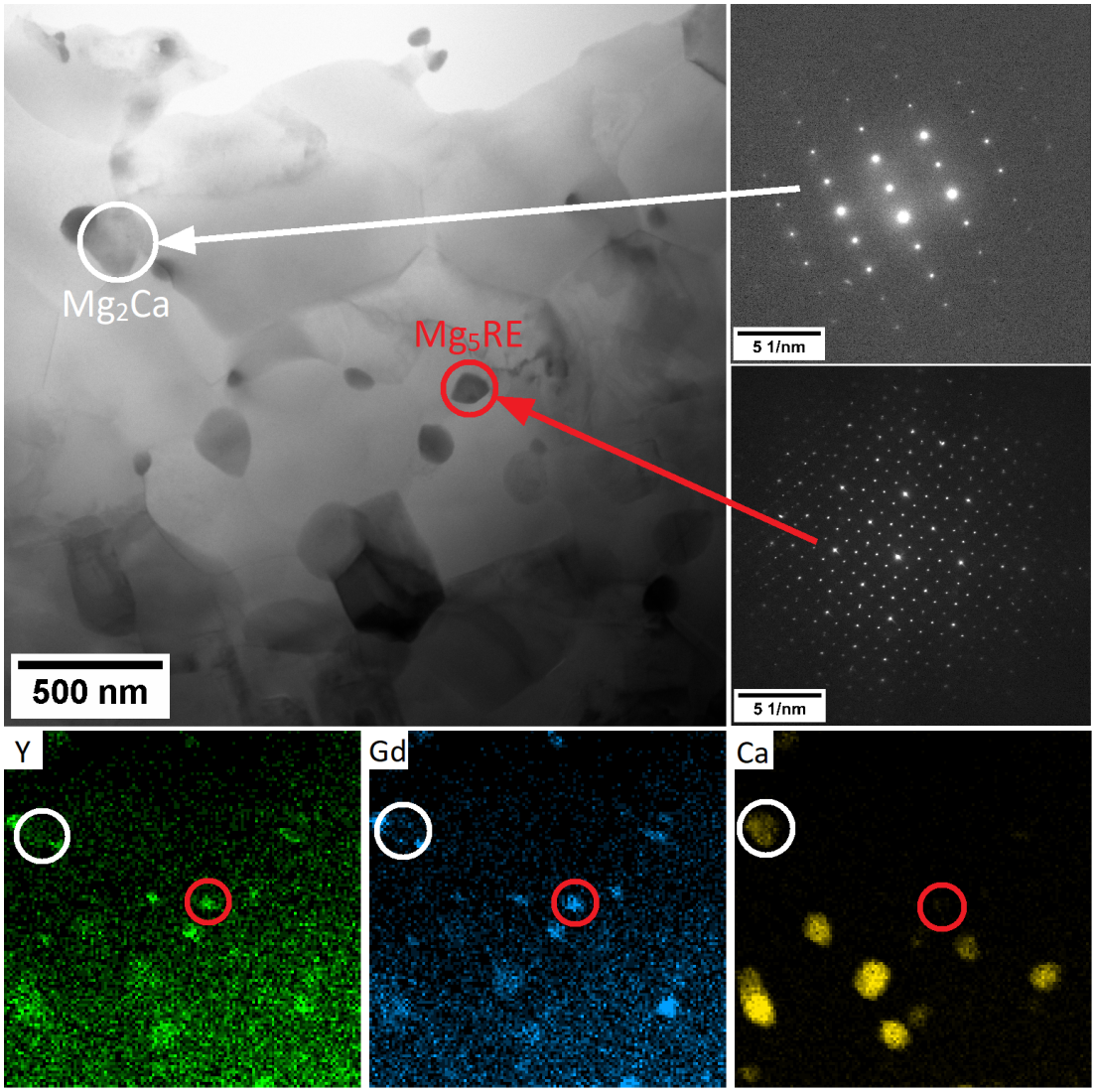

Figure 5.23: TEM micrograph of ECAP condition with diffraction patterns and EDS maps.

5.3.2 Grain microstructure

IPF maps measured in ZY and ZX planes (Fig. 5.25 (b)) are shown in Fig. 5.24. Although the microstructure measured in ZY plane appears homogeneous with equiaxed grains, it is evident from the IPF map measured in ZX plane that some grains are elongated close to ECAP direction. These elongated grains have mostly basal planes parallel to ECAP direction. The mean grain size calculated from IPF map measured in ZY plane is 0.9 µm.

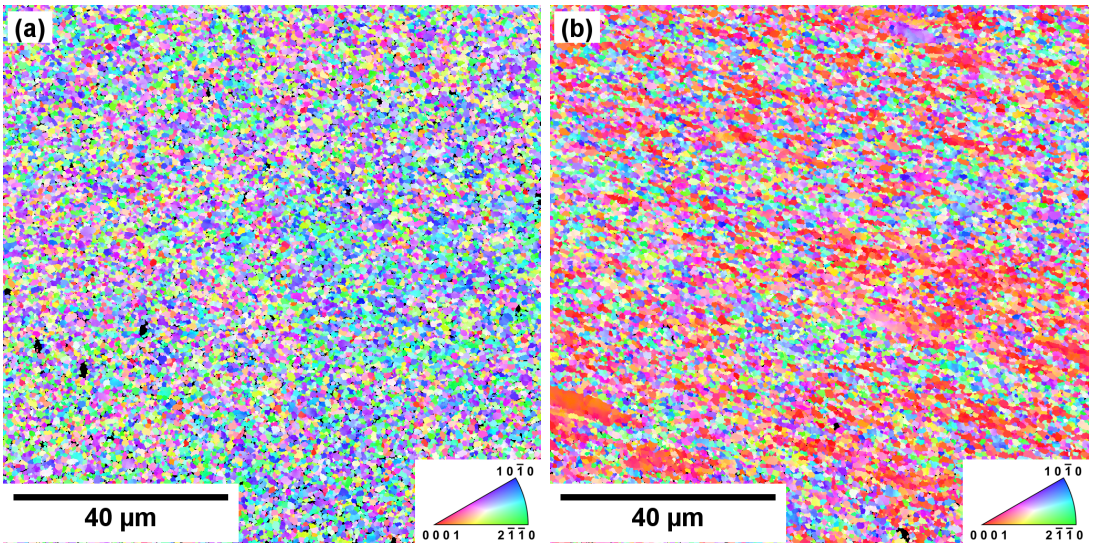

Figure 5.24: IPF orientation maps of ECAP condition measured in (a) ZY plane and (b) ZX plane.

5.3.3 Texture

Pole figure of ECAP condition calculated from the EBSD data measured in ZY plane is shown in Fig. 5.25. There are three textural components. The most intense one (denoted by A) has basal planes rotated by ∼55° from the processing direction. Its formation is attributed to activation of the basal slip system resulting in rotation of basal planes parallel to geometric slip plane in ECAP [81]. Small inclination in the Y direction is caused by rotation of the billet between passes (route B_C) [82]. Formation of this texture is typical in magnesium alloys processed by ECAP following route B_C [82–85].
Two other textural components (B and C) represent grains with a basal plane parallel to the ECAP direction. It was proved in Ref. [82] that the textural component denoted by B is associated with activation of the prismatic slip system, and the component C is associated with activation of the $\{11\bar{2}2\}\ \langle 11\bar{2}\bar{3}\rangle$ pyramidal slip system. Note that the fourfold symmetry is not associated with the square cross-section of the ECAP die as these textural components were observed in a magnesium alloy processed by ECAP with a circular cross-section [86].

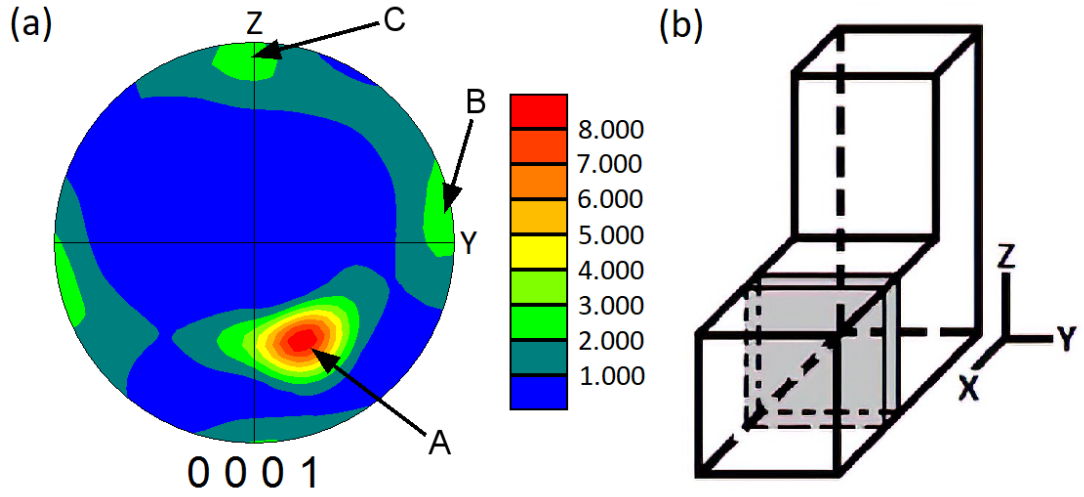

Figure 5.25: Pole figure of ECAP condition calculated from the EBSD data measured in TS (a) and the orientation of the sample for texture investigation (b) [61].

5.3.4 Mechanical properties

Tensile and compressive tests

Tensile and compressive stress-strain curves are shown in Fig. 5.26. Both curves reach a similar yield strength value, but only in the compression curve, yield elongation is present. This anisotropy was observed in another magnesium alloy processed by ECAP with a similar texture [67]. The cause may be the abrupt twinning after reaching sufficient stress. Due to twinning the length of the grains in the direction of compression is reduced which results in the shortening in the whole sample and the yield elongation (strain plateau). The formation of yield point elongation in fine-grained magnesium alloys is described in detail in Ref. [87].
It is clear that limited deformability was achieved in tension. This can be explained by the texture. At room temperature, CRSS of non-basal slip systems is high, and the basal slip system does not provide elongation in the c-axis, which is crucial to meeting the von Mises criterion. In the case of compression tests, non-basal slip systems are partially replaced by $\{10\bar{1}2\}$ twinning.

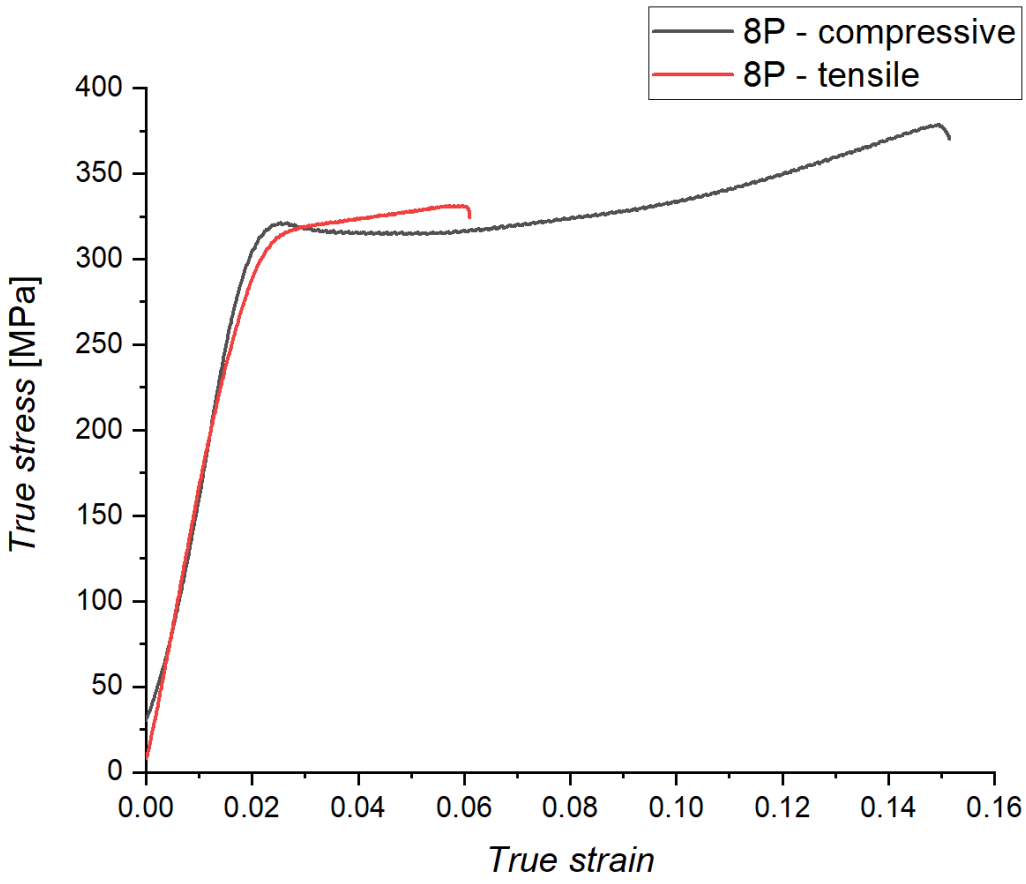

Figure 5.26: Compressive and tensile stress-strain diagram of ECAP condition.

Microhardness measurements

Microhardness map of ECAP condition is shown in Fig. 5.27. The sample orientation is the same as the orientation for texture investigation, see Fig. 5.25 (b). The microhardness is not homogeneous over the entire cross-section, it is significantly higher at the bottom edge. This may be due to the lower temperature at the bottom of the ECAP die, as the heating device is only on the sides. Lower processing temperature results in finer microstructure and improved mechanical properties. Higher strain caused by the friction on the bottom of the processed billet may also be the reason for the higher microhardness values [88]. The evaluated mechanical properties of ECAP condition are shown in Tab. 5.2

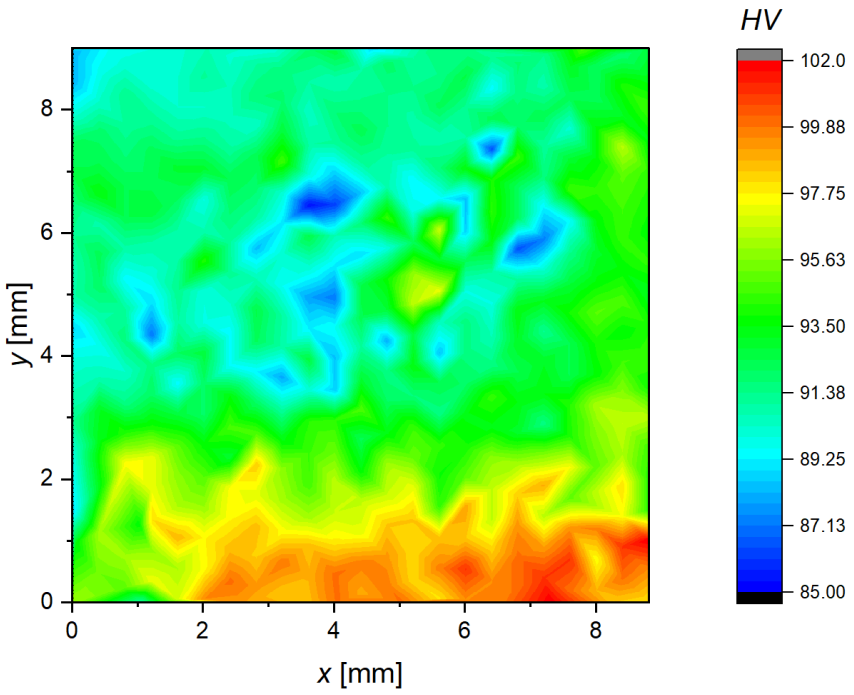

Figure 5.27: Microhardness map of ECAP condition.

6. Discussion

6.1 Secondary phase particles

Three types of secondary phase particles were observed in the alloys studied in this thesis - REH_2, Mg_2Ca, and Mg_5RE.

REH_2 precipitates

Particles of REH_2 were present in all conditions and only a small number of them was observed. They are easily recognized due to their square shape. Moreover, they can be easily recognized in SEM thanks to the Z-contrast because of the high atomic number. Hydrides are commonly present in the Mg-RE alloys already after casting because of a high affinity of RE to H. They can also form during mechanical polishing, which can cause more observed particles than there are actually in the material [89]. However, they were observed in ion-polished samples in TEM so their presence in the material is confirmed. In ECAP condition, the presence was particularly rare. Therefore, it cannot be assumed that they would affect the mechanical properties of the investigated alloys.

Mg_2Ca precipitates

Mg_2Ca particles were also observed in all conditions. In all extruded conditions, they occurred in the form of large particles (micrometres in diameter) and in the form of small incoherent and coherent precipitates (hundreds of nanometres in diameter). Large particles are usually aggregated and aligned along extrusion direction similarly to other alloys processed by extrusion [79,80,90]. These Mg_2Ca bands may contain a high density of crystal defects and even precracks [91]. Consequently, microcracks tend to generate within the Mg_2Ca particle regions, causing early failure of the alloys and decrease in their ductility [90].
Temperature of (Mg)+Mg_2Ca $\leftrightarrows$ (Mg) phase transition was determined by DSC measurement as $\sim$515 °C for both alloys. The temperature of solution annealing (480 °C), which preceded the extrusion, was not sufficient to dissolve large Mg_2Ca particles but, on the contrary, helped their growth. For the ECAP condition, DSC was measured first, and then the solution annealing temperature was determined to be 525 °C. Subsequent quenching in water resulted in the formation of a supersaturated solid solution. Small particles of Mg_2Ca observed in ECAP condition formed during the ECAP process.

Mg_5RE precipitates

Mg_5RE precipitates were observed in ECAP condition and extruded Mg-4Y-4Gd-2Ca alloy. The presence of Mg_5RE in the extruded Mg-2Y-2Gd-1Ca alloy was not confirmed, although very small amount of RE metal-rich particles were observed in Ex300-ER11 by TEM.
Equilibrium phase diagrams of Mg-3Y-xGd and Mg-2Y-xGd are shown in Fig. 6.1. Note that the actual composition of Mg-4Y-4Gd-2Ca alloy measured by EDS is 4.5 % Gd, 3.4 % Y and 2.6 % Ca, in wt. %. According to the phase diagram,

Mg_5RE particles form at temperatures lower than 430 °C in Mg-3Y-5Gd alloy, which has a similar composition to the investigated Mg-4Y-4Gd-2Ca alloy. The solvus temperature can be also affected by the presence of Ca however, the extrusion temperature 350/400 °C was significantly lower and therefore, Mg_5RE particles precipitated during the extrusion process.
In the case of Mg-2Y-2Gd, the solvus temperature is 340 °C. It is less than the extrusion temperature of Mg-2Y-2Gd-1Ca Ex350 conditions. This explains why no Mg_5RE particles were observed. The high density of these particles was observed in ECAP condition, which was exposed to lower process temperatures for much longer than extruded conditions.
The amount and size of precipitates depend on the temperature and time for which the material is exposed. The larger the difference between the temperature of the solvus and the processing temperature, the more favourable the given phase is in terms of Gibbs free energy. On the other hand, with increasing temperature, the diffusivity increases, which plays a crucial role in precipitation. Therefore, it is not easy to determine a suitable temperature for the heat treatment in terms of precipitation. The situation is also complicated because extrusion is a complex process in which there are also nonequilibrium processes that do not follow the equilibrium phase diagram.

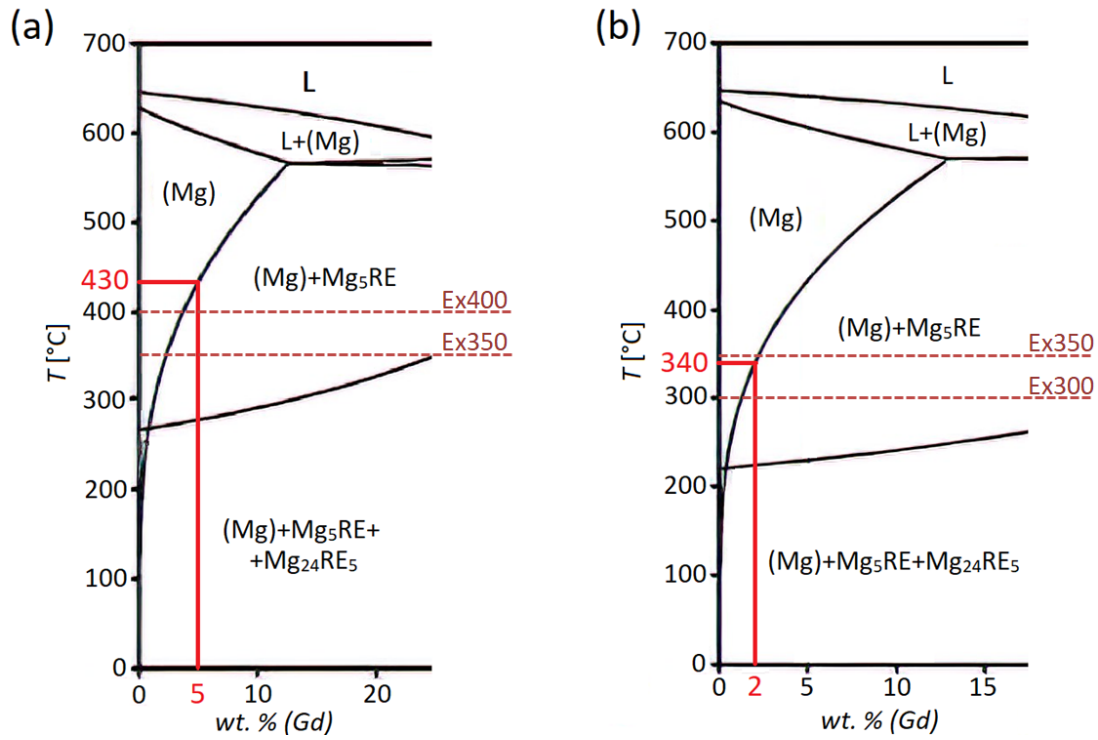

Figure 6.1: Equilibrium phase diagrams of (a) Mg-3Y-xGd and (b) Mg-2Y-xGd [92].

In the ECAP condition, particles play an important role both in precipitation hardening and during the ECAP process. Fine distribution of small precipitates inside the matrix can pin grain boundaries and hinder grain growth. Additionally, due to the presence of particles, dislocations are generated and gathered, which supports DRX. That results in the finer microstructure. RE-metal particles are

ideal for this purpose because of the high thermal stability [4]. Enhanced mechanical properties and ultrafine-grained microstructure was observed in magnesium alloys containing RE metals elements processed by ECAP [61, 83, 93].

6.2 Grain microstructure

Using EBSD measurement, the effect of temperature and extrusion ratio on the resulting microstructure was observed. The study was mainly focused on the degree of recrystallization, the size of the recrystallized grains and homogeneity within the extruded rods.

Degree of recrystallization

Fraction of recrystallized grains is influenced by extrusion temperature. In most conditions, the fraction of recrystallized grains increases with increasing extrusion temperature.
ER25 conditions show a higher fraction of recrystallized grains because the higher ER (ER25) results in the higher strain which promotes recrystallization. Especially for the Mg-2Y-2Gd-1Ca alloy, the effect of ER is significant. A higher fraction of recrystallized grains in alloys processed by extrusion with higher ER has already been observed [94, 95].
The only two fully recrystallized conditions studied in this work are Ex400-ER25 (Mg-4Y-4Gd-2Ca) and ECAP condition.

Grain size

The recrystallized grain size of different extruded conditions is shown in Fig. 6.2. The size of the recrystallized grains increases with increasing extrusion temperature. Significantly larger grains can be observed in conditions extruded at 400 °C. Increasing grain size with increasing processing temperature is expected in alloys processed by extrusion [95–98].
The effect of ER on mean grain size is not definite. For Mg-4Y-4Gd-2Ca, the grain size was reduced by increasing the extrusion ratio, while for Mg-2Y-2Gd-1Ca the opposite trend can be observed. Higher ER results in higher strain and consequent finer microstructure. On the other hand, higher ER may increase the processing temperature, resulting in an increase in grain size. Both trends were observed in magnesium alloys [94, 98].
The grain size does not appear to be affected by the concentration of the alloying elements, as the Ex350 conditions have a similar size of recrystallized grains. The mean grain size measured in ES is the same or slightly lower than in TS. The mean grain size of ECAP condition was only 0.9 μm. Alloys with an average grain size below 1 μm are called ultrafine-grained (UFG) alloys.

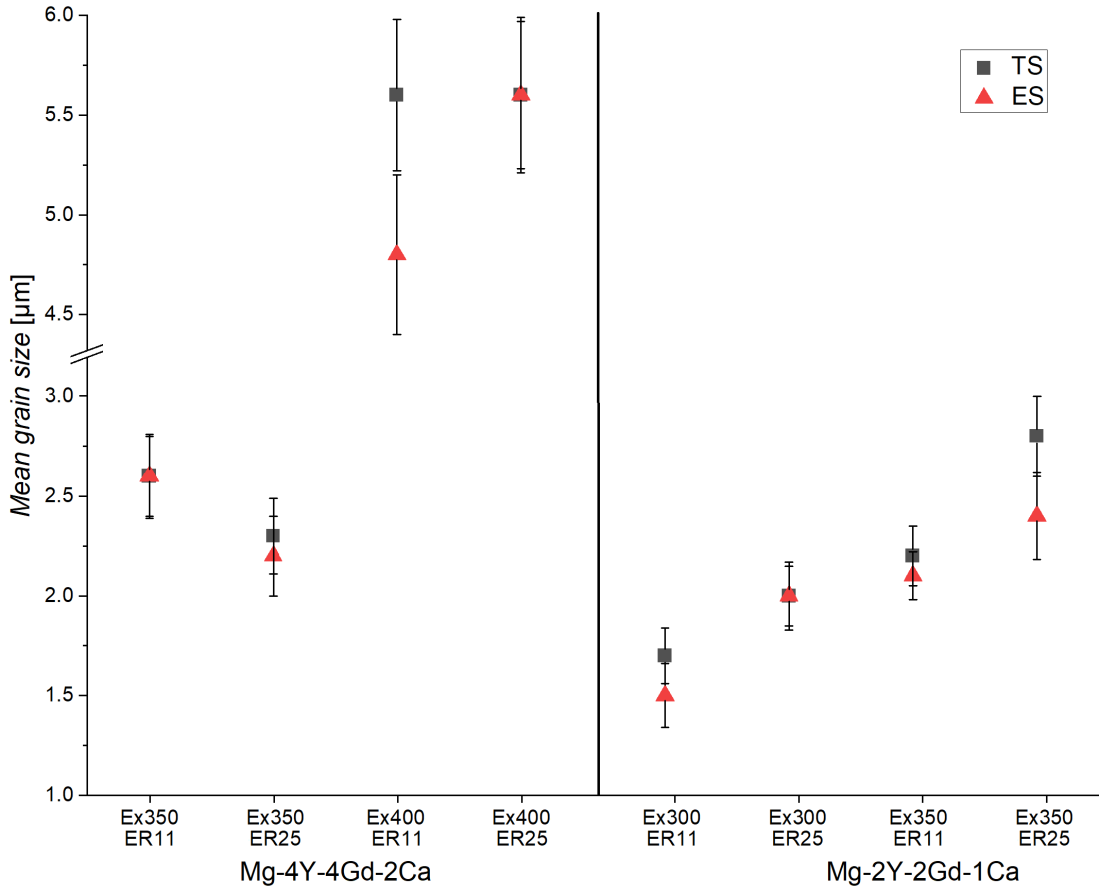

Figure 6.2: Mean recrystallized grain size of extruded conditions.

Homogeneity of the microstructure within the extruded rods

The microstructure is not homogeneous in most conditions. The fraction of recrystallized grains in ES is higher than in TS due to friction effects. From the measured data, it is not possible to say whether a different microstructure characterizes only a layer of a certain thickness or whether it is a gradient microstructure. In Ref. [78], 2 mm thick friction boundary layers were observed. Due to the diameter of the extruded rod (6 mm - ER25), a large part of the material can be affected by friction.

6.3 Texture

The texture was studied by EBSD for both recrystallized and non-recrystallized grains. The study of texture using EBSD has limitations, as data are collected on a limited number of grains.

Recrystallized grains

Recrystallized grains of all extruded conditions have RE textural component having a c-axis rotated by ∼45° from the extrusion direction. This textural component is weak for all conditions with a maximum intensity of 2.5 (Ex350-ER25

Mg-2Y-2Gd-1Ca). The RE textural component appears to form gradually during recrystallization. Conditions with a high fraction of non-recrystallized grains show a texture close to $\{10\bar{1}0\}$. With an increasing fraction of recrystallized grains, a fully developed RE textural component is formed. The orientation of the recrystallized grains is affected by the orientation of the parent grains. It has been reported that during discontinuous dynamic recrystallization (DDRX) the new DDRXed grains adopted orientations close to that of the adjacent parent grains. The mechanism of DDRX is characterized by nucleation and nucleus growth by high angle boundary migration [99, 100].
The origin of RE texture component is still under investigation. It has been proven that RE-textured grains tend to nucleate at shear bands in the RE-containing alloys. Non-RE alloys tend to recrystallize more from the interior of the deformed grains. [70]. A mechanism involving boundary pinning can also play an important role in restricting the preferential growth of grains with certain orientations.
The addition of RE leads to grain refinement, which is consistent with the consideration that the addition of RE hinders the growth of recrystallized grains. This results in a weakening of the texture. A weaker texture leads to an increase in ductility, but also to a decrease in yield and ultimate strength. The weakened RE texture has a suitable grain orientation for basal slip and promotes additional $\{10\bar{1}2\}$ twinning [70].

Non-recrystallized grains

All conditions containing non-recrystallized grains have strong $\{10\bar{1}0\}$ texture. They are not fibre components according to the pole figures, which is probably a consequence of local texture measurement by EBSD. The texture of the non-recrystallized grains may vary depending on the position in the extruded rod. Strong fibre $\{10\bar{1}0\}$ texture is typical for non-recrystallized grains of extruded magnesium alloys [73, 74].
Four different types of texture were described in extruded magnesium alloys, where the basal planes are parallel to the direction of extrusion. Beside fibre $\{10\bar{1}0\}$ texture, it is $\{11\bar{2}0\}$ fibre and $\{10\bar{1}0\}$-$\{11\bar{2}0\}$ double fibre texture as well as non-fibre texture without specific crystallographic directions parallel to the extrusion direction [71, 73, 74, 101–103]. All the mentioned textures can be part of the textural evolution during the extrusion process, and it is suggested that the final texture is related to extrusion parameters [71, 74, 101, 103].

ECAP condition

The ECAP condition has a texture typical for magnesium alloys processed by ECAP using route B_C. Strong component (intensity of 8.8) has basal planes rotated by $\sim 55°$ from the processing direction. Small inclination in the Y direction is caused by rotation of the billet between passes (route B_C). Other two textural components having basal planes parallel to processing direction were observed, see Fig. 5.25. The formation of these components is attributed to the alignment of the slip planes with the geometric slip plane during the ECAP process. Three different components correspond to three different slip systems - basal, prismatic and $\{11\bar{2}2\}$ $\langle 11\bar{2}\bar{3}\rangle$ pyramidal slip system [82].

6.4 Mechanical properties

6.4.1 Tensile and compressive tests

The evaluated tensile and compressive tests are shown in Fig. 6.3. For all extruded conditions of Mg-4Y-4Gd-2Ca alloy, YTS and YCS values are almost the same for the same condition. This is due to the RE textural component, which is suitable for activation of the basal slip system. Thus, deformation by twinning is limited. The only exception is semi-recrystallized condition Ex350-ER11 with stronger $\{10\bar{1}0\}$ textural component suitable for $\{10\bar{1}2\}$ twinning.
Conditions extruded at 350 °C are stronger in all parameters than conditions extruded at 400 °C. Material after extrusion at 400 °C is characterized by a larger mean size of recrystallized grains. Thus, grain boundary strengthening causes the higher strength. In addition, higher temperatures promote dynamic recovery, which leads to lower dislocation densities. Therefore, work hardening may also play an important role.
The conditions of the extruded alloy Mg-2Y-2Gd-1Ca are characterized by a strong $\{10\bar{1}0\}$ textural component which contributes to a significant anisotropy of mechanical properties. This corresponds to the YTS and YCS values of extruded Mg-2Y-2Gd-1Ca shown in Fig. 6.3. Most of the volume in conditions with a strong $\{10\bar{1}0\}$ textural component is not suitable for activation of the basal slip system, but is suitably oriented for $\{10\bar{1}2\}$ twinning in compression resulting in significantly higher YTS than YCS. The claim of twinning activation during compression tests also confirms the sigmoidal shape of stress-strain curves and yield elongation in some conditions [87]. As in the case of Mg-4Y-4Gd-2Ca alloy, the conditions extruded at a lower temperature are stronger. In addition, ER25 conditions have a higher YCS than ER11 conditions.

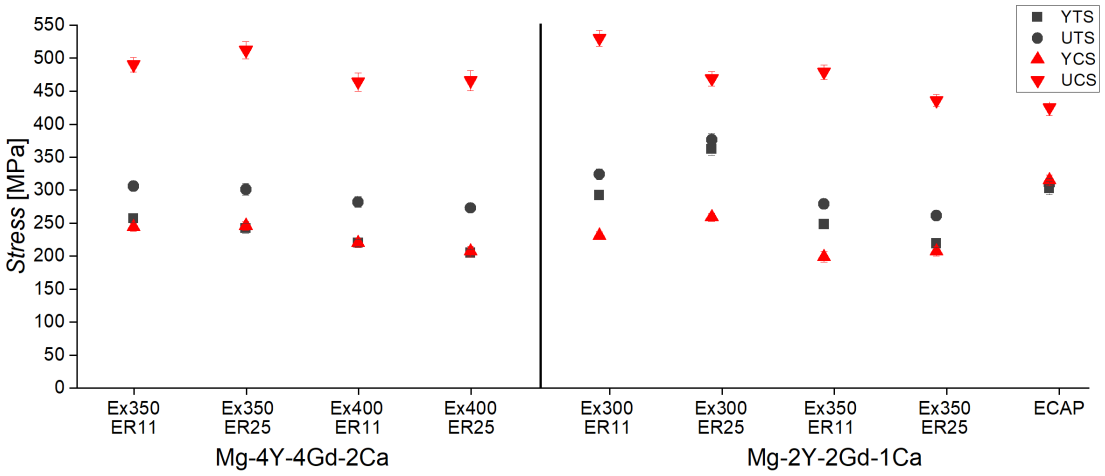

Figure 6.3: Evaluated tensile and compressive tests.

The ECAP condition is characterized by both high YTS and YCS (∼310 MPa). The low anisotropy of mechanical properties is caused by the texture, which consists of two weak components alowing $\{10\bar{1}2\}$ twinning in compression. On the other hand, ECAP condition almost does not strengthen, which has already been observed for RE-containing magnesium alloy processed by ECAP [61]. A combination of multiple strengthening mechanisms can cause the high values

of YTS and YCS. Grain boundary strengthening probably plays an essential role because of the small mean grain size (0.9 μm). Also, high density of small precipitates was observed, so precipitation hardening can contribute to increased strength. The dislocation density of conditions processed by several ECAP passes (>5) is usually comparable to the extruded condition [20, 104, 105]. Therefore, it cannot be assumed that work hardening would play a more significant role than in extruded conditions.

6.4.2 Microhardness measurements

Mean Vickers microhardness values are shown in Fig. 6.4. The microhardness values of the individual conditions are easier to compare than the values of tensile/compressive tests because they are not so much affected by the texture. During indentation, deformation occurs in multiple directions.
Vickers microhardness values are higher for conditions extruded at lower temperatures, and they match within the error for ER11 and ER25. There is a significant difference between the studied alloys. For instance, the difference in microhardness between the alloys extruded at 350 °C is bigger than HV 20. This is probably due to precipitation hardening, which is more significant for Mg-4Y-4Gd-2Ca due to the higher concentration of alloying elements. ECAP condition is characterized by a high microhardness (HV 92) compared to the extruded conditions of Mg-2Y-2Gd-1Ca. This is probably due to the smaller grain size and higher density of precipitates. Increased microhardness is typical for magnesium alloys processed by ECAP [20, 105–107].

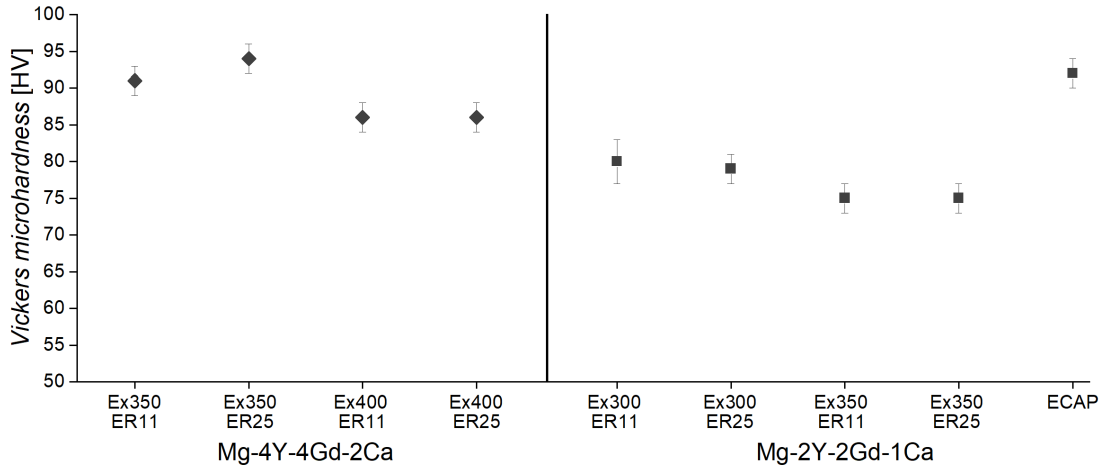

Figure 6.4: Vickers microhardness values.

The microhardness is not homogeneous over the whole cross-section. The edge of extruded rods is characterized by higher microhardness values in most conditions. This can be caused by friction effects. Friction at the interface extruded alloy-die causes a lower material flow rate than in the middle of the extruded rod. This is associated with strain accumulation. It results in higher dislocation density and finer microstructure [77, 78]. The same phenomenon can be observed in the ECAP condition, in which, however, the flow distribution is different than in extrusion [88]. Inhomogeneity of ECAP condition can be also caused by a lower

temperature at the bottom of the ECAP die, as the heaters are located only on the sides.

7. Conclusions

Non-flammable Mg-4Y-4Gd-2Ca and Mg-2Y-2Gd-1Ca alloys have been succsessfully prepared by extrusion using two extrusion temperatures and two extrusion ratios (ER). In addition, ultrafine-grained condition of Mg-2Y-2Gd-1Ca alloy was prepared by ECAP.

Characterization of the microstructure – secondary phases

- Mg_2Ca, Mg_5RE, and REH_2 secondary phases were observed in Mg-4Y-4Gd-2Ca alloy. Mg_5RE precipitates have not been observed in extruded Mg-2Y-2Gd-1Ca alloy.
- Extruded conditions are characterized by a large amount of Mg_2Ca particles in the form of large precipitates stretched in the extrusion direction as well as in the form of submicrometer coherent and incoherent precipitates.
- Analysis of phase diagrams explained precipitation of secondary phase particles in conditions processed at different temperatures.
- ECAP condition is characterized by a dense precipitation structure containing submicrometer Mg_2Ca and Mg_5RE.

Characterization of the microstructure – recrystallization and grain sizes

- The microstructure of extruded conditions was bimodal containing large elongated non-recrystallized and small equiaxed recrystallized grains. Only Ex400-ER25 condition of Mg-4Y-4Gd-2Ca was fully-recrystallized.
- Increasing extrusion ratio resulted in higher fraction of recrystallized grains.
- Higher extrusion temperature led to a larger size of recrystallized grains.
- Severe plastic deformation by eight passes of ECAP led to homogenous fully-recrystallized microstructure with the mean grain size of 0.9 μm.

Characterization of the texture

- The non-recrystallized grains are characterized by a strong $\{10\bar{1}0\}$ texture component common for all Mg alloys after extrusion.
- Recrystallized grains have a weak texture component having a c-axis rotated by ∼45° from the extrusion direction, which is typical for rare-earth containing Mg alloys (RE texture).
- Texture of ECAP condition consists of three component corresponding to the activation of three different slip systems: basal, prismatic and $\{11\bar{2}2\}$ $\langle 11\bar{2}\bar{3}\rangle$ pyramidal slip system.

Mechanical properties

- The texture significantly affected the mechanical properties. The conditions with the high fraction of non-recrystallized grains are characterized by anisotropy of mechanical properties due to the suitable texture for $\{10\bar{1}2\}$ twinning in compression.
- Higher concentration of alloying elements in Mg-4Y-4Gd-2Ca alloy, as well as higher extrusion temperatures, led to increase in microhardness values.
- Processing by ECAP led to enhanced mechanical properties with yield strength over 300 MPa in tension and compression. The weak anisotropy of mechanical properties is caused by weak textural components allowing twinning in compression. Also, high Vickers microhardness was achieved (HV 92).

The developed and analysed microstructural condition resulted in favourable mechanical properties. The studied alloys are therefore promising for the application in aerospace industry.

Bibliography

[1] M. Gupta and S.N.M. Ling. *Magnesium, magnesium alloys, and magnesium composites*. John Wiley & Sons, 2011.

[2] D.S. Aydin, Z. Bayindir, M. Hoseini, and M.O. Pekguleryuz. The high temperature oxidation and ignition behavior of Mg–Nd alloys part I: The oxidation of dilute alloys. *Journal of Alloys and Compounds*, 569:35–44, 2013.

[3] D.S. Aydin, Z. Bayindir, and M.O. Pekguleryuz. The high temperature oxidation behavior of Mg–Nd alloys. Part II: the effect of the two-phase microstructure on the on-set of oxidation and on oxide morphology. *Journal of Alloys and Compounds*, 584:558–565, 2014.

[4] L.W.F. Mackenzie, G.W. Lorimer, J.F. Humphreys, and T. Wilks. Recrystallization behaviour of two magnesium alloys. In *Materials Science Forum*, volume 467, pages 477–482. Trans Tech Publ, 2004.

[5] G. Cao, J. Kobliska, H. Konishi, and X. Li. Tensile properties and microstructure of SiC nanoparticle–reinforced Mg-4Zn alloy fabricated by ultrasonic cavitation–based solidification processing. *Metallurgical and Materials Transactions A*, 39(4):880–886, 2008.

[6] R.E. Brown. Magnesium and its alloys. *Materials and Mechanical Design*, page 278, 2006.

[7] G. Gottstein. *Physical foundations of materials science*. Springer Science & Business Media, 2013.

[8] S. Schuette, D. Vereault, B.T.G. Ting, and M. Janghorbani. Accurate measurement of stable isotopes of magnesium in biological materials with inductively coupled plasma mass spectrometry. *Analyst*, 113(12):1837–1842, 1988.

[9] B.L.. Mordike and T. Ebert. Magnesium: Properties — applications — potential. *Materials Science and Engineering: A*, 302(1):37 – 45, 2001.

[10] Hexagonal close packed crystal structure (hcp) — matse 81: Materials in today's world. `https://www.e-education.psu.edu/matse81/node/2134`. (Accessed on 12/13/2020).

[11] D. Drozdenko. Study of novel magnesium alloys with controlled microstructure and texture. Univerzita Karlova, Matematicko-fyzikální fakulta, 2016.

[12] K. Illková. Influence of solid solution elements and precipitate formation on the mechanical behaviour of magnesium alloys. Univerzita Karlova, Matematicko-fyzikální fakulta, 2013.

[13] Dislocations. `https://material.karlov.mff.cuni.cz/people/smilauerova/vyuka/FyzMat_I/FyzMat_I_3_dislocations.pdf`. (Accessed on 12/13/2020).

[14] R. Sánchez-Martín, M.T. Pérez-Prado, J. Segurado, J. Bohlen, I. Gutiérrez-Urrutia, J. Llorca, and J.M. Molina-Aldareguia. Measuring the critical resolved shear stresses in Mg alloys by instrumented nanoindentation. *Acta Materialia*, 71:283 – 292, 2014.

[15] R. von Mises. Mechanik der plastischen formänderung von kristallen. *ZAMM-Journal of Applied Mathematics and Mechanics/Zeitschrift für Angewandte Mathematik und Mechanik*, 8(3):161–185, 1928.

[16] M.H. Yoo. Slip, twinning, and fracture in hexagonal close-packed metals. *Metallurgical Transactions A*, 12(3):409–418, 1981.

[17] W.F. Hosford. *Mechanical behavior of materials*. Cambridge university press, 2010.

[18] Doitpoms - LDP library heating of a shape memory alloy spring - shape changes in a shear transformation. `https://www.doitpoms.ac.uk/ldplib/shape_memory/background.php?printable=1`. (Accessed on 02/09/2021).

[19] J. Čapek. Studium deformačních procesů v hexagonálních materiálech. Univerzita Karlova, Matematicko-fyzikální fakulta, 2013.

[20] J. Stráská. Physical properties of ultrafine-grained magnesium based alloys prepared by various severe plastic deformation techniques. Univerzita Karlova, Matematicko-fyzikální fakulta, 2014.

[21] W. Soboyejo. *Mechanical properties of engineered materials*, volume 152. CRC press, 2002.

[22] E.O. Hall. The deformation and ageing of mild steel: III discussion of results. *Proceedings of the Physical Society. Section B*, 64(9):747, 1951.

[23] N.J. Petch. The cleavage strength of polycrystals. *Journal of the Iron and Steel Institute*, 174:25–28, 1953.

[24] A.H. Cottrell. Theory of brittle fracture in steel and similar metals. *Trans. Met. Soc. AIME*, 212, 1958.

[25] M.A. Meyersm and E. Ashworth. A model for the effect of grain size on the yield stress of metals. *Philosophical Magazine A*, 46(5):737–759, 1982.

[26] J.C.M. Li and Y.T. Chou. The role of dislocations in the flow stress grain size relationships. *Metallurgical and Materials Transactions B*, 1(5):1145, 1970.

[27] O. Srba. Komplexní studium jemnozrnných polykrystalů Cu a slitiny CuZr připravených metodami equal channel angular pressing a high pressure torsion. Univerzita Karlova, Matematicko-fyzikální fakulta, 2012.

[28] W. Hume-Rothery. Atomic theory for students of metallurgy. 1952.

[29] R.L. Fleischer. Rapid solution hardening, dislocation mobility, and the flow stress of crystals. *Journal of Applied Physics*, 33(12):3504–3508, 1962.

[30] R. Labusch. Statistische theorien der mischkristallhärtung. *Acta Metallurgica*, 20(7):917–927, 1972.

[31] Precipitate hardening – isaac's science blog. `https://isaacscienceblog.com/2017/03/10/precipitate-hardening/`. (Accessed on 02/23/2021).

[32] P. Haasen. Mechanical properties of solid solutions. In *Fundamental Aspects of Structural Alloy Design*, pages 3–25. Springer, 1977.

[33] J.W. Martin. *Precipitation hardening: theory and applications*. Butterworth-Heinemann, 2012.

[34] S. Xu, D.L. McDowell, and I.J. Beyerlein. Sequential obstacle interactions with dislocations in a planar array. *Acta Materialia*, 174:160–172, 2019.

[35] F.J. Humphreys and P.B. Hirsch. The deformation of single crystals of copper and copper-zinc alloys containing alumina particles-II. Microstructure and dislocation-particle interactions. *Proceedings of the Royal Society of London. A. Mathematical and Physical Sciences*, 318(1532):73–92, 1970.

[36] H.R. Wenk and P. Van Houtte. Texture and anisotropy. *Reports on Progress in Physics*, 67(8):1367, 2004.

[37] U.F. Kocks, C.N. Tomé, and H.R. Wenk. *Texture and anisotropy: preferred orientations in polycrystals and their effect on materials properties*. Cambridge university press, 2000.

[38] P. Minárik. Effect of composition and microstructure on mechanical and corrosion properties in magnesium alloys with a potential for medical applications. Univerzita Karlova, Matematicko-fyzikální fakulta, 2014.

[39] Y. Kang, Z. Huang, H. Zhao, C. Gan, N. Zhou, K. Zheng, J. Zhang, F. Pan, J.C. Huang, and S. Wang. Comparative study of hot deformation behavior and microstructure evolution of as-cast and extruded WE43 magnesium alloy. *Metals*, 10(4), 2020.

[40] M. Bauser and K. Siegert. *Extrusion*. ASM international, 2006.

[41] M. Shahzad and L. Wagner. Influence of extrusion parameters on microstructure and texture developments, and their effects on mechanical properties of the magnesium alloy AZ80. *Materials Science and Engineering: A*, 506(1-2):141–147, 2009.

[42] X. Huang, Y. Chino, M. Yuasa, H. Ueda, M. Inoue, F. Kido, and T. Matsumoto. Microstructure and mechanical properties of AZX912 magnesium alloy extruded at different temperatures. *Materials Science and Engineering: A*, 679:162–171, 2017.

[43] T. Murai, S. Matsuoka, S. Miyamoto, and Y. Oki. Effects of extrusion conditions on microstructure and mechanical properties of AZ31B magnesium alloy extrusions. *Journal of Materials Processing Technology*, 141(2):207–212, 2003.

[44] V.M. Segal. *Russian Metall*, 1:99, 1981.

[45] R.Z. Valiev and T.G. Langdon. Principles of equal-channel angular pressing as a processing tool for grain refinement. *Progress in Materials Science*, 51(7):881–981, 2006.

[46] A.I. Alateyah, M.M.Z. Ahmed, Y. Zedan, H.A. El-Hafez, M.O. Alawad, and W.H. El-Garaihy. Experimental and numerical investigation of the ECAP processed copper: Microstructural evolution, crystallographic texture and hardness homogeneity. *Metals*, 11(4):607, 2021.

[47] M. Furukawa, Z. Horita, and T.G. Langdon. Factors influencing microstructural development in equal-channel angular pressing. *Metals and Materials International*, 9(2):141–149, 2003.

[48] Z. Horita, M. Furukawa, M. Nemoto, and T.G. Langdon. Development of fine grained structures using severe plastic deformation. *Materials Science and Technology*, 16(11-12):1239–1245, 2000.

[49] Y.C. Chen, Y.Y. Huang, C.P. Chang, and P.W. Kao. The effect of extrusion temperature on the development of deformation microstructures in 5052 aluminium alloy processed by equal channel angular extrusion. *Acta Materialia*, 51(7):2005–2015, 2003.

[50] A. Goloborodko, O. Sitdikov, R. Kaibyshev, H. Miura, and T. Sakai. Effect of pressing temperature on fine-grained structure formation in 7475 aluminum alloy during ECAP. *Materials Science and Engineering: A*, 381(1-2):121–128, 2004.

[51] Y.Y. Wang, P.L. Sun, P.W. Kao, and C.P. Chang. Effect of deformation temperature on the microstructure developed in commercial purity aluminum processed by equal channel angular extrusion. *Scripta Materialia*, 50(5):613–617, 2004.

[52] D. Dvorský, J. Kubásek, D. Vojtěch, and P. Minárik. Novel aircraft Mg-Y-Gd-Ca alloys with high ignition temperature and suppressed flammability. *Materials Letters*, 264:127313, 2020.

[53] A. Prasad, Z. Shi, and A. Atrens. Influence of Al and Y on the ignition and flammability of Mg alloys. *Corrosion Science*, 55:153–163, 2012.

[54] A. Prasad, Z. Shi, and A. Atrens. Flammability of Mg-X binary alloys. *Advanced Engineering Materials*, 14(9):772–784, 2012.

[55] S. Tekumalla, C. Yang, S. Seetharaman, W.L.E. Wong, C.S. Goh, R. Shabadi, and M. Gupta. Enhancing overall static/dynamic/damping/ignition response of magnesium through the addition of lower amounts ($< 2\%$) of yttrium. *Journal of Alloys and Compounds*, 689:350–358, 2016.

[56] J. Kubásek, D. Dvorský, M. Čavojský, M. Roudnická, and D. Vojtěch. WE43 magnesium alloy-material for challenging applications. *Kov. Mater*, 57:159–165, 2019.

[57] C. Liu, S. Lu, Y. Fu, and H. Zhang. Flammability and the oxidation kinetics of the magnesium alloys AZ31, WE43, and ZE10. *Corrosion Science*, 100:177–185, 2015.

[58] Scanning electron microscope - Wikipedia. `https://en.wikipedia.org/wiki/Scanning_electron_microscope#Detection_of_secondary_electrons`. (Accessed on 03/22/2021).

[59] Keywords - glossary of TEM terms — JEOL. `https://www.jeol.co.jp/en/words/emterms/search_result.html?keyword=kikuch%i20pattern&fbclid=IwAR1NG-qu765W16AIOnmHeO3cFfUVb8LhPaFXVMwTZWUqLUl1oXQd64j_7fo`. (Accessed on 03/23/2021).

[60] EBSD Oxford instruments - EBSD gallery. `http://www.ebsd.com/17-ebsd-applications/ebsd-gallery`. (Accessed on 03/24/2021).

[61] P. Minárik, J. Veselý, R. Král, J. Bohlen, J. Kubásek, M. Janeček, and J. Stráská. Exceptional mechanical properties of ultra-fine grain Mg-4Y-3RE alloy processed by ECAP. *Materials Science and Engineering: A*, 708:193–198, 2017.

[62] What is ultimate tensile strength? Science ABC. `https://www.scienceabc.com/pure-sciences/what-is-ultimate-tensile-strength.html`. (Accessed on 03/14/2021).

[63] Microhardness testing - an overview — ScienceDirect topics. `https://www.sciencedirect.com/topics/materials-science/microhardness-testing`. (Accessed on 03/17/2021).

[64] J.L. McNaughton, G. Höhne, W. Hemminger, and H.J. Flammersheim. *Differential scanning calorimetry*. Springer Science & Business Media, 2003.

[65] J. Šmilauerová. Phase transformations in modern titanium alloys. Univerzita Karlova, Matematicko-fyzikální fakulta, 2016.

[66] Principle of a heat-flux DSC - NETZSCH analyzing & testing. `https://www.netzsch-thermal-analysis.com/en/landing-pages/principle-of-a-heat-flux-dsc/`. (Accessed on 03/21/2021).

[67] J. Stráská, P. Minárik, S. Šašek, J. Veselý, J. Bohlen, R. Král, and J. Kubásek. Texture hardening observed in Mg–Zn–Nd alloy processed by equal-channel angular pressing (ECAP). *Metals*, 10(1):35, 2020.

[68] H. Vosskühler. The phase diagram of magnesium-rich Mg-Ca alloys. *Zeitschrift für Metallkunde*, 29:236–237, 1937.

[69] E.C. Burke. Solid solubility of calcium in magnesium. *JOM-Journal of the Minerals, Metals and Materials Society*, 7(2):285–286, 1955.

[70] N. Stanford and M.R. Barnett. The origin of "rare earth" texture development in extruded Mg-based alloys and its effect on tensile ductility. *Materials Science and Engineering: A*, 496(1-2):399–408, 2008.

[71] J. Bohlen, S. Yi, D. Letzig, and K.U. Kainer. Effect of rare earth elements on the microstructure and texture development in magnesium–manganese alloys during extrusion. *Materials Science and Engineering: A*, 527(26):7092–7098, 2010.

[72] S. Asqardoust, A.Z. Hanzaki, H.R. Abedi, T. Krajňák, and P. Minárik. Enhancing the strength and ductility in accumulative back extruded WE43 magnesium alloy through achieving bimodal grain size distribution and texture weakening. *Materials Science and Engineering: A*, 698:218–229, 2017.

[73] L.W.F. Mackenzie, B. Davis, F.J. Humphreys, and G.W. Lorimer. The deformation, recrystallisation and texture of three magnesium alloy extrusions. *Materials Science and Technology*, 23(10):1173–1180, 2007.

[74] M.G. Jiang, C. Xu, H. Yan, G.H. Fan, T. Nakata, C.S. Lao, R.S. Chen, S. Kamado, E.H. Han, and B.H. Lu. Unveiling the formation of basal texture variations based on twinning and dynamic recrystallization in AZ31 magnesium alloy during extrusion. *Acta Materialia*, 157:53–71, 2018.

[75] D. Li, V. Joshi, C. Lavender, M. Khaleel, and S. Ahzi. Yield asymmetry design of magnesium alloys by integrated computational materials engineering. *Computational Materials Science*, 79:448–455, 2013.

[76] M.R. Barnett. Twinning and the ductility of magnesium alloys: Part I:"Tension" twins. *Materials Science and Engineering: A*, 464(1-2):1–7, 2007.

[77] I. Flitta and T. Sheppard. Nature of friction in extrusion process and its effect on material flow. *Materials Science and Technology*, 19(7):837–846, 2003.

[78] V. Sanabria, S. Mueller, and W. Reimers. Microstructure evolution of friction boundary layer during extrusion of AA 6060. *Procedia Engineering*, 81:586–591, 2014.

[79] Z. Zeng, N. Stanford, C.H.J. Davies, J.F. Nie, and N. Birbilis. Magnesium extrusion alloys: a review of developments and prospects. *International Materials Reviews*, 64(1):27–62, 2019.

[80] H. Zengin and Y. Turen. Effect of Y addition on microstructure and corrosion behavior of extruded Mg–Zn–Nd–Zr alloy. *Journal of Magnesium and Alloys*, 8(3):640–653, 2020.

[81] H.K. Lin, J.C. Huang, and T.G. Langdon. Relationship between texture and low temperature superplasticity in an extruded AZ31 Mg alloy processed by ECAP. *Materials Science and Engineering: A*, 402(1-2):250–257, 2005.

[82] P. Minárik, R. Král, J. Čížek, and F. Chmelík. Effect of different c/a ratio on the microstructure and mechanical properties in magnesium alloys processed by ECAP. *Acta Materialia*, 107:83–95, 2016.

[83] S.M. Masoudpanah and R. Mahmudi. Effects of rare-earth elements and Ca additions on the microstructure and mechanical properties of AZ31 magnesium alloy processed by ECAP. *Materials Science and Engineering: A*, 526(1-2):22–30, 2009.

[84] T. Krajňák, P. Minárik, J. Stráská, J. Gubicza, K. Máthis, and M. Janeček. Influence of the initial state on the microstructure and mechanical properties of AX41 alloy processed by ECAP. *Journal of Materials Science*, 54(4):3469–3484, 2019.

[85] M. Janeček, S. Yi, R. Král, J. Vrátná, and K.U. Kainer. Texture and microstructure evolution in ultrafine-grained AZ31 processed by EX-ECAP. *Journal of Materials Science*, 45(17):4665–4671, 2010.

[86] T. Liu, Y.D. Wang, S.D. Wu, R.L. Peng, C.X. Huang, C.B. Jiang, and S.X. Li. Textures and mechanical behavior of Mg–3.3% Li alloy after ECAP. *Scripta Materialia*, 51(11):1057–1061, 2004.

[87] M.R. Barnett, M.D. Nave, and A. Ghaderi. Yield point elongation due to twinning in a magnesium alloy. *Acta Materialia*, 60(4):1433–1443, 2012.

[88] P. Chyła, S. Bednarek, A. Łukaszek-Sołek, and J. Sińczak. Strain distribution in ECAP process with various friction conditions-numerical modelling. *Metallurgy and Foundry Engineering*, 36(1):13, 2010.

[89] Y. Huang, L. Yang, S. You, W. Gan, K.U. Kainer, and N. Hort. Unexpected formation of hydrides in heavy rare earth containing magnesium alloys. *Journal of Magnesium and Alloys*, 4(3):173–180, 2016.

[90] H. Liu, C. Sun, C. Wang, Y. Li, J. Bai, F. Xue, A. Ma, and J. Jiang. Improving toughness of a Mg_2Ca-containing Mg-Al-Ca-Mn alloy via refinement and uniform dispersion of Mg_2Ca particles. *Journal of Materials Science & Technology*, 59:61–71, 2020.

[91] Z.T. Li, X.G. Qiao, C. Xu, S. Kamado, M.Y. Zheng, and A.A. Luo. Ultrahigh strength Mg-Al-Ca-Mn extrusion alloys with various aluminum contents. *Journal of Alloys and Compounds*, 792:130–141, 2019.

[92] Y. Guo, J. Li, J. Li, Z. Yang, J. Zhao, F. Xia, and M. Liang. Mg–Gd–Y system phase diagram calculation and experimental clarification. *Journal of Alloys and Compounds*, 450(1-2):446–451, 2008.

[93] Z. Kang, L. Zhou, and J. Zhang. Achieving high strain rate superplasticity in Mg–Y–Nd–Zr alloy processed by homogenization treatment and equal channel angular pressing. *Materials Science and Engineering: A*, 633:59–62, 2015.

[94] Y. Uematsu, K. Tokaji, M. Kamakura, K. Uchida, H. Shibata, and N. Bekku. Effect of extrusion conditions on grain refinement and fatigue behaviour in magnesium alloys. *Materials Science and Engineering: A*, 434(1-2):131–140, 2006.

[95] T. Murai, S. Matsuoka, S. Miyamoto, and Y. Oki. Effects of extrusion conditions on microstructure and mechanical properties of AZ31B magnesium alloy extrusions. *Journal of Materials Processing Technology*, 141(2):207–212, 2003.

[96] H. Zengin and Y. Turen. Effect of La content and extrusion temperature on microstructure, texture and mechanical properties of Mg-Zn-Zr magnesium alloy. *Materials Chemistry and Physics*, 214:421–430, 2018.

[97] H. Sun, C. Li, and W. Fang. Evolution of microstructure and mechanical properties of Mg–3.0Zn–0.2Ca–0.5Y alloy by extrusion at various temperatures. *Journal of Materials Processing Technology*, 229:633–640, 2016.

[98] M. Shahzad and L. Wagner. Influence of extrusion parameters on microstructure and texture developments, and their effects on mechanical properties of the magnesium alloy AZ80. *Materials Science and Engineering: A*, 506(1):141–147, 2009.

[99] H. Borkar, R. Gauvin, and M. Pekguleryuz. Effect of extrusion temperature on texture evolution and recrystallization in extruded Mg–1% Mn and Mg–1% Mn–1.6% Sr alloys. *Journal of Alloys and Compounds*, 555:219–224, 2013.

[100] J. Zhang, B. Chen, and C. Liu. An investigation of dynamic recrystallization behavior of ZK60-Er magnesium alloy. *Materials Science and Engineering: A*, 612:253–266, 2014.

[101] N. Stanford. The effect of calcium on the texture, microstructure and mechanical properties of extruded Mg–Mn–Ca alloys. *Materials Science and Engineering: A*, 528(1):314–322, 2010.

[102] S.S. Park, B.S. You, and D.J. Yoon. Effect of the extrusion conditions on the texture and mechanical properties of indirect-extruded Mg–3Al–1Zn alloy. *Journal of Materials Processing Technology*, 209(18-19):5940–5943, 2009.

[103] Q. Liu, X. Zhou, H. Zhou, X. Fan, and K. Liu. The effect of extrusion conditions on the properties and textures of AZ31B alloy. *Journal of Magnesium and Alloys*, 5(2):202–209, 2017.

[104] L. Balogh, R.B. Figueiredo, T. Ungár, and T.G. Langdon. The contributions of grain size, dislocation density and twinning to the strength of a magnesium alloy processed by ECAP. *Materials Science and Engineering: A*, 528(1):533–538, 2010.

[105] J. Vrátná. Physical properties of ultrafine-grained polycrystals of magnesium based alloys. Univerzita Karlova, Matematicko-fyzikální fakulta, 2010.

[106] R. Jahadi, M. Sedighi, and H. Jahed. ECAP effect on the microstructure and mechanical properties of AM30 magnesium alloy. *Materials Science and Engineering: A*, 593:178–184, 2014.

[107] K.R. Gopi, H.S. Nayaka, and S. Sahu. Investigation of microstructure and mechanical properties of ECAP-processed AM series magnesium alloy. *Journal of Materials Engineering and Performance*, 25(9):3737–3745, 2016.

List of Figures

List of Tables

List of Abbreviations

BSE	Backscattered electrons
CRSS	Critical resolved shear stress
DDRX	Discontinuous dynamic recrystallization
DRX	Dynamic recrystallization
DSC	Differential scanning calorimetry
EBSD	Electron backscatter diffraction
ECAP	Equal channel angular pressing
EDS	Energy-dispersive X-ray spectroscopy
ER	Extrusion ratio
ES	Transverse edge section
HCP	Hexagonal close-packed
IPF	Inverse pole figure
LS	Longitudinal section
ODF	Orientation distribution function
RE	Rare-earth
RT	Room temperature
SE	Secondary electrons
SEM	Scanning electron microscopy/microscope
SPD	Severe plastic deformation
TEM	Transmission electron microscopy/microscope
TS	Transverse middle section
UCS	Ultimate compressive strength
UFG	Ultrafine-grained
UTS	Ultimate tensile strength
YCS	Yield compressive strength
YTS	Yield tensile strength